NASA TECHNICAL REPORT

NASA TR R-153

NASA TR R-153

AN EXPERIMENTAL STUDY OF THE PRESSURE AND HEAT-TRANSFER DISTRIBUTION ON A 70° SWEEP SLAB DELTA WING IN HYPERSONIC FLOW

by Mitchel H. Bertram and Philip E. Everhart

Langley Research Center
Langley Station, Hampton, Va.

NATIONAL AERONAUTICS AND SPACE ADMINISTRATION • WASHINGTON, D. C. • DECEMBER 1963

AN EXPERIMENTAL STUDY OF THE PRESSURE AND HEAT-TRANSFER DISTRIBUTION ON A 70° SWEEP SLAB DELTA WING IN HYPERSONIC FLOW

By Mitchel H. Bertram and Philip E. Everhart

Langley Research Center
Langley Station, Hampton, Va.

NATIONAL AERONAUTICS AND SPACE ADMINISTRATION

For sale by the Office of Technical Services, Department of Commerce,
Washington, D.C. 20230 -- Price $2.75

CONTENTS

AN EXPERIMENTAL STUDY OF THE PRESSURE AND HEAT-TRANSFER DISTRIBUTION ON A 70° SWEEP SLAB DELTA WING IN HYPERSONIC FLOW

By Mitchel H. Bertram and Philip E. Everhart

SUMMARY

Results are presented for a study of the pressure and heat-transfer distributions and force characteristics of slab delta wings of 70° sweep at Mach numbers of 6.8 and 9.6 in air and 18 in helium. The wings had cylindrical leading edges and were tested with two different noses. One was sharp in plan view and the other was a tangent sphere with the same diameter as the cylindrical leading edge. Simple approaches to predicting the heat transfer are shown to be successful if the flow pattern peculiar to the angle-of-attack range under consideration is taken into account.

INTRODUCTION

At the present time, very little is known about the problem of heat transfer to highly swept wings and the aerodynamics of such a wing in the vicinity of the wing apex for the wide angle-of-attack range of interest in glider and reentry work. Much of the data available are for sharp-leading-edge delta wings and essentially flat-plate data applicable to high lift-drag gliders and in regions not close to the leading edge. A systematic research program was started at Langley Research Center to supply at least a portion of the needed information on blunt delta wings. As part of this program to supply this information, several slab delta wings have been studied in the Langley 11-inch hypersonic tunnel at Mach numbers of 6.8 and 9.6 in air and at 18.4 in helium to obtain aerodynamic-heating, pressure-distribution, static-stability, and flow-visualization data. A preliminary report on part of the results from this study was given in reference 1.

SYMBOLS

a	speed of sound
c	mean aerodynamic chord (3.5 inches)
c_r	root chord
c_p	specific heat of air at constant pressure
c_w	specific heat of model skin material
C_w	coefficient in linear equation for viscosity (see eq. (1))
C_D	drag coefficient referred to planform area, $\frac{\text{Drag}}{q_\infty S_p}$
C_L	lift coefficient referred to planform area, $\frac{\text{Lift}}{q_\infty S_p}$
C_m	pitching-moment coefficient about 2/3 root chord, $\frac{\text{Pitching moment}}{q_\infty S_p c}$
d	diameter
h	aerodynamic heat-transfer coefficient
j	index number
k	thermal conductivity
L	distance along leading edge measured from apex of slab portion of wing
L/D	lift-drag ratio
M	Mach number
N_{St}	Stanton number, $h/\rho u c_p$
N_{Pr}	Prandtl number
p	static pressure
q	heat-flow rate per unit area; dynamic pressure, $\rho_\infty u_\infty^2/2$
r	corner radius

R	radius
$R_{\infty,t}, R_{\infty,d}$	Reynolds number based on model thickness or nose diameter and free-stream conditions
s	distance along wing surface normal to leading edge from geometric stagnation point
s_c	surface distance along wing center line from geometric stagnation point
s_o	distance along wing surface normal to leading edge from midline of wing
S_o	distance along wing surface normal to leading edge from midline to center line of wing
S_p	planform area
t_w	model skin thickness
t	model thickness
T	temperature
T_e	adiabatic wall temperature
u	velocity
α	angle of attack
γ	ratio of specific heats of air
η_r	temperature recovery factor
θ	planform ray angle from stagnation point of sphere with origin at center of sphere nose
μ	dynamic viscosity
ρ	density
τ	time
Λ	sweep angle
Λ'	effective sweep angle

Subscripts:

2	static conditions just behind normal shock

l	local static conditions just outside boundary layer
max	maximum
N	normal to leading edge or windward surface
0	stagnation-point values
s	sphere
w	model skin
∞	undisturbed free-stream conditions

APPARATUS AND TESTS

Tunnel and Nozzles

This investigation was conducted in the Langley 11-inch hypersonic tunnel, a description of which may be found in reference 2. This blowdown facility has the capability of operation at different Mach numbers by changing nozzles. In the present tests, nozzles giving nominal Mach numbers of 6.8 and 9.6 with air and 18.4 with helium were used with a few tests at a Mach number of about 11 in helium. The Mach number 6.8 air nozzle is a contoured two-dimensional nozzle machined from Invar to minimize deflection of the nozzle throat due to thermal gradients. The Mach number 9.6 air nozzle is a contoured three-dimensional nozzle with square throat and test section. The Mach number 18 helium nozzle is contoured and has a circular cross section. A description and calibration of these nozzles may be found in references 3, 4, and 5.

Models

The wing chosen for this investigation consisted of a delta planform slab having a 70° sweep and a cylindrical leading edge. Wings were constructed having either a sharp prow or a blunt prow. The sharp prow was formed by the intersection of the elements of the cylindrical leading edge on the center line of the wing. For the blunt prow the apex was a tangent sphere with the same diameter as the cylindrical leading edge. The models are presented in figure 1.

Two heat-transfer and two pressure models, a sharp and blunt prow of each, were electroformed from nickel and had a skin thickness of approximately 0.030 inch and an overall thickness of 0.75 inch. The models were sting mounted in the test section on a movable support strut which could be rotated through an angle-of-attack range. Pressure and thermocouple locations for the models are shown in figure 1(a). The thermocouples on the heat-transfer models were No. 30 chromel-alumel wire (0.010-inch diameter) fastened to the model by welding a preformed bead into a hole drilled through the skin. The instrumentation is laid out normal to the leading edge and on the slab they are also arranged on rays

from the slab apex. Two main distance parameters are shown. One is labeled L/t and is the distance in diameters along the leading edge measured from the apex of the slab portion of the wing. (Note that the slab thickness is equal to the leading-edge and nose diameters.) The other distance parameter utilized is the distance along the wing surface normal to the leading edge also nondimensionalized in terms of wing thickness s_o/t. Continuous records of the tunnel stagnation temperature and the model skin temperatures were obtained on 18-channel recording galvanometers. Surface pressures were measured by means of the NASA aneroid-type six-cell recording units described in reference 2. An accuracy of approximately one-half of 1 percent of full-scale deflection can be obtained on the low-pressure instruments through careful calibration and reading of the records. For this investigation, pressure cells were chosen to give as near full-scale deflection as possible for the measuring station.

The force-test models consisted of four wings constructed of stainless steel having a thickness of 0.75 inch (7 thicknesses long) or 0.25 inch (21 thicknesses long) with a sharp- and a blunt-prow model of each thickness. (See fig. 1(b).) Shown in figure 1(b) is a photograph of the force models showing the half-cone adapter used to fasten the 21-diameter-long models to the sting. A sketch of the 21-diameter models and sting mount is presented in figure 1(c). These models had the same span and chord as the heat-transfer models. The force-test models were also used in the oil-flow and schlieren tests.

Range of Test Conditions

Heat-transfer and pressure measurements and surface flow data were obtained at Mach numbers of 6.8 and 9.6 in air and at a Mach number of 18 in helium. These models were tested for angles of attack from 0° to 45° in air and from 0° to 10° in helium.

Lift, drag, and pitching-moment data were obtained at Mach numbers of 6.8 and 9.6 in air with a sting-mounted strain-gage balance. A circular metal shield was used to protect the exposed portions of the balance behind the model. For the $M_\infty = 6.8$ tests the angles of attack of the models were measured optically by use of a light beam reflected from the model by a prism onto a calibrated scale. This method gives the true angles of attack of the model regardless of the deflection of the balance and sting under load. The angle-of-attack range for the $M_\infty = 6.8$ tests was from -2.5° to 45° and was obtained by using the same movable support strut as used in the heat-transfer test. The $M_\infty = 9.6$ data were obtained at angles of attack from -2.5° to 30°. At the higher angles of attack the tunnel boundary layer separated because of the strong shock from the models, struck the models, and invalidated the data. Because of the smaller size of the $M_\infty = 9.6$ nozzle windows, the prism method could not be used and the angles of attack of the models were obtained from the schlieren photographs.

The stagnation temperature was maintained at an average value of 650° F at $M_\infty = 6.8$ and $1{,}200^\circ$ F at $M_\infty = 9.6$ by means of a variable-frequency, resistance-tube heater to insure against liquefaction of the air. The $M_\infty = 6.8$ tests were made at stagnation pressures of approximately 10 and 30 atmospheres and gave Reynolds numbers based on model thickness (0.75 inch) of about 0.8×10^5 and

2.6×10^5. The stagnation pressures for the $M_\infty = 9.6$ tests were approximately 25 and 45 atmospheres and gave Reynolds numbers of about 0.4×10^5 and 0.8×10^5. The $M_\infty = 18$ tests were made at a stagnation pressure and temperature of 1,600-pound-per-square-inch gage and 60° F and yielded a Reynolds number of about 5.1×10^5. For the heat-transfer tests the wall temperature averaged about 570° R.

Visual Test Techniques

Schlieren photographs were taken of the flow pattern for each run. Top view schlieren photographs were obtained by using the force-test models. The schlieren system used in these tests had a single-pass vertical Z-shape light path with a horizontal knife edge. The light source for the schlieren photographs was a mercury-vapor arc lamp having a flash duration of about 3 microseconds.

Surface flow studies were made on the force-test models at Mach numbers of 6.8 and 9.6 in air and 18 in helium. Two oil-flow techniques were used. One method consisted of completely coating the model with a mixture of oil and lamp-black. The second method consisted of applying the mixture of oil and lampblack to the model in a dot pattern.

Data Reduction

Heat-transfer coefficients were obtained from the temperature-time curves by use of the following thin-skin heat-flow equation:

$$q = h\left(T_e - T_w\right) + q_c = \rho_c c_w t_w \frac{dT_w}{d\tau} + q_c$$

The finite time required for the proper flow conditions to be established in the nozzle by the quick start technique (1 to 2 seconds) was such that the temperature rise of the skin was sufficient to require conduction corrections. The required second derivative of surface temperature with surface distance (normal to the leading edge of the slab portion of the wing) was evaluated by a three-point finite-difference method. The resulting equation for conduction in the skin material at a point n is:

$$q_c = -\frac{t_w k_w}{4R^2}\left[\frac{\left(T_n - T_{n-2}\right)\sin^j\left(\frac{s}{R}\right)_{n-1} + \left(T_n - T_{n+2}\right)\sin^j\left(\frac{s}{R}\right)_{n+1}}{\left(\frac{\Delta s}{R}\right)^2 \sin^j\left(\frac{s}{R}\right)}\right]$$

in which the intervals are equally spaced and Δs is the surface distance from the end of one interval to the start of the next (n to $n + 1$, for example). The index exponent j is equal to 0 for the flat plate and cylinder and equal to 1 for the sphere. Also $R = d/2$ for the sphere or cylinder and $R = t/2$ for the flat plate and the skin thickness t_w and thermal conductivity k_w were assumed constant over the intervals. Since the preceding equation is

indeterminate at $s = 0$ for a sphere, in this case the following form is used:

$$q_{c,s=0} = -\frac{t_w k_w}{R^2\left(\frac{\Delta s}{R}\right)^2}\left(T_n - T_{n+2}\right)$$

Nickel properties were obtained from references 6 and 7 and are fitted by the following empirical equations:

$$k_w = 70.4 - 0.03333T_w, \frac{\text{Btu}}{\text{hr-ft-}^\circ\text{F}}$$

$$c_w = 0.000058T_w + 0.081, \frac{\text{Btu}}{\text{lb-}^\circ\text{F}}$$

where T_w is in degrees Rankine. The earliest time at which the tunnel stagnation temperature and pressure could be considered constant for each run was determined from the temperature traces. At this time, the model skin temperature T_w was read and $dT_w/d\tau$ determined from the slope of the temperature-time curve for each thermocouple. Adiabatic-wall temperatures T_e were calculated for each station from the relation:

$$\frac{T_e}{T_0} = \frac{1 + \eta_r \frac{\gamma - 1}{2} M_l^2}{1 + \frac{\gamma - 1}{2} M_l^2}$$

Local Mach numbers M_l were determined from the measured pressures by taking into account the entropy rise across the appropriate shock. For the sphere a normal shock was used and for the cylindrical leading edge and slab a swept-cylinder entropy rise was assumed. The recovery factor was calculated from the square root of the T-prime Prandtl number by Monaghan's laminar T-prime method as shown in reference 8. The variation of the adiabatic wall temperature with surface pressure and distance is shown in figure 2 for Mach numbers of 6.8 and 9.6. As indicated in figure 2(a), the adiabatic wall temperature ratios on a sphere for $M_\infty = 6.8$ and $M_\infty = 9.6$ were the same. In figure 2(b) the vertical line on the leading-edge plot indicates the junction of the cylinder and slab. The dashed lines to the right of this vertical line indicate the values of recovery-temperature ratio that would have been obtained had the cylinder continued beyond this junction.

RESULTS AND DISCUSSION

Details of Flow in Leading Edge and Nose Region

Cylindrical leading edge in air.- In order to assess the leading edge of the delta wing under study the results were compared with those from cylinder studies where attempts were made to obtain results valid for cylinders of infinite length. Much of these available data for the pressure distribution on a cylinder in air for various Mach numbers (refs. 9 to 11) are presented in figure 3. The data indicate that the pressure parameter p/p_{max} is a function only of position on the cylinder for Mach numbers normal to the cylinder greater than about 3.5 at least for $s/d < \pi/4$.

When the pressure distribution is fixed, then Lees theory (ref. 12) predicts that the distribution of heat-transfer coefficient will also be independent of the free-stream Mach number. Lees theory was evaluated by both the approximate solution which assumes the velocity distribution is linear at the slope evaluated at the stagnation point and the integral method in which the actual velocity and pressure distribution (fig. 3) are used. (See appendix for details on the application of Lees theory.) These results are compared in figure 4 with some results obtained in the Langley 11-inch hypersonic tunnel at $M_\infty = 9.6$ on an unswept cylinder which formed the nose of a blunt slab. There is not a great deal of difference between the two methods of evaluating Lees theory even though the velocity distribution is decidedly nonlinear above values of s/d of 0.3 or 0.4. Lees theory for the heat-transfer distribution was used with a stagnation-point value from Fay and Riddells theory (ref. 13) described in a following discussion. The agreement of theory with experiment is good, considering the uncertainties in the data.

Consider now the leading edge of the delta wings of this investigation. Figure 5 shows the variation of maximum Stanton number with angle of attack for the cylindrical leading edge of the delta wings at $M_\infty = 6.8$ and $M_\infty = 9.6$. These maximum Stanton numbers are actual leading-edge values chosen no matter where the maximum occurred and therefore are somewhat conservative. These maximums were generally obtained close to the geometric stagnation point. The parameter L/t is the station along the leading edge measured from the apex of the slab portion of the wing. (See fig. 1(a).)

The data are compared with predicted values obtained from the Fay and Riddell equation for heat transfer at the stagnation point of a blunt body which in a perfect gas may be written in terms of Stanton number

$$\left(N_{St,\infty}\sqrt{R_{\infty,d}}\right)_0 = \frac{0.54(2)^{j/2}}{N_{Pr}^{0.6}} C_w^{0.1} \sqrt{\frac{p_0}{p_\infty}\frac{\mu_0}{\mu_\infty}\left(\frac{T_\infty}{T_0}\right)^{1/2}\frac{1}{M_\infty}\left(\frac{d(u/a_0)}{d(s/d)}\right)_0} \qquad (1)$$

in which $j = 0$ for two-dimensional flow and $j = 1$ for axially symmetric flow and where

0 refers to conditions at stagnation point outside boundary layer

∞ refers to conditions in free stream

$$C_w = \frac{\mu_w T_0}{\mu_0 T_w}$$

Conditions with zero subscript were evaluated at the Mach number normal to the leading edge where for a swept wing

$$M_N = M_\infty \cos \Lambda' \tag{2}$$

in which the effective sweep angle Λ' is given by

$$\cos(90 - \Lambda') = \cos(90 - \Lambda)\cos \alpha \tag{3}$$

The Sibulkin equation for heat transfer to the blunt leading edge is (adapted from ref. 14)

$$\left(N_{St,\infty}\sqrt{R_{\infty,d}}\right)_0 = \frac{0.763(0.747)^{1-j}}{N_{Pr_2}^{0.6}} \sqrt{\frac{\mu_2}{\mu_\infty}\frac{a_0}{u_2}(\cos \Lambda')^{1-j}\left(\frac{d(u/a_0)}{d(s/d)}\right)_0} \tag{4}$$

where the 0.747 factor is obtained from reference 15 and

$$\frac{a_0}{u_2} = \sqrt{\frac{\left[(\gamma + 1)M_N\right]^2}{4 + 2(\gamma - 1)M_N^2}} \tag{5}$$

$$\frac{T_2}{T_\infty} = \frac{\left[2\gamma M_N^2 - (\gamma - 1)\right]\left[(\gamma - 1)M_N^2 + 2\right]}{\left[(\gamma + 1)M_N\right]^2} \tag{6}$$

The values of the geometric stagnation-point velocity gradient used in equations (1) and (4) varied as follows with Mach number normal to the swept cylinder (based on data contained in fig. 3).

M_N	$\left(\frac{d(u/a_0)}{d(s/t)}\right)_0$
1.5	1.88
2.0	2.03
3.0	2.15
4.0	2.18
9.6	2.18

In general, the Stanton numbers on the blunt-nose model at a Mach number of 6.8 (fig. 5(a)) are above the predicted values of Fay and Riddell. Similarly, at a Mach number of 9.6 (fig. 5(b)), both the Fay and Riddell and the Sibulkin equations underestimate the measured Stanton numbers on the blunt- and sharp-nose models. However, at $L/t = 5$, cylinder theory shows fair agreement with the measured Stanton numbers on the blunt-nose model at a Mach number of 9.6 up to an angle of attack of about 30°. For angles of attack up to 20° the blunt-nose data at $M_\infty = 6.8$ and $M_\infty = 9.6$ tend to follow the trend with angle of attack predicted by the infinite cylinder theory but drop below the theory at the higher angles of attack. The data at the $L/t = 0$ station, which may be considered as a line on a sphere, did not depart from the theoretical trend at the higher angles of attack. For the angle-of-attack range of the tests, the sharp-nose data followed the trend predicted by cylinder theory. However, an examination of the distribution of heat transfer about the leading edge of the sharp-nose wing at an angle of attack of 30° to 35° (to be presented later) indicates the data from the particular station are probably too high because of inadequate conduction corrections.

Schlieren studies have shown that at low angles of attack, the leading-edge shock when viewed from the top is parallel to the leading edge away from the nose-influenced region; however, at an angle of attack of 20° and higher, the shock is inclined at an angle to the leading edge as is shown in a later section. (See ref. 1.) With this change in the shock relationship to the leading edge is associated a change in the flow pattern on the wing. These schlieren photographs and flow studies are presented in detail in a later section.

Spherical nose in air.- Available data for the pressure distribution on a sphere at various Mach numbers in air (refs. 14 and 16 to 20) are shown in figure 6(a) together with the results obtained on the sphere nose of the delta wing of the present tests. One notes that, as for the cylinder results, the pressure distribution is practically invariant with Mach number for Mach numbers greater than 3.5 or 4. The delta-wing data which are averaged results over small intervals for all the data obtained show good agreement with the previously published sphere pressures.

These delta-wing data are given in more detail in figure 6(b) where it is designated according to angle of attack, Reynolds number, and station without averaging. The value of surface distances is obtained from the distance of an orifice from the geometric stagnation point along a geodesic. Both ray angle and angle of attack in the range shown apparently have no discernible effect.

The velocity distribution and the local Mach number of the averaged data obtained at $M_\infty = 9.6$ on the spherical nose of the delta wing are shown in figure 6(c). On this same figure for purposes of comparison are shown the data obtained on the unswept cylinder at $M_\infty = 9.6$ (see fig. 3) in the form of local velocity. The lines in figure 6(c) represent a fairing of all the hypersonic data in figures 3 and 6(a).

Figure 7(a) presents the Stanton number distribution on the spherical nose of the delta wing in air. The measured Stanton numbers on the spherical section are well predicted by Lees theory with the Fay and Riddell stagnation-point value.

However, the scatter of the data is admittedly greater than is desirable probably because the small diameter of the nose required the application of substantial conduction corrections. As for the pressures presented previously, both ray angle θ and angle of attack in the range shown had apparently no effect.

Again, as for the pressure, the data shown in figure 7(a) were averaged over small intervals and these results are shown in figure 7(b). The present data show reasonable agreement with the data obtained by Crawford and McCauley (ref. 14) on the hemisphere nose of a cylinder model.

Sphere and cylinder in helium.- Available data for the pressure distribution on a sphere in helium flow (refs. 21 and 22) are shown in figure 8(a) together with the results obtained on the sphere nose of the delta wing of the present tests. There is general agreement between the various sources of data. Some of the scatter in the shoulder region (s/d values around 0.78) can probably be attributed to the Reynolds number effects on surface pressure shown in reference 1.

The velocity distribution and the local Mach number for these helium data are presented in figure 8(b). For the velocity the lines shown on the figure are the faired values of all the pressure results from figure 8(a). For the Mach number the lines shown are the results obtained in air (fig. 6(c)). There are apparently only relatively small differences in the local Mach numbers obtained on these blunt shapes in air and helium.

Pressures and Heat Transfer Along Center Line of Wing

Pressures.- The center-line pressure distribution on the blunt-nose wing is shown in figure 9. The data are shown over a range of angle of attack from 0° to 46°. The pressure parameter is p/p_0 where p_0 is the stagnation pressure after a normal shock. The distance parameter s_c/t is the distance along the surface on the center line of the wing in terms of leading-edge diameters. The origin of the surface distance is always taken at the geometric stagnation point of the spherical nose. On the spherical nose there is a Mach number freeze, that is, p/p_0 is a function only of position on the sphere and not of free-stream Mach number as discussed earlier. On the slab portion of the high-pressure side of the wing, the pressure gradient induced by the blunt nose, which is so pronounced at an angle of attack of 0°, becomes less severe with increasing angle of attack and virtually disappears at an angle of attack of 20° and greater.

Heat transfer.- Figures 10(a) and 10(b) present the variation in heat-transfer-coefficient ratio along the center line of the blunt-nose model at $M_\infty = 6.8$ and $M_\infty = 9.6$. Heat-transfer coefficients measured at points along the center line, expressed as a fraction of the value calculated for the stagnation point of a sphere, are plotted against surface distance along the wing center line from the geometric stagnation point. The measured heat-transfer rates on the sphere nose were presented in figure 7. The results at a Mach number of 6.8 and 9.6 are similar. On the slab, at an angle of attack of 0°, oil flow showed that the nose effect extended back over the entire length of this short model

and, in addition, the cylindrical leading edge also has an effect which increases the pressures over that for the infinitely thin wing of the same planform shape. The heat-transfer coefficients in figures 10(a) and 10(b) are increased by the nose-induced pressures and thus are underestimated by strip theory. However, at $M_\infty = 6.8$, strip theory ($\alpha = 0^\circ$) modified for pressure, pressure gradient, and nose geometry (ref. 8) predicts the correct trend for the heat-transfer coefficients. As the angle of attack increases, the distance over which the induced pressures due to the nose are significant decreases as was shown in figure 9, and at an angle of attack of 21° the heat transfer on the windward surface of the slab is satisfactorily predicted by the constant-pressure strip theory from about 2 diameters back from the stagnation point.

At higher angles of attack, the flow becomes outward over the leading edge and at an angle of attack of 42°, cross-flow theory gives a good prediction of the center-line heat-transfer rates. An exception to this good agreement with the cross-flow theory is evident in the data at the higher angles of attack and values of s_c/t at Mach number 6.8. (See fig. 10(a).) This discrepancy between theory and experiment is believed to be a result of transition of the boundary layer to turbulent flow. This effect is also exhibited by unpublished results shown in figure 10(c) obtained in the Langley Unitary Plan wind tunnel on a spherical-nose wing tested at a higher Reynolds number and lower Mach numbers than in the present tests. The configuration was essentially the same as the one tested in the Langley 11-inch hypersonic tunnel except that this wing was 1 inch thick and 20 wing thicknesses long instead of 7.

The cross-flow theory is determined from an adaption of the Fay and Riddell relation for laminar stagnation-point heating. (See eq. (1).) In this case, the component of the free-stream flow normal to the windward surface of the wing is assumed to be the only one that contributes to the aerodynamic heating. With this assumption, the laminar cross-flow stagnation-point heating as a ratio to the laminar stagnation-point heating on a sphere is as follows for a slab wing with rounded edges where the edge radius of the wing is the same as the radius of the sphere:

$$\frac{h_{cf}}{h_{0,s}} = \left[\frac{1}{2}\frac{p_{0,N}}{p_0}\left(\frac{\mu_{0,N}}{\mu_0}\right)^{0.8}\left(\frac{T_0}{T_{0,N}}\right)^{0.3}\frac{\dot{u}}{S_o/t - 0.285}\right]^{1/2} \tag{7}$$

This result is independent of the wall temperature. Where S_o is the surface distance from the midline of the leading edge to the center line of the wing normal to the leading edge, the relation between surface distance normal to the leading edge and center-line surface distance from the geometric stagnation point of the sphere nose is given by the relation:

$$\frac{s_c}{t} = \frac{\frac{S_o}{t} - 0.785}{\cos \Lambda} + 0.785\left(1 - \frac{2\alpha}{\pi}\right) \tag{8}$$

The values from equation (1) used to normalize the data presented in figure 10 are as follows:

M_∞	$\left(N_{St,\infty}\sqrt{R_{\infty,d}}\right)_{0,s}$
3.51	3.72
4.65	4.73
6.8	6.84
9.6	8.95

If $p_{0,N}/p_0$ for hypersonic flow is given by the approximation

$$\frac{p_{0,N}}{p_0} \approx \sin^2\alpha \tag{9}$$

then equation (7) may be simplified somewhat to[1]

$$\frac{h_{cf}}{h_{0,s}} \approx \frac{\sin\alpha}{\sqrt{2}}\sqrt{\left(\frac{\mu_{0,N}}{\mu_0}\right)^{0.8}\left(\frac{T_0}{T_{0,N}}\right)^{0.3}\frac{\dot{u}}{S_0/t - 0.285}} \tag{10}$$

and

$$\frac{T_0}{T_{0,N}} = \frac{1 + \frac{\gamma - 1}{2}M_\infty^2}{1 + \frac{\gamma - 1}{2}(M_\infty \sin\alpha)^2} \tag{11}$$

$\dot{u}$ designates the nondimensional cross-flow stagnation-point velocity gradient at a point on the center line of the wing as a ratio to the velocity gradient at the stagnation point of a sphere

$$\dot{u} \equiv \left\{\frac{d\left(u/a_0\right)/d(s/t)}{\left[d\left(u/a_0\right)/d(s/d)\right]_s}\right\}_0 \tag{12}$$

---

[1]For very high Mach numbers and high angles of attack in flight, equation (10) reduces to

$$\frac{h_{cf}}{h_{0,s}} \approx (\sin\alpha)^{1.1}\sqrt{\frac{1}{2}\frac{\dot{u}}{S_0/t - 0.285}}$$

The value of $\dot{u}$ is expected to be a function of the ratio of the edge radius of the wing to the distance from the leading edge to the root chord of the wing measured normal to the leading edge. For disks this ratio is designated r/R and data indicate that this velocity gradient ratio varies with r/R as in the following sketch (for air) which utilizes the results already presented for a sphere plus disk data from references 19 and 23 to 28 and unpublished results from the Langley 9-inch supersonic tunnel at a Mach number of 3.6.

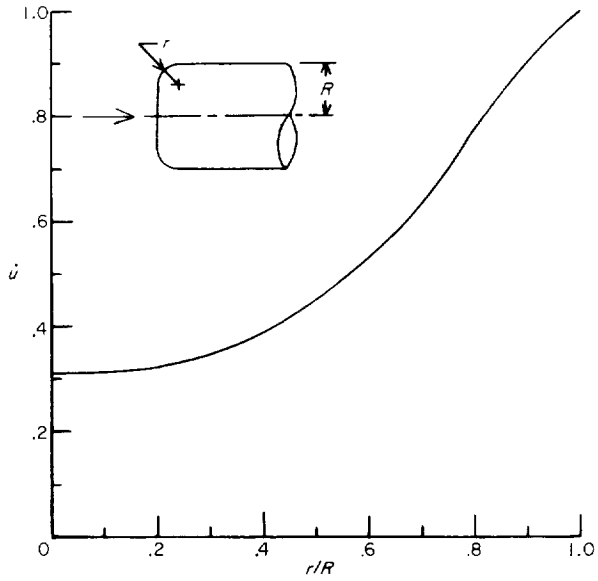

These values of $\dot{u}$ were assumed to hold for the delta wing with the relation between the disk dimensions and the wing dimensions, with $t = 2r$, taken to be

$$\frac{r}{R} = \frac{1}{2}\frac{1}{S_o/t - 0.285}$$

Visual Studies of Wings

Surface oil-flow patterns.- The role of nose shape, angle of attack, and Mach number in determining the flow patterns on the wing are shown in figures 11 to 14. A mixture of oil and carbon black was applied to the wing in various ways. One way was to coat the wing uniformly with the mixture before the run, another was to apply the oil mixture in stripes, and the third was to apply the oil mixture in discrete dots distributed over the wing.

At an angle of attack of 0° as shown in figure 11, the oil and lampblack patterns are similar for the Mach numbers shown which are 6.8 and 9.6 in air and approximately 11 and 18 in helium. Along the blunt leading edge, the flow picture is as expected from a swept cylinder. A region of central outflow is

evident for both the sharp- and blunt-prow models; however, the region influenced by the nose is smaller in the case of the sharp-prow models. This central outflow is a consequence of the mass of air at high induced pressures which enters the wing over the apex region and is contained by the shock, the wing surface, and the high pressure induced in the air coming from the leading-edge region. In this sort of phenomenon, dissipation of this prow effect must occur as this air moves further downstream and the proportion of the wing surface affected must diminish. This dissipation can be seen by comparing the 7-diameter wing with the 21-diameter wing. The model with thickness-to-chord ratio (t/c_r) of 0.143 is 7 thicknesses long; whereas the model with $t/c_r = 0.048$ is 21 thicknesses long.

Surface flow studies at Mach number of 6.8 and 9.6 in air and at angles of attack from 10° to 45° are presented in figures 12 and 13. The surface shears indicate an inflow toward the center of the wing at angles of attack of 10° to 20°. At an angle of attack of 30° the flow appears to be straight. With increasing angle of attack, cross-flow effects start to predominate and the flow at the surface turns out from the center as shown by the cases for angles of attack of 40° to 45°. The surface flow patterns at angle of attack are similar for Mach numbers of 6.8 and 9.6. Surface flow studies at a Mach number of 18.4 are presented in figure 14(a) for an angle of attack of 10° and are similar to the Mach number 6.8 and 9.6 patterns.

Surface flow studies for the leeward side of the models (figs. 12(c), 13(c), 13(d), and 14(b)) indicate that, at low angles of attack, there is strong prow influence similar to that shown at an angle of attack of 0° (fig. 11) and at the higher angles of attack of the tests separated flow existed on the leeward side. These effects are evident even when the half-cone that is used as a model support on the thin model covers much of the lee side. Several photographs of the leeward side indicate erratic flow patterns which are a result of oil accumulation splattering during tunnel shutdown.

Side and top view schlieren photographs.- Figures 15 to 21 present the side view and top view schlieren photographs of the sharp- and blunt-nose models. The flow field for the 7-diameter model is representative of the forward one-third of the 21-diameter model magnified 3 times. In figures 15 and 16, the model is at an angle of attack of 0° at $M_\infty = 6.8$ and $M_\infty = 9.6$ in air and at $M_\infty = 11.1$ and $M_\infty = 18.4$ in helium. As would be expected from the predicted insensitivity of blunt-body shock shapes and detachment distances with Mach number, the shock shape is very similar at all the Mach numbers of the tests, as shown in the side view schlieren photographs of figure 15. The shock is attached on the sharp-prow model and detached on the blunt-prow model as expected.

The shock shapes seen in the Mach number 6.8 and 9.6 top view photographs of the sharp-prow model (fig. 16(a)) are much the same; also the shock shape is not much different at Mach number 18.4 in helium. The sharp-prow model has a conical-shaped leading-edge shock. In the case of the blunt-prow model (fig. 16(b)), the first part of the shock emanating from the nose is the same as that on a sphere. However, in the region where this nose shock would strike the leading edge there is an interaction between the bow shock and the leading-edge detached shock characterized by the inflection which can readily be seen in the schlierens. The

leading edge is thus seen to play a significant part in the flow over the wing. Also, it can be seen from figure 16(b) that far enough away from the nose of the blunt-prow model the shock is parallel to the leading edge at $\alpha = 0^{\circ}$.

The shock shapes for the cylindrical-leading-edge models at angles of attack of 10°, 20°, 30°, and 40°, and at Mach numbers of 6.8 and 9.6 are presented in figures 17 to 20. The side view photographs indicate no appreciable change in the shock shape due to Mach number. At a Mach number of 9.6 and an angle of attack of 40° (figs. 18(a) and 18(b)) the model nose shock caused the tunnel-wall boundary layer to separate and engulf approximately one-half of the model. This tunnel-wall boundary-layer separation is also shown in the plan view photographs of figure 20. From the top view photographs, it can be seen that a conical shock existed on the sharp-prow model throughout the angle of attack and Mach number ranges of the tests. However, the shock shape for the blunt-prow model is different. If the extent of the nose influence is judged by the inflection in the leading-edge shock, the blunt nose affects less of the wing length as the angle of attack increases. Since the spherical nose has a shock of fixed shape, independent of angle of attack in the range shown, this change in shock shape is mainly due to changes in the shock around the cylindrical leading edge with angle of attack. Previously, it was shown that at a sufficient distance from the nose of the blunt-nose model, the shock is parallel to the leading edge at an angle of attack of 0°. (See fig. 16(b).) This is also true of the shock at an angle of attack of 10°. (See figs. 19(b) and 20(b).) At angles of attack of 20° and, to a more noticeable extent, at 30° and 40° the main-stream flow senses the local wing span and the leading-edge shock shape becomes conical in nature.

Schlieren studies at an angle of attack of 10° for a Mach number of 18.4 (helium) are presented in figure 21 and the shock shape is essentially the same as for the Mach number 6.8 and 9.6 tests in air.

Pressure Distribution on Wing

Pressure distribution at zero angle of attack.- The measured pressure distributions at an angle of attack of 0° on the sharp-nose and blunt-nose models at Mach numbers 6.8 and 9.6 in air and Mach number 18 in helium are presented in figure 22. The pressures in terms of free-stream static pressure are plotted against the nondimensional distance along the wing surface normal to the leading edge where t is the wing thickness. The short-dashed vertical lines at $s_o/t = \pm 0.785$ indicate the juncture of the leading edge and slab region. The value for $R_{\infty,t}$ shown here is the Reynolds number for the tests based on undisturbed free-stream conditions and wing thickness. The parameter L/t is the station along the leading edge measured from the apex of the slab portion of the wing. The solid symbols indicate points along the model center line. The decay in pressure along rays from the apex is evident and most clearly seen in the center-line data. This is the effect seen in the center-line presentation in figure 9. Qualitatively, the results in air and helium are similar. The maximum pressure on the leading edge is a factor of 5 to 10 higher than the pressure on the slab. The pressure on the slab is relatively constant at a given station, L/t, on the wing.

In the leading-edge region the pressure data of figure 22 are compared with empirical curves for essentially infinite cylinders shown by the solid line and for spheres given by the dashed line. These curves are fits to the hypersonic sphere and cylinder data discussed in a previous section. Remember that the $L/t = 0$ station is a line on a sphere. The leading-edge data for the sharp-prow models agree well with the correlated cylinder data except perhaps in the leading-edge—slab-juncture region. There are significant deviations from this correlated data for the blunt-prow model data. The correlated sphere data show reasonable agreement with the blunt-prow model data for the $L/t = 0$ station. The short-dashed line in the slab region in figure 22(a), blunt nose, $R_{\infty,t} = 2.4 \times 10^5$ is from data obtained on sphere-nose rods. The sphere-nose rod data underestimate the wing center-line data. A detailed comparison of rod data with data from this wing is contained in figure 13 of reference 1.

Pressure distribution at angle of attack.- The angle-of-attack pressure distributions for Mach numbers 6.8 and 9.6 in air and Mach number 18 in helium are presented in figures 23 to 27. The Mach number 9.6 data are presented for two Reynolds numbers. The pressure data are again plotted against surface distance normal to the leading edge of the wing. The surface distance is measured from the midline of the cylindrical leading edge. Positive s_o/t values indicate the windward surface of the wing and negative s_o/t, the leeward surface. The isolated cylinder data are again shown by the solid line and the sphere data, by the dashed line. Two-dimensional oblique-shock theory, Prandtl-Meyer expansion, and Newtonian theory for a sharp-leading-edge unswept plate at the same angle of attack as the wing are presented for reference purposes for the slab region. The correlated cylinder data give a good approximation to the leading-edge pressures for both the sharp- and blunt-prow models at Mach number 6.8 for the angles of attack of the test. (See figs. 23 and 24.) At higher Mach numbers ($M_\infty = 9.6$ and $M_\infty = 18$) the leading-edge data show fair agreement with the isolated cylinder data for the sharp-prow model. (See figs. 25 and 27.) For the blunt-prow models at the higher Mach numbers and the lower angles of attack ($\alpha < 25^\circ$), the measured pressures are below the correlated cylinder data (figs. 26 and 27); for the higher angles of attack fair agreement is shown. The leading-edge pressures at $L/t = 0$ for the blunt-prow model are approximated by correlated sphere data for the Mach numbers and angles of attack of the tests. The peak in pressure on the leading edge has disappeared at approximately $\alpha = 40^\circ$. (See figs. 23(d), 25(i), and 26(i).)

The pressures on the slab portion of the windward side of the wings at Mach number 6.8 (figs. 23 and 24) are relatively constant throughout the angle-of-attack range. For angles of attack from 5° to between 10° and 20°, the pressures are closely predicted by oblique-shock theory. A good approximation of the pressures at higher angles of attack was obtained from Newtonian theory. As discussed earlier, the pressure gradient induced by the blunt nose which was so pronounced at an angle of attack of 0° (fig. 22) becomes less severe with angle of attack and virtually disappears at an angle of attack of 20° and greater. Similar pressure-gradient effects are indicated at a Mach number of 9.6.

At a Mach number of 9.6, oblique-shock theory and Newtonian theory both underestimate the pressures on the slab portion of the high-pressure side of the

wings at the low angles of attack. (This lack of agreement is most evident in figs. 25(a), 25(b), 26(a), and 26(b).) At an angle of attack of 10° (figs. 25(c) and 26(c)), oblique-shock theory gives a reasonable prediction of the slab pressures whereas for the angle-of-attack range from 15° to 20° the pressures are overestimated by oblique-shock theory and slightly underestimated by Newtonian theory. For angles of attack greater than 25°, Newtonian theory agrees well with the slab pressures. Figure 27 presents the pressures on the slab portion of the wings at a Mach number of 18.4 (helium) at angles of attack of 5° and 10°. The results are similar to the air tests; however, the pressures in helium are about four times the air values. The leading-edge pressures for the sharp-prow model show good agreement with correlated cylinder data which overestimate the pressures on the blunt-prow model. Both Newtonian theory and oblique-shock theory underestimate the pressures on the slab portion of the wings for the low angles of attack studied in helium similar to the results obtained in air.

Stanton Number Distribution on Wing

Stanton number distribution at zero angle of attack.- The Stanton number distribution at an angle of attack of 0° on the models at Mach numbers of 6.8 and 9.6 are presented in figure 28. The vertical scale is the laminar-heating correlation parameter, Stanton number times the square root of Reynolds number based on wing thickness. As shown in figure 28, the data obtained are apparently laminar. The top and bottom sets of data differ mainly by the Reynolds numbers at which they were taken. Lees theory (ref. 12) for the heat-transfer distribution around a cylinder and a sphere by the integral method are shown in the leading-edge region. This distribution was used with the Fay and Riddell heating value for the stagnation point of an unswept cylinder (eq. (1)) utilizing as the initial velocity gradient $d(u/a_0)/d(s/t) = 2.19$ and the component Mach number normal to the leading edge. The empirical curve for pressure distribution in the leading-edge region shown in figure 22 was used in performing the integration. (See appendix.) The heating distribution is actually that shown in figure 4. Fair agreement with the appropriate theories is shown in the leading-edge region even though over most of the leading edge the known shock shape is not that to be expected for the infinite cylinder assumed in theory. (See fig. 16.)

On the slab, laminar strip theory (ref. 8) with zero pressure gradient and a pressure ratio of unity gives only a rough approximation of the heat transfer. The flow assumed in the strip-theory calculation is more or less streamwise and, as was shown in the surface flow studies (fig. 11), the surface flow directions are far from streamwise over a large portion of the wing. The heat transfer is higher along the wing center line (solid symbols) than on other parts of the slab surface at a given value of s_o/t.

Stanton number distribution at angle of attack.- Details of the heat-transfer-coefficient distribution at angle of attack are shown in figures 29 to 31. In figure 29 are shown the details of the $M_\infty = 6.8$ Stanton number distribution against distance normal to the leading edge at angles of attack of 10° to 46° for the blunt-nose model. Heat-transfer tests were not made on the sharp-nose model at $M_\infty = 6.8$. As at an angle of attack of 0°, fair agreement with the appropriate theories is shown in the leading-edge region for the angles of attack presented.

On the slab at an angle of attack of 10° (fig. 29(a)), the measured Stanton numbers are below the prediction of strip theory; however, at an angle of attack of 20° (fig. 29(b)) strip theory gives a reasonable approximation of the Stanton number distribution. Similarly, cross-flow theory agrees well with the measured data at an angle of attack of 20°. This cross-flow theory is obtained directly from equation (10) but is plotted against s_o rather than against s_c and strictly should be compared only with the solid symbols representing data on the center line of the slab part of the wing. At the higher angles of attack (figs. 29(c) to 29(e)), there is considerable discrepancy between the data and the cross-flow theory at the larger values of s_o/t. This discrepancy is believed to be due to boundary-layer transition which was discussed in an earlier section where only the heat transfer along the center line of the wing was considered. The detailed distribution in figure 29 indicates transition affects a large portion of the wing well off the center line.

The heat-transfer data for the sharp-nose model at a Mach number of 9.6 and various angles of attack are shown in figure 30. The swept cylinder predictions are somewhat below the measured Stanton numbers throughout the angle-of-attack range of the tests. At low angles of attack, strip theory overestimates the Stanton numbers on the slab. At angles of attack from 15° to 30° the measured heat-transfer data agree well with strip theory; however, the theory is below the data at $\alpha = 35^{\circ}$. Again, cross-flow theory gives a fair prediction of the Stanton numbers on the center line of the slab.

Figure 31 presents the heat-transfer-coefficient distribution on the blunt-nose model at a Mach number of 9.6 and for angles of attack from 2° to 41°. In the leading-edge region the agreement between the measured Stanton numbers and the theories improves with angle of attack. A large peak in heat transfer (figs. 31(h) and 31(i)) still occurs on the leading edge even though no such peak is noticeable in the pressure, especially at $\alpha = 41.5^{\circ}$. (See figs. 26(h) and 26(i).) This peak in heating can be an edge effect and cross-flow theory, if carried out spanwise for these ratios of edge radius to semispan, would give a peak near the edge. At an angle of attack of 20° (figs. 31(e) and 31(f)), there is reasonable agreement with strip and cross-flow theories on the slab. At the higher angles of attack the slab Stanton numbers show fair agreement with cross-flow theory but are overestimated by strip theory as was true of the sharp-nose model. At the conditions of the tests at a Mach number of 9.6, no consistent evidence of boundary-layer transition was obtained.

Aerodynamic Characteristics

The variation of the aerodynamic characteristics with angle of attack is shown in figures 32 and 33 for Mach number 6.8 and 9.6 tests in air. Because of tunnel-wall boundary-layer separation (see figs. 18 and 20), no data are presented at a Mach number of 9.6 for angles of attack greater than 30°. No data were obtained on the 21-diameter models $\left(t/c_r = 0.048\right)$ below an angle of attack of 15° because of induced loads caused by exposure of the conical adapter. The coefficients obtained from two-dimensional shock-expansion theory for a flat plate $\left(t/c_r = 0\right)$ and from modified Newtonian theory are presented for comparison with the test data. The measured lift coefficients for the 7-diameter models

$(t/c_r = 0.143)$ show good qualitative agreement with the modified Newtonian theory. (See figs. 32(a) and 33(a).) Shock-expansion theory gives relatively good agreement with the lift data only at the lower angles of attack. For the 21-diameter models $(t/c_r = 0.048)$ (figs. 32(b) and 33(b)), the measured lift coefficients are below the shock-expansion predictions and above modified Newtonian estimates and the results from the 7-diameter model.

Modified Newtonian predictions agree qualitatively with the measured drag coefficients for both the 7-diameter and the 21-diameter models.

At a Mach number of 6.8, $(L/D)_{max}$ occurred on the sharp-prow model at an angle of attack of approximately 16° and on the blunt-prow model at an angle of attack of approximately 22°. At a Mach number of 9.6, $(L/D)_{max}$ occurred on the sharp- and blunt-prow models at an angle of attack of about 24°.

CONCLUDING REMARKS

Results have been presented for a study of slab delta wings of 70° sweep at hypersonic Mach numbers. These wings had cylindrical leading edges and experiments were run with the nose formed by the intersection of the elements of the cylinders on the wing center line and with the nose blunted to a tangent sphere.

At the lower angles of attack the heat transfer to the leading edge of this delta wing was reasonably predicted by cylinder theory by using the component normal to the leading edge. At the highest angles of attack the heat transfer to the leading edge of the wing with the blunt nose (for which the highest angles of attack were obtained) was considerably less than that predicted by yawed cylinder theory. This drop-off in heat transfer appeared to be connected with an outward flow of air over the wing at high angles of attack.

The pressure and heat-transfer results obtained on the sphere nose appeared to be unaffected by the presence of the wing in the range of angle of attack studied (up to 46°).

For the slab portion of the wing, at low angles of attack, constant-pressure strip theory was poor in predicting the heat transfer. At angles of attack of 10° to 20°, strip theory gave a reasonable prediction of the test results. From 20° to the maximum test angle of attack, cross-flow theory gave good prediction of the heat transfer on the center line of the wing except for areas of the wing where transition is suspected to have occurred.

Much of the problem of predicting the heat transfer to delta wings is the changing flow pattern with angle of attack and simple approaches to predicting

the heat transfer are shown to be successful if the flow pattern peculiar to the angle-of-attack range under consideration is taken into account.

Langley Research Center,
National Aeronautics and Space Administration,
Langley Station, Hampton, Va., August 15, 1962.

APPENDIX

EVALUATION OF HEATING DISTRIBUTION ON TWO-DIMENSIONAL BLUNT NOSE BY LEES METHOD

For a two-dimensional blunt nose immersed in a perfect gas, Lees solution (ref. 12) may be written as

$$\frac{h}{h_0} = \frac{\sqrt{t}\,F(s)}{\sqrt{\frac{a_0}{u_\infty}\left(\frac{d(u/a_0)}{d(s/t)}\right)_0}} = \frac{\sqrt{t}\,F(s)}{\sqrt{\frac{1}{M_\infty}\left(\frac{T_0}{T_\infty}\right)^{1/2}\left(\frac{d(u/a_0)}{d(s/t)}\right)_0}} \tag{A1}$$

where

$$\sqrt{t}\,F(s) = \frac{1}{\sqrt{2}} \frac{\frac{p}{p_0}\frac{1}{C_e}\frac{u}{u_\infty}}{\left[\int_0^{s/t} \frac{p}{p_0}\frac{u}{u_\infty}\frac{1}{C_e}\,d\left(\frac{s}{t}\right)\right]^{1/2}} \tag{A2}$$

in which

$$\frac{u}{u_\infty} = \frac{u}{a_0}\frac{1}{M_\infty}\sqrt{\frac{T_0}{T_\infty}}$$

$$\frac{u}{a_0} = \sqrt{\frac{2}{\gamma - 1}\left[1 - \left(\frac{p}{p_0}\right)^{\frac{\gamma-1}{\gamma}}\right]}$$

$$C_e = \frac{\mu_0}{\mu}\frac{T}{T_0}$$

$$\frac{T}{T_0} = 1 - \frac{\gamma - 1}{2}\left(\frac{u}{a_0}\right)^2$$

for air with the Sutherland law

$$C_e = \sqrt{\frac{T_0}{T}}\,\frac{T + 198(^\circ F)}{T_0 + 198(^\circ F)}$$

An exact solution of equation (A2) generally requires a graphical evaluation of the integral in equation (A2).

If the velocity distribution is assumed to be linear (see figs. 6(c) and 8(b)), then with $s/t = \phi/2$

$$\frac{u}{u_\infty} = \frac{1}{u_\infty}\left(\frac{du}{d\phi}\right)_0 \phi$$

and with C_e assumed to be constant, equation (A1) reduces to

$$\frac{h}{h_0} = \frac{\frac{p}{p_0}\phi}{\sqrt{2\int_0^\phi \frac{p}{p_0}\phi\, d\phi}} \tag{A3}$$

If the pressure distribution over the two-dimensional nose is assumed to be represented by an equation of the form

$$\frac{p}{p_0} = \cos^2\phi + b\,\sin^2\phi + c\phi^n \tag{A4}$$

upon substitution of equation (A4) into and the integration of equation (A3) the following result is obtained:

$$\frac{h}{h_0} = \frac{\sqrt{2}\left[1 - (1 - b)\sin^2\phi + c\phi^n\right]\phi}{\sqrt{(1 - b)\left(\phi\,\sin 2\phi - \sin^2\phi\right) + \phi^2\left(\frac{4c}{n + 2}\phi^n + 1 + b\right)}} \tag{A5}$$

According to the Newtonian approximation adopted by Lees, $b = \left(\gamma M_\infty^2\right)^{-1}$ and $c = 0$. In the present case, the values of b, c, and n which accurately represented the pressure distribution on a cylinder for $M_\infty \geq 4$ were found to be for $0 \leq \phi \leq 90^\circ$

$$b = 0.16$$

$$c = -0.00665$$

$$n = 5$$

These values are the values used in obtaining the heat-transfer-coefficient distribution, shown in figure 4, by equation (A5) and by evaluating the integral in equation (A2) graphically. This pressure distribution is not a strong function of Mach number; for example, for $M_\infty \approx 3$ the following values were found to give a good fit to the pressure data (compare with fig. 3 after insertion in eq. (4)) for $0 \leqq \phi \leqq 100^\circ$

$$b = 0.167$$

$$c = -0.00268$$

$$n = 7$$

REFERENCES

1. Bertram, Mitchel H., and Henderson, Arthur, Jr.: Recent Hypersonic Studies of Wings and Bodies. ARS Jour., vol. 31, no. 8, Aug. 1961, pp. 1129-1139.

2. McLellan, Charles H., Williams, Thomas W., and Bertram, Mitchel H.: Investigation of a Two-Step Nozzle in the Langley 11-Inch Hypersonic Tunnel. NACA TN 2171, 1950.

3. Bertram, Mitchel H.: Exploratory Investigation of Boundary-Layer Transition on a Hollow Cylinder at a Mach Number of 6.9. NACA Rep. 1313, 1957. (Supersedes NACA TN 3546.)

4. Bertram, Mitchel H.: Boundary-Layer Displacement Effects in Air at Mach Numbers of 6.8 and 9.6. NASA TR R-22, 1959. (Supersedes NACA TN 4133.)

5. Henderson, Arthur, Jr., and Baradell, Donald L.: Recent Work at Langley Research Center in the Development of Hypersonic Helium Tunnels. Proc. Nat. Symposium on Hypervelocity Techniques, Inst. Aero. Sci., Oct. 1960, pp. 131-141.

6. Eckert, E. R. G., and Drake, Robert M., Jr.: Heat and Mass Transfer. Second ed., McGraw-Hill Book Co., Inc., 1959.

7. Hodgman, Charles D., Weast, Robert C., and Selby, Samuel M., eds.: Handbook of Chemistry and Physics. Thirty-eighth ed., Chemical Rubber Pub. Co., 1956-1957, pp. 2086, 2251, and 2252.

8. Bertram, Mitchel H., and Feller, William V.: A Simple Method for Determining Heat Transfer, Skin Friction, and Boundary-Layer Thickness for Hypersonic Laminar Boundary-Layer Flows in a Pressure Gradient. NASA MEMO 5-24-59L, 1959.

9. Penland, Jim A.: Aerodynamic Characteristics of a Circular Cylinder at Mach Number 6.86 and Angles of Attack up to 90°. NACA TN 3861, 1957. (Supersedes NACA RM L54A14.)

10. Beckwith, Ivan E., and Gallagher, James J.: Experimental Investigation of the Effect of Boundary-Layer Transition on the Average Heat Transfer to a Yawed Cylinder in Supersonic Flow. NACA RM L56E09, 1956.

11. Beckwith, Ivan E., and Gallagher, James J.: Local Heat Transfer and Recovery Temperatures on a Yawed Cylinder at a Mach Number of 4.15 and High Reynolds Numbers. NASA TR R-104, 1961. (Supersedes NASA MEMO 2-27-59L.)

12. Lees, Lester: Laminar Heat Transfer Over Blunt-Nosed Bodies at Hypersonic Flight Speeds. Jet Propulsion, vol. 26, no. 4, Apr. 1956, pp. 259-269, 274.

13. Fay, J. A., and Riddell, F. R.: Theory of Stagnation Point Heat Transfer in Dissociated Air. Jour. Aero. Sci., vol. 25, no. 2, Feb. 1958, pp. 73-85, 121.

14. Crawford, Davis H., and McCauley, William D.: Investigation of the Laminar Aerodynamic Heat-Transfer Characteristics of a Hemisphere-Cylinder in the Langley 11-Inch Hypersonic Tunnel at a Mach Number of 6.8. NACA Rep. 1323, 1957. (Supersedes NACA TN 3706.)

15. Reshotko, Eli, and Cohen, Clarence B.: Heat Transfer at the Forward Stagnation Point of Blunt Bodies. NACA TN 3513, 1955.

16. Oliver, Robert E.: An Experimental Investigation of Flow Over Simple Blunt Bodies at a Nominal Mach Number of 5.8. GALCIT Memo. No. 26 (Contract No. DA-04-495-Ord-19), June 1, 1955.

17. Machell, Reginald M., and O'Bryant, William T.: An Experimental Investigation of the Flow Over Blunt-Nosed Cones at a Mach Number of 5.8. GALCIT Memo. No. 32 (Contract No. DA-04-495-Ord 19), June 15, 1956.

18. Beckwith, Ivan E., and Gallagher, James J.: Heat Transfer and Recovery Temperatures on a Sphere With Laminar, Transitional, and Turbulent Boundary Layers at Mach Numbers of 2.00 and 4.15. NACA TN 4125, 1957.

19. Kendall, James M., Jr.: Experiments on Supersonic Blunt-Body Flows. Progress Rep. No. 20-372 (Contract No. DA-04-495-Ord 18), Jet Propulsion Lab., C.I.T., Feb. 27, 1959.

20. Baer, A. L.: Pressure Distributions on a Hemisphere Cylinder at Supersonic and Hypersonic Mach Numbers. AEDC-TN-61-96 (Contract No. AF 40(600)-800 S/A 24(61-73)), Arnold Eng. Dev. Center, Aug. 1961.

21. Vas, I. E., Bogdonoff, S. M., and Hammitt, A. G.: An Experimental Investigation of the Flow Over Simple Two-Dimensional and Axial Symmetric Bodies at Hypersonic Speeds. Rep. No. 382 (WADC TN 57-246), Dept. Aero. Eng., Princeton Univ., June 1957.

22. Wagner, Richard D., Jr., Pine, W. Clint, and Henderson, Arthur, Jr.: Laminar Heat-Transfer and Pressure-Distribution Studies on a Series of Reentry Nose Shapes at a Mach Number of 19.4 in Helium. NASA TN D-891, 1961.

23. Cooper, Morton, and Mayo, Edward E.: Measurements of Local Heat Transfer and Pressure on Six 2-Inch-Diameter Blunt Bodies at a Mach Number of 4.95 and at Reynolds Numbers per Foot up to 81×10^6. NASA MEMO 1-3-59L, 1959.

24. Julius, Jerome D.: Experimental Pressure Distributions Over Blunt Two- and Three-Dimensional Bodies Having Similar Cross Sections at a Mach Number of 4.95. NASA TN D-157, 1959.

25. Beckwith, Ivan E., and Cohen, Nathaniel B.: Application of Similar Solutions to Calculation of Laminar Heat Transfer on Bodies With Yaw and Large Pressure Gradient in High-Speed Flow. NASA TN D-625, 1961.

26. Ferri, Antonio: A Review of Some Recent Developments in Hypersonic Flow. WADC Tech. Note 58-230, ASTIA Doc. No. AD 155822, U.S. Air Force, Sept. 1958.

27. Hastings, S. M., Persh, J., and Redman, E. J.: Experimental Investigation of the Pressure Distribution on Axi-Symmetric Flat-Face Cone-Type Bodies at Supersonic and Hypersonic Speeds, NAVORD Rep. 5659 (Aerodynamics Res. Rep. 3), U.S. Naval Ord. Lab. (White Oak, Md.), Oct. 1, 1957.

28. Shutts, William Holland: Characteristics of Flow Around Blunted Cones With Axial Symmetry at Supersonic Speeds. DRL-417, CM-920 (Contract NOrd-16498), Univ. of Texas, May 1958.

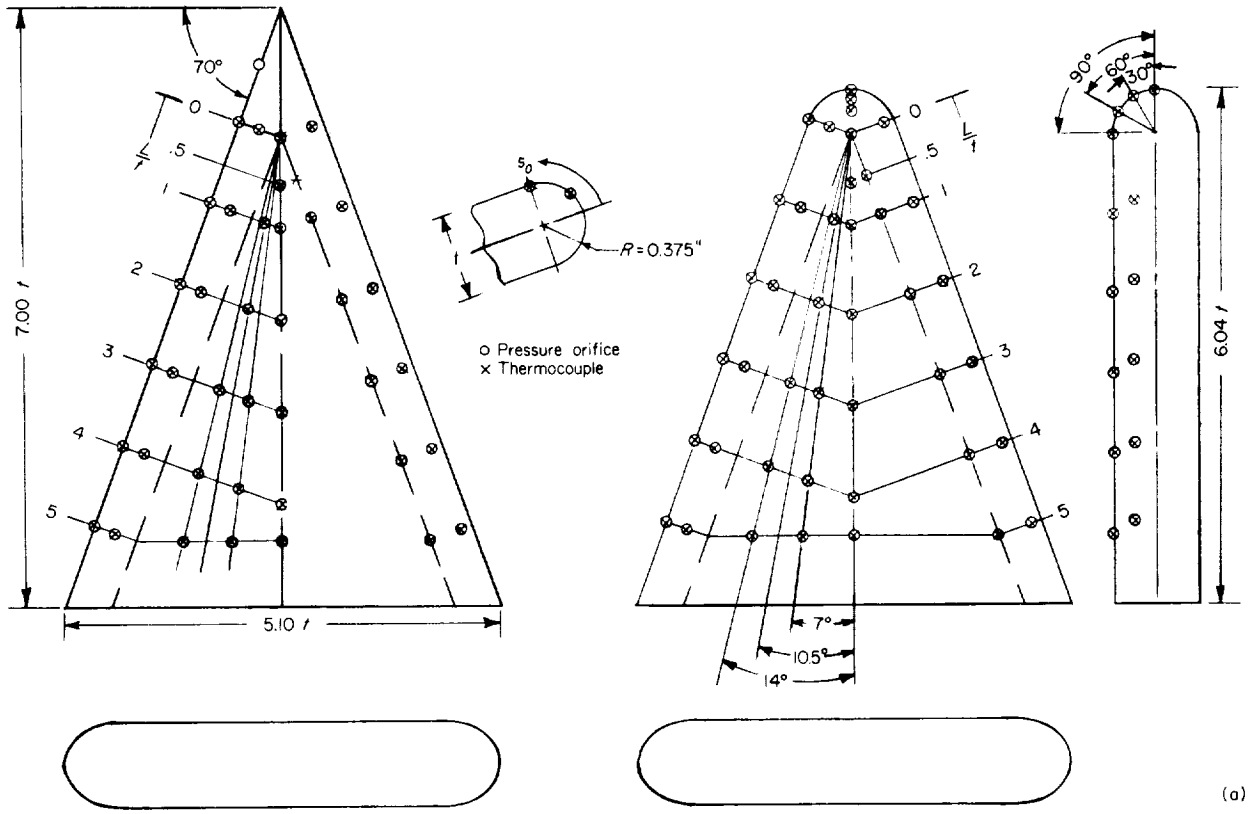

(a) Sketch of pressure and heat-transfer models.

Figure 1.- Models.

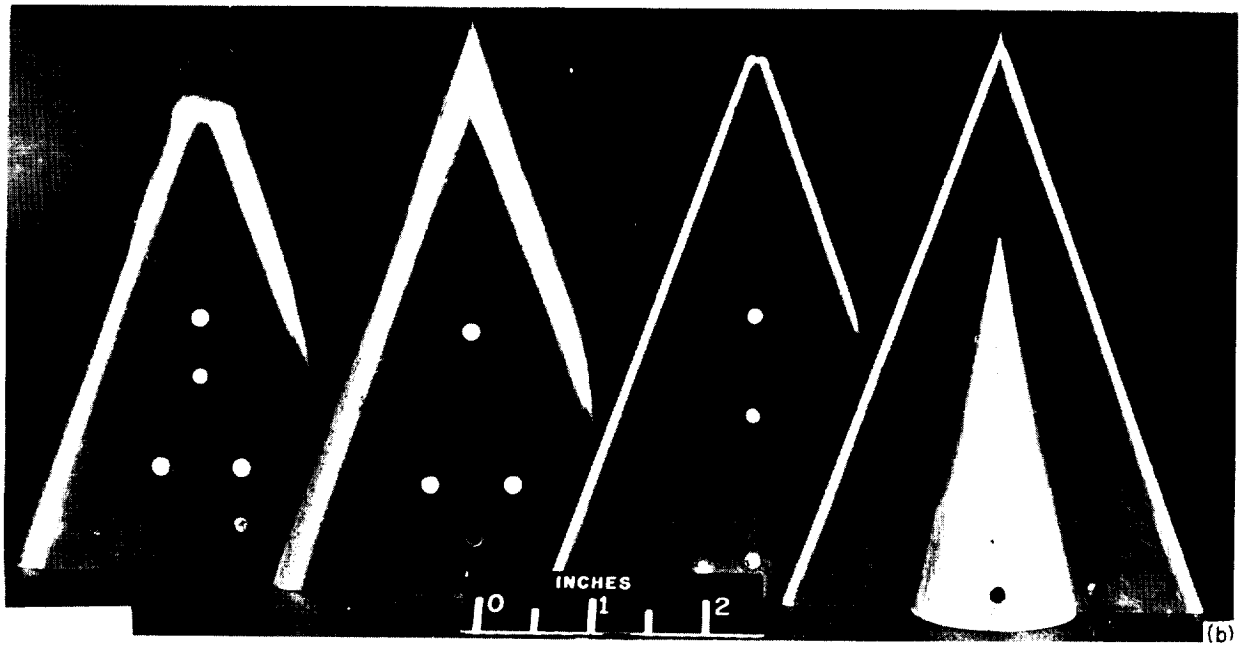

L-61-7442

(b) Photographs of solid models used for oil-flow and force characteristics.

Figure 1.- Continued.

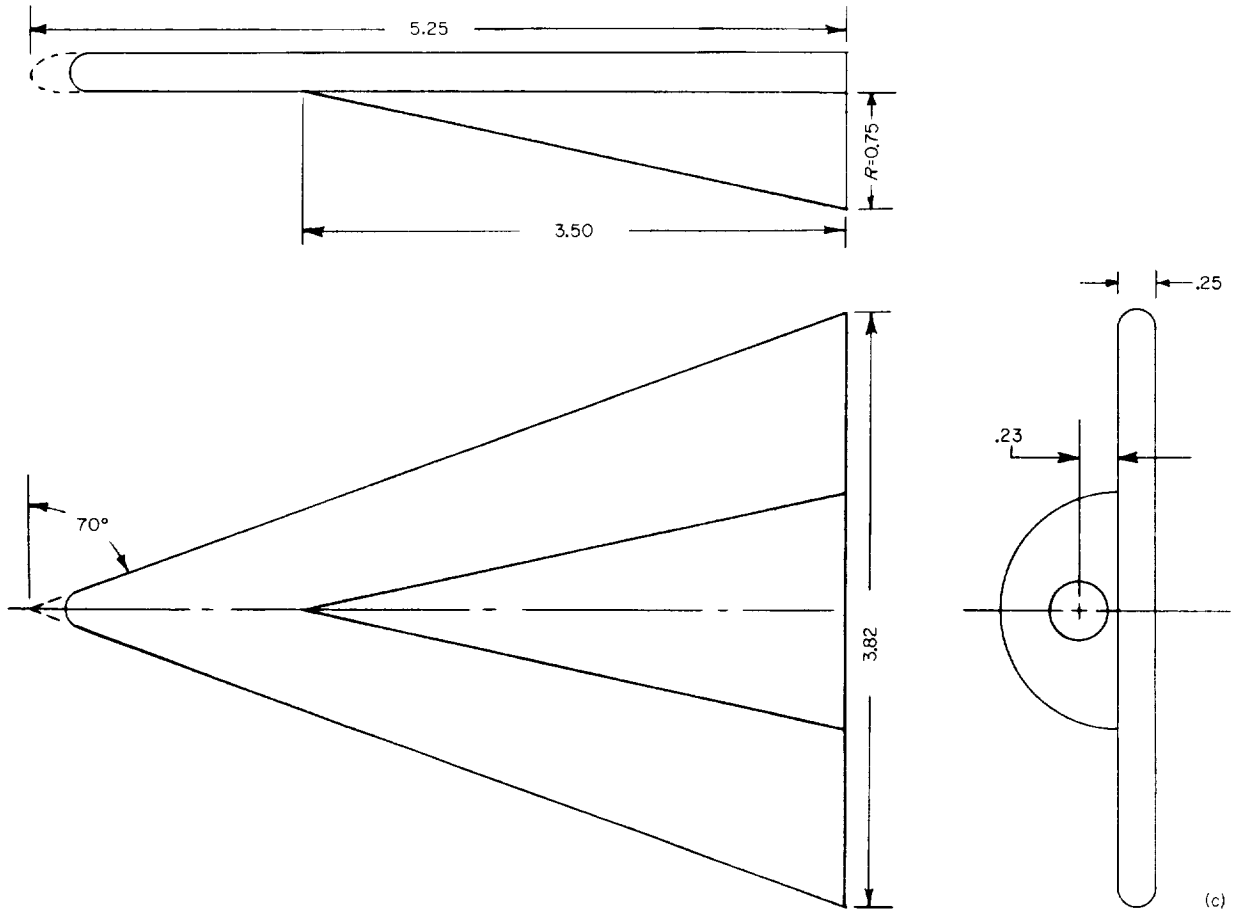

(c) Sketch of 21-diameter force and oil-flow models.

Figure 1.- Concluded.

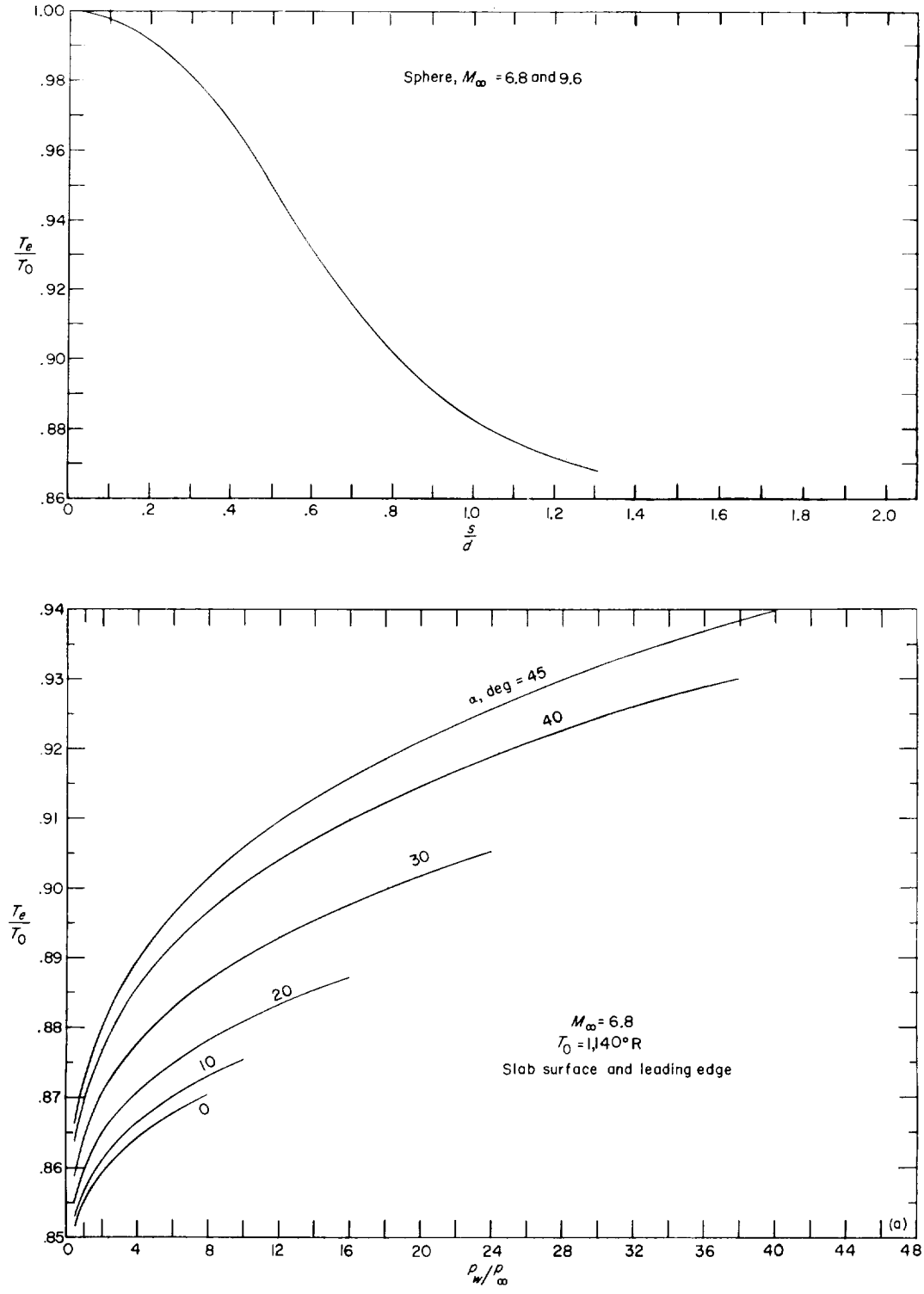

(a) Sphere nose, slab surface, and leading edge at $M_\infty = 6.8$.

Figure 2.- Adiabatic wall temperatures used in reducing test results.

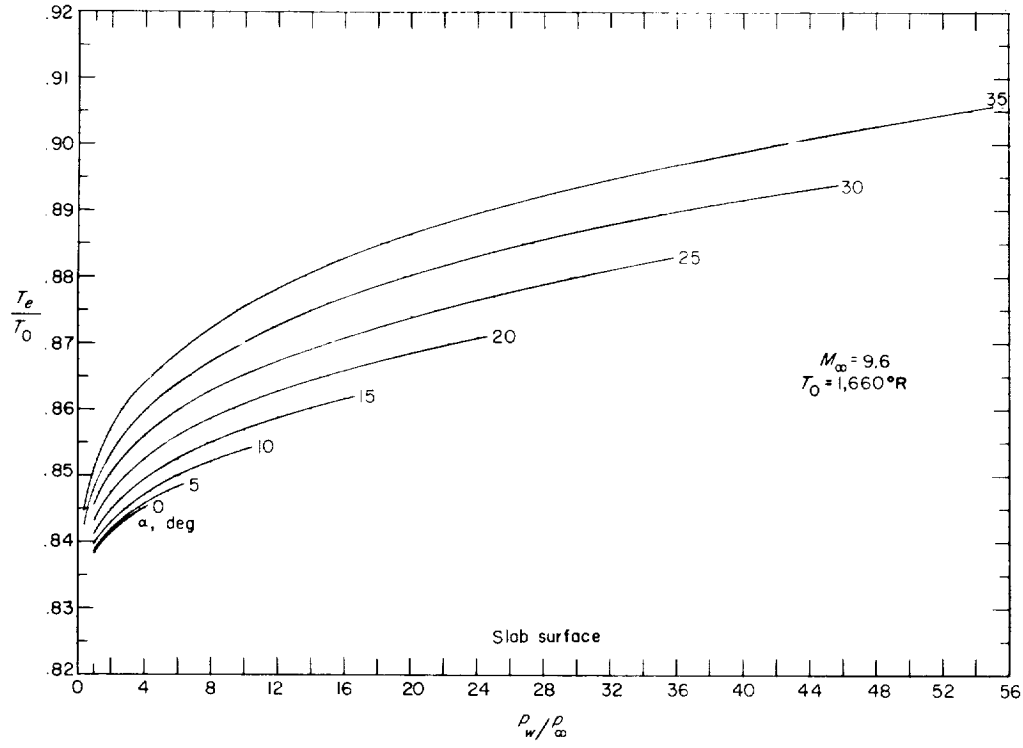

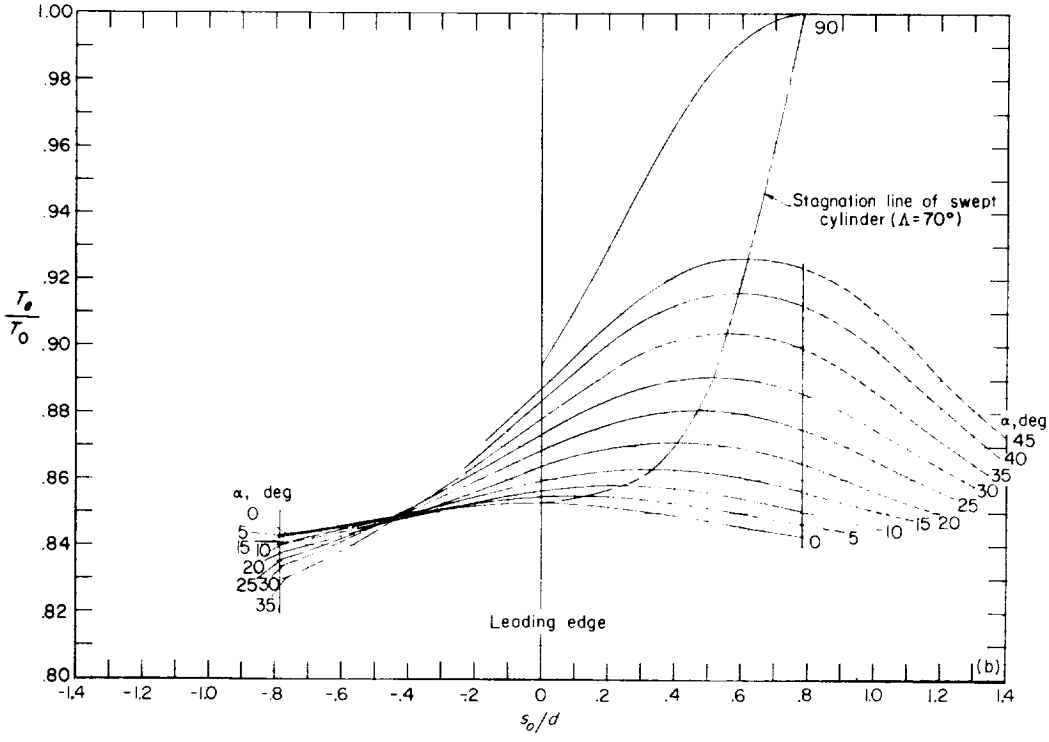

(b) Slab surface and leading edge at $M_\infty = 9.6$.

Figure 2.- Concluded.

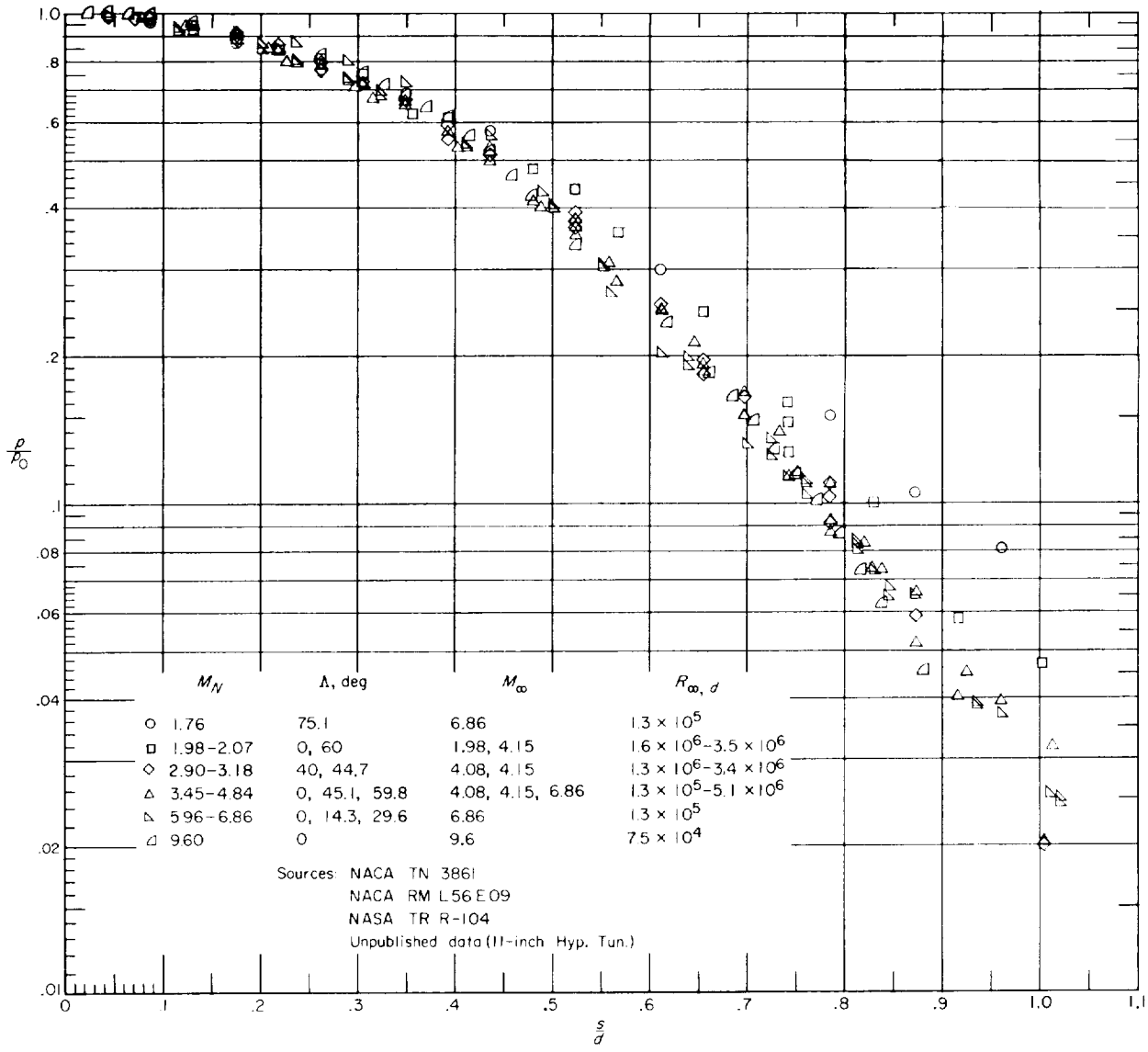

Figure 3.- Pressure distribution on cylinder in air.

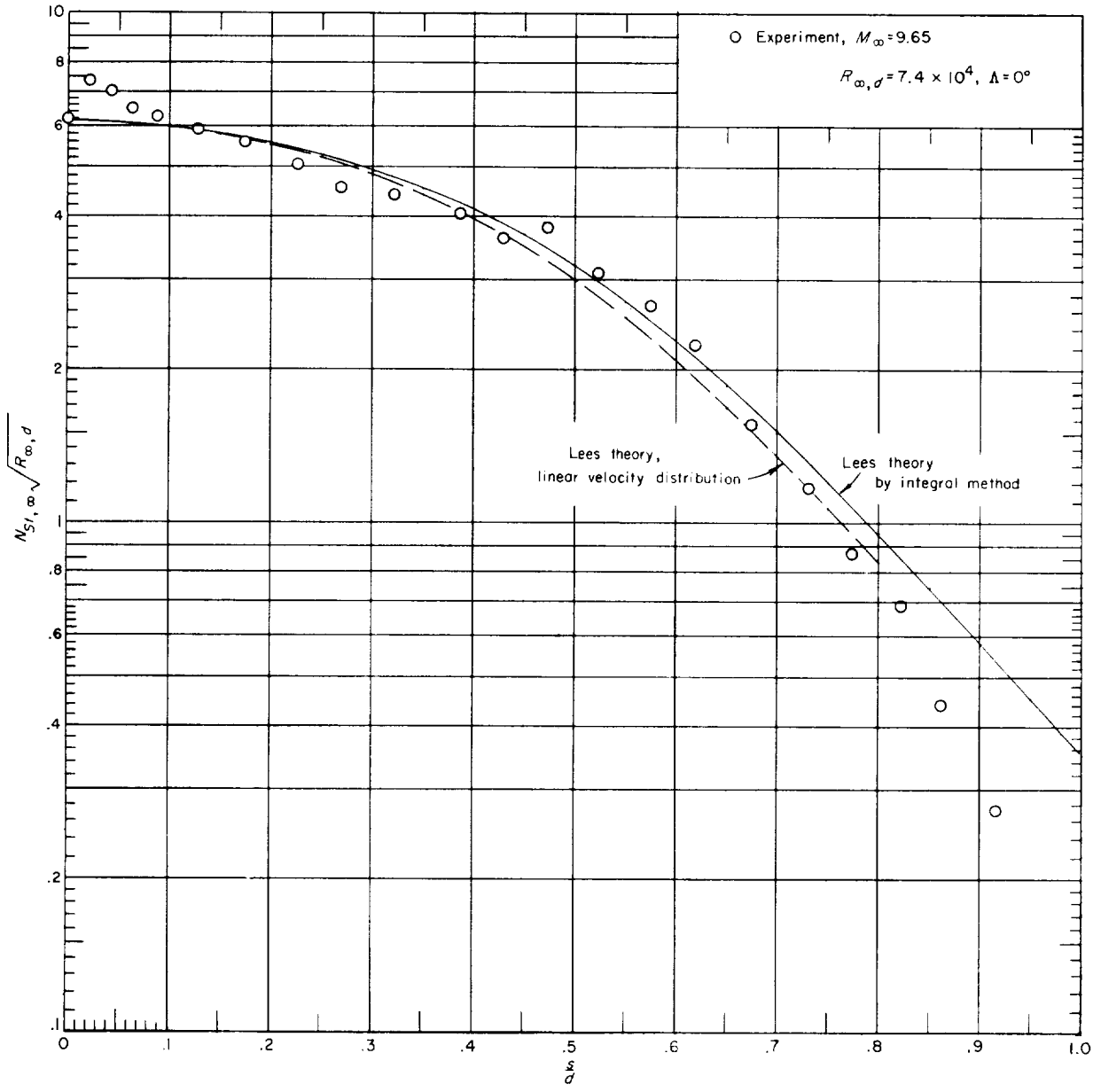

Figure 4.- Stanton number distribution on cylinder in air.

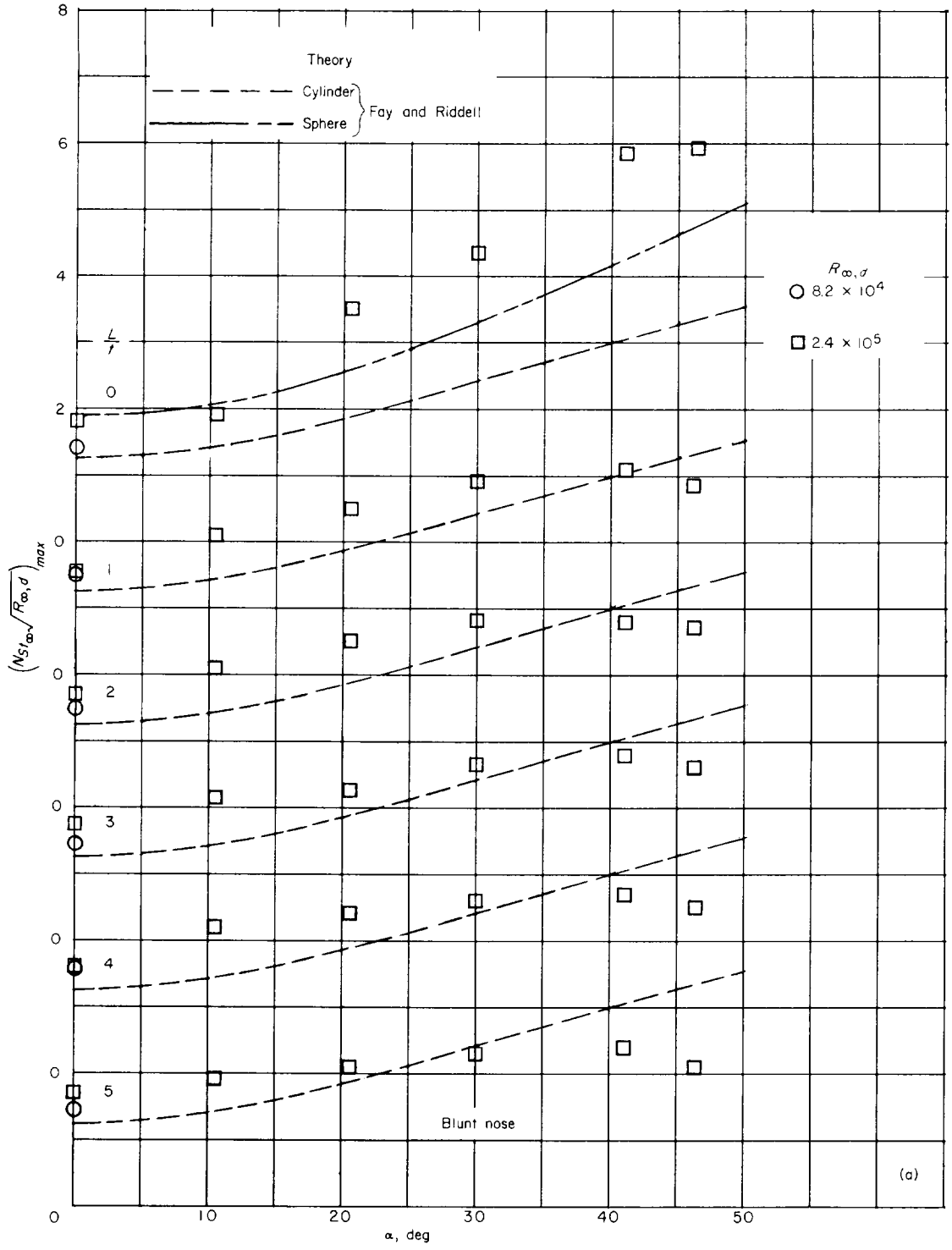

(a) $M_\infty = 6.8$.

Figure 5.- Maximum Stanton numbers measured at various locations along the leading edge of delta wing.

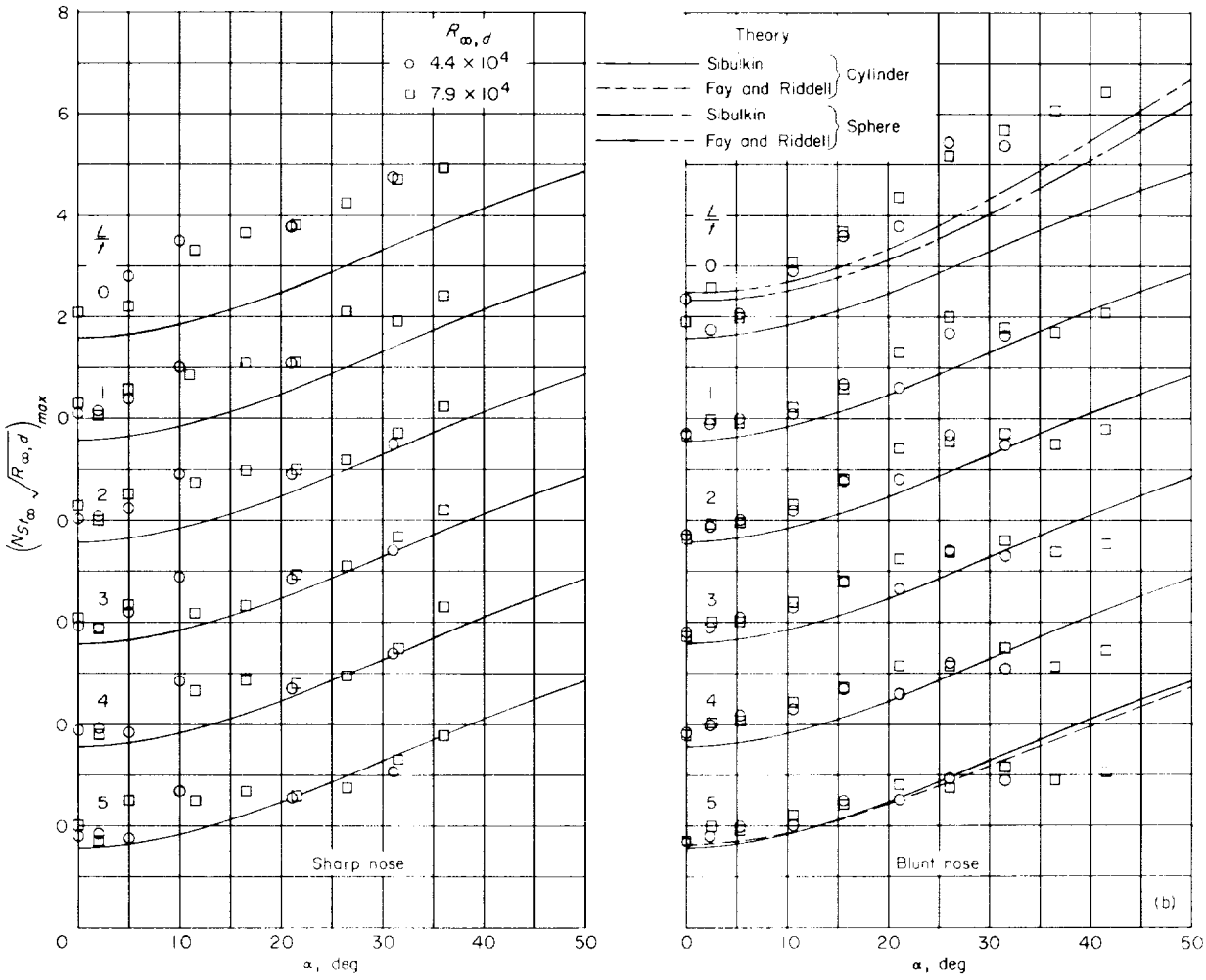

(b) $M_\infty = 9.6$.

Figure 5.- Concluded.

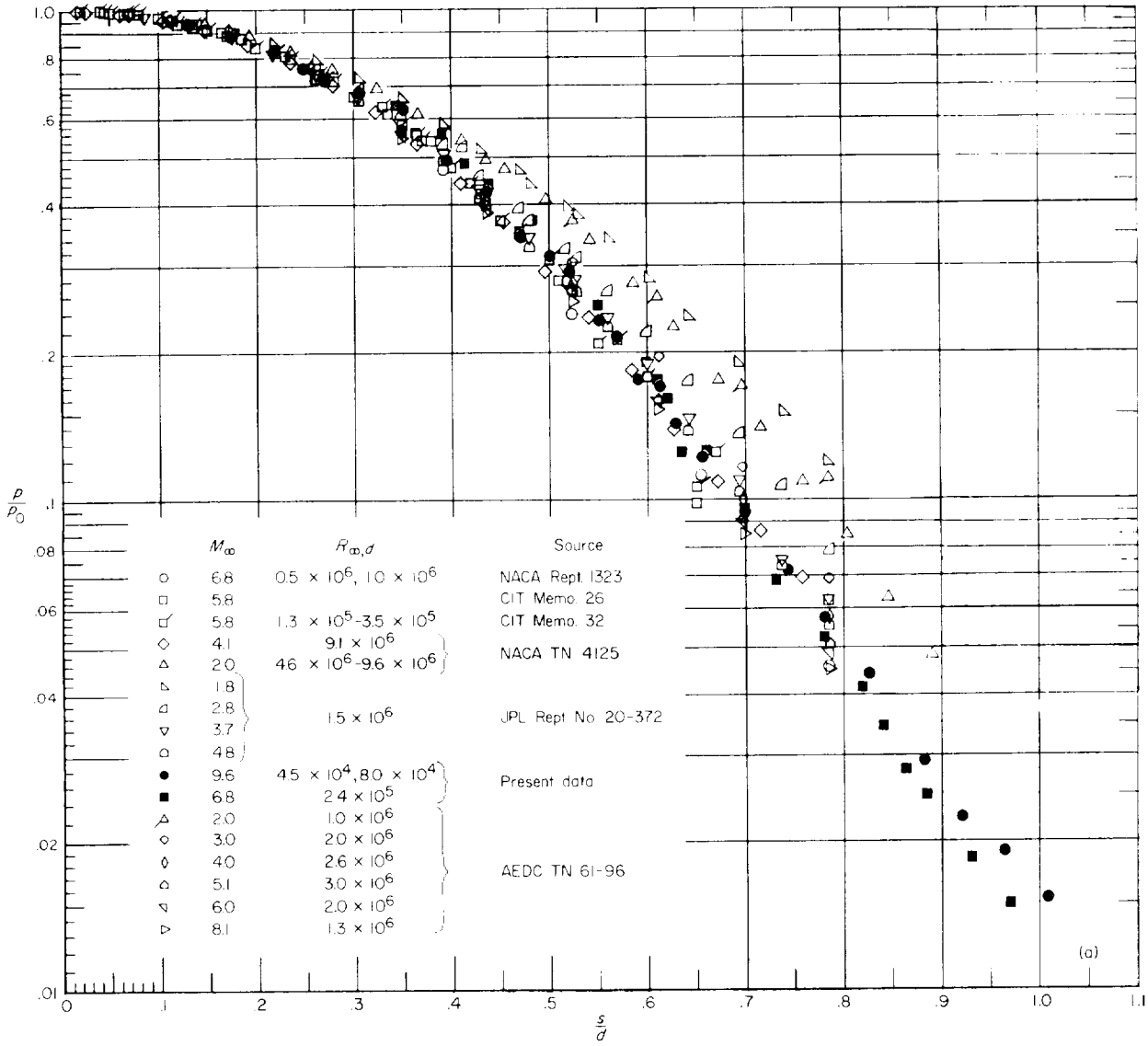

(a) Collected data.

Figure 6.- Pressure distributions on sphere in air.

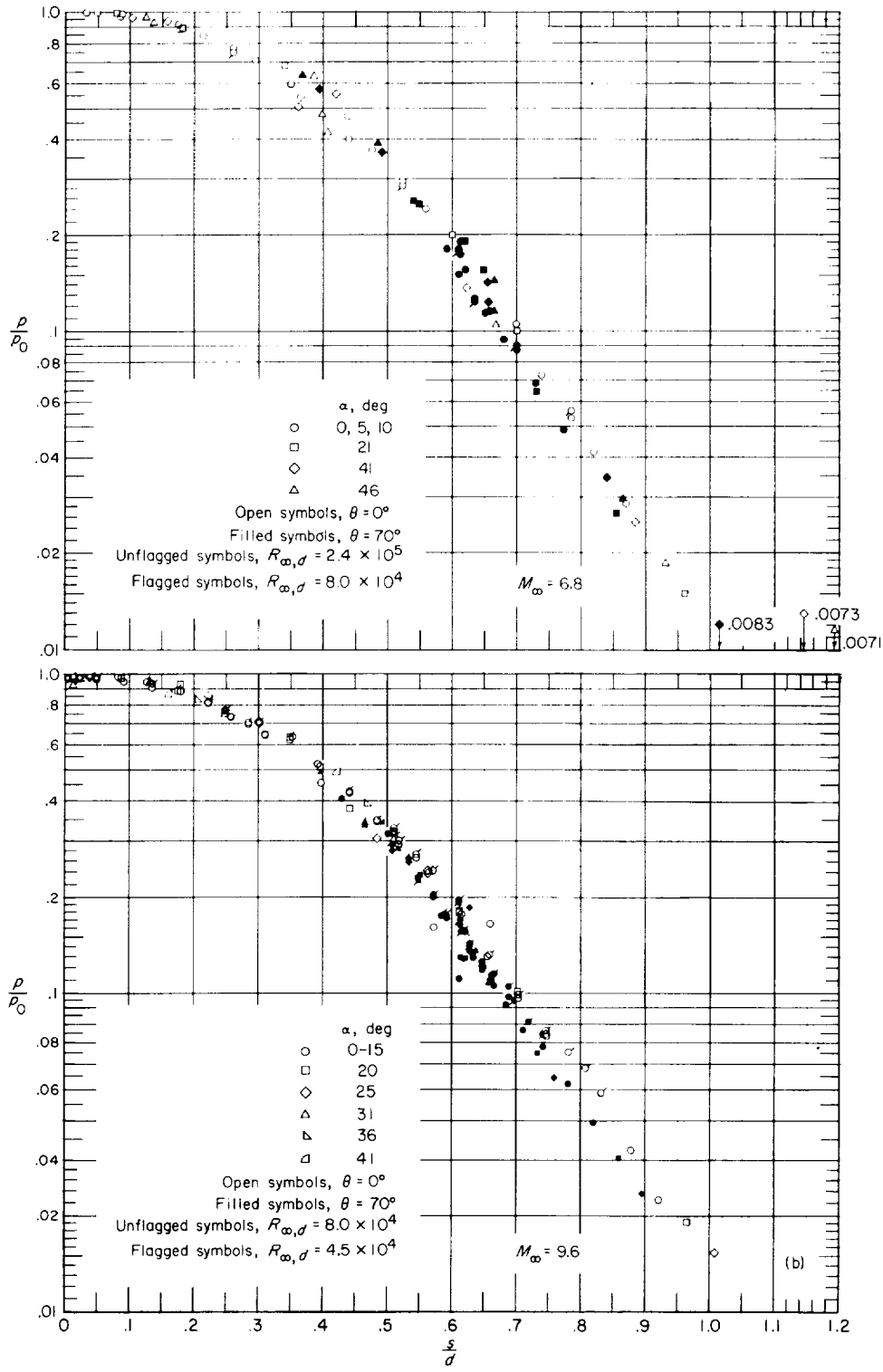

(b) Details of present data on sphere nose.

Figure 6.- Continued.

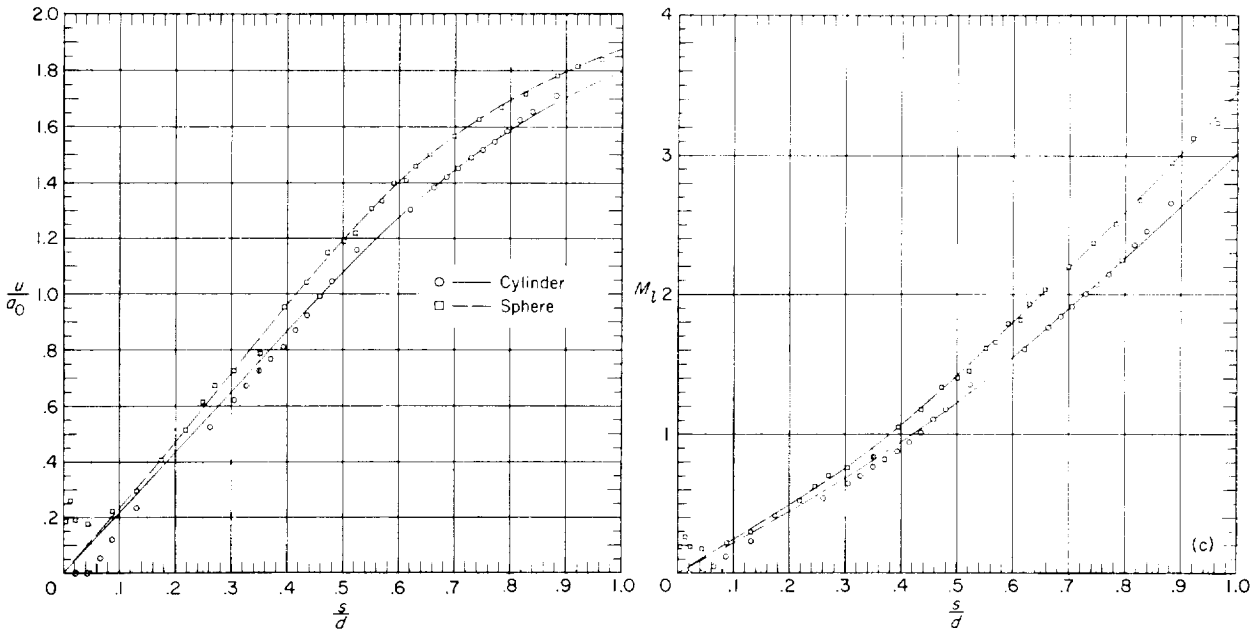

(c) Velocity and Mach number distribution on cylinder and sphere. Data designated by symbols are for $M_\infty = 9.6$.

Figure 6.- Concluded.

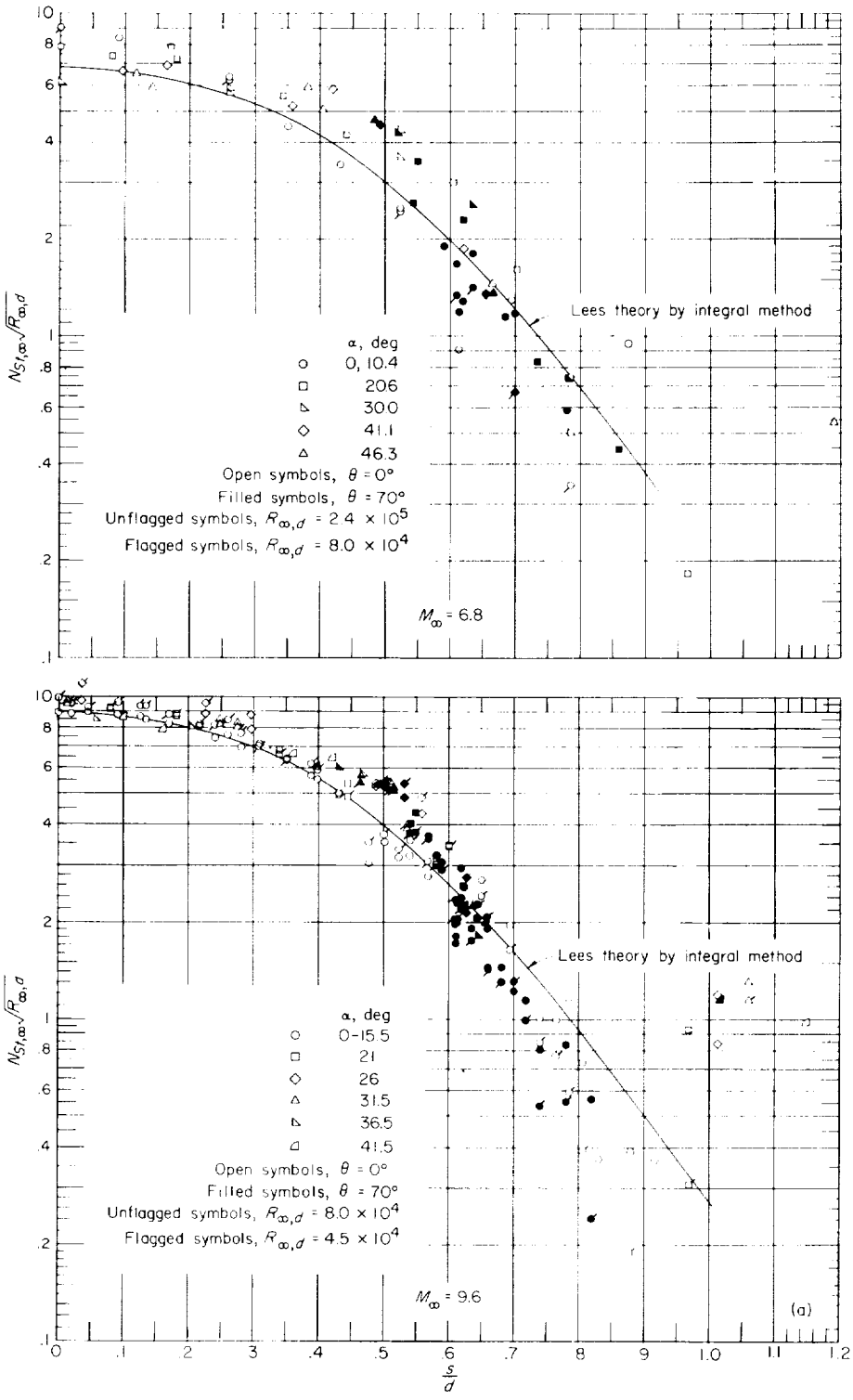

(a) Details of present data on sphere nose.

Figure 7.- Stanton number distribution on sphere in air.

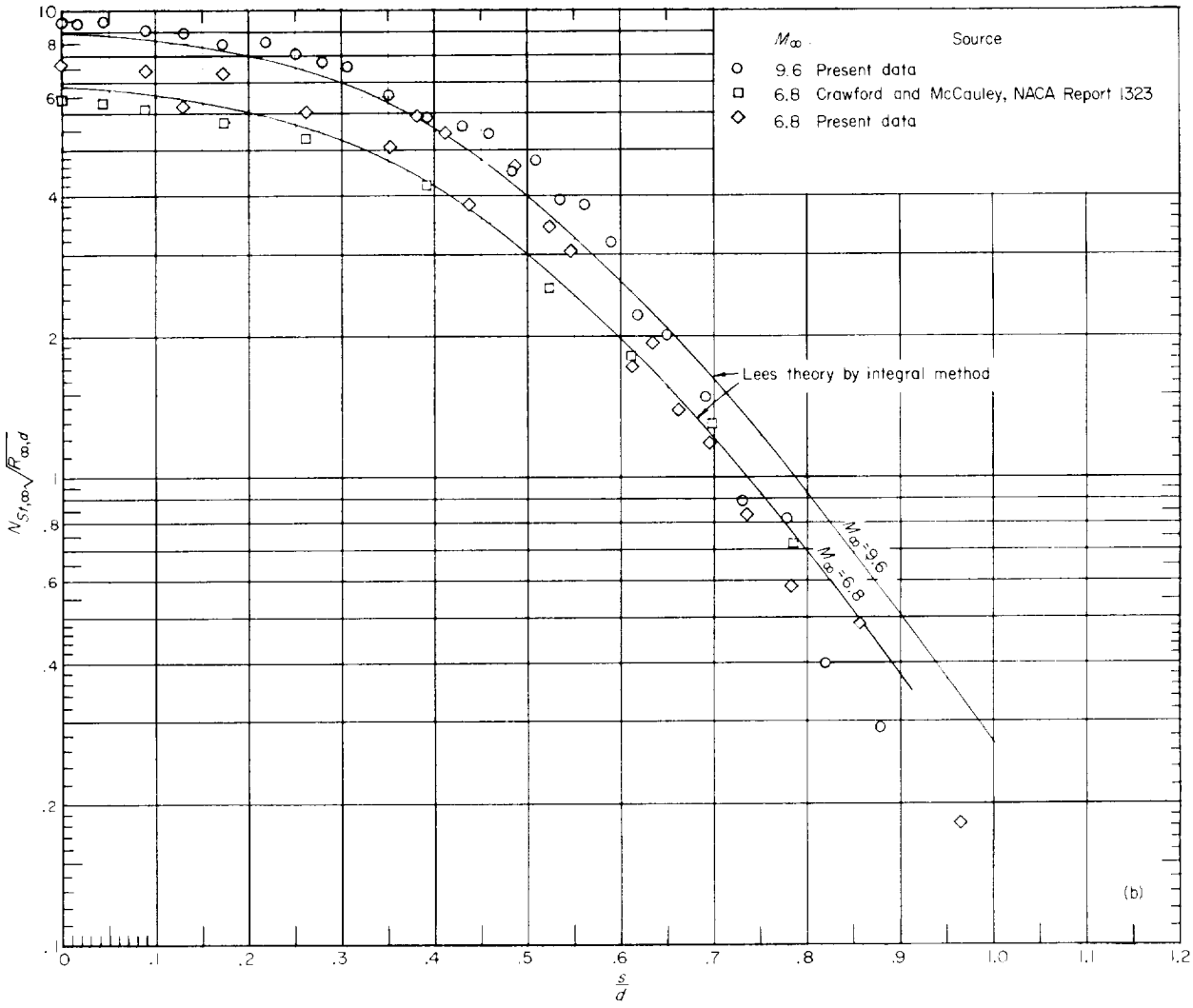

(b) Averaged values of present data compared with previous data.

Figure 7.- Concluded.

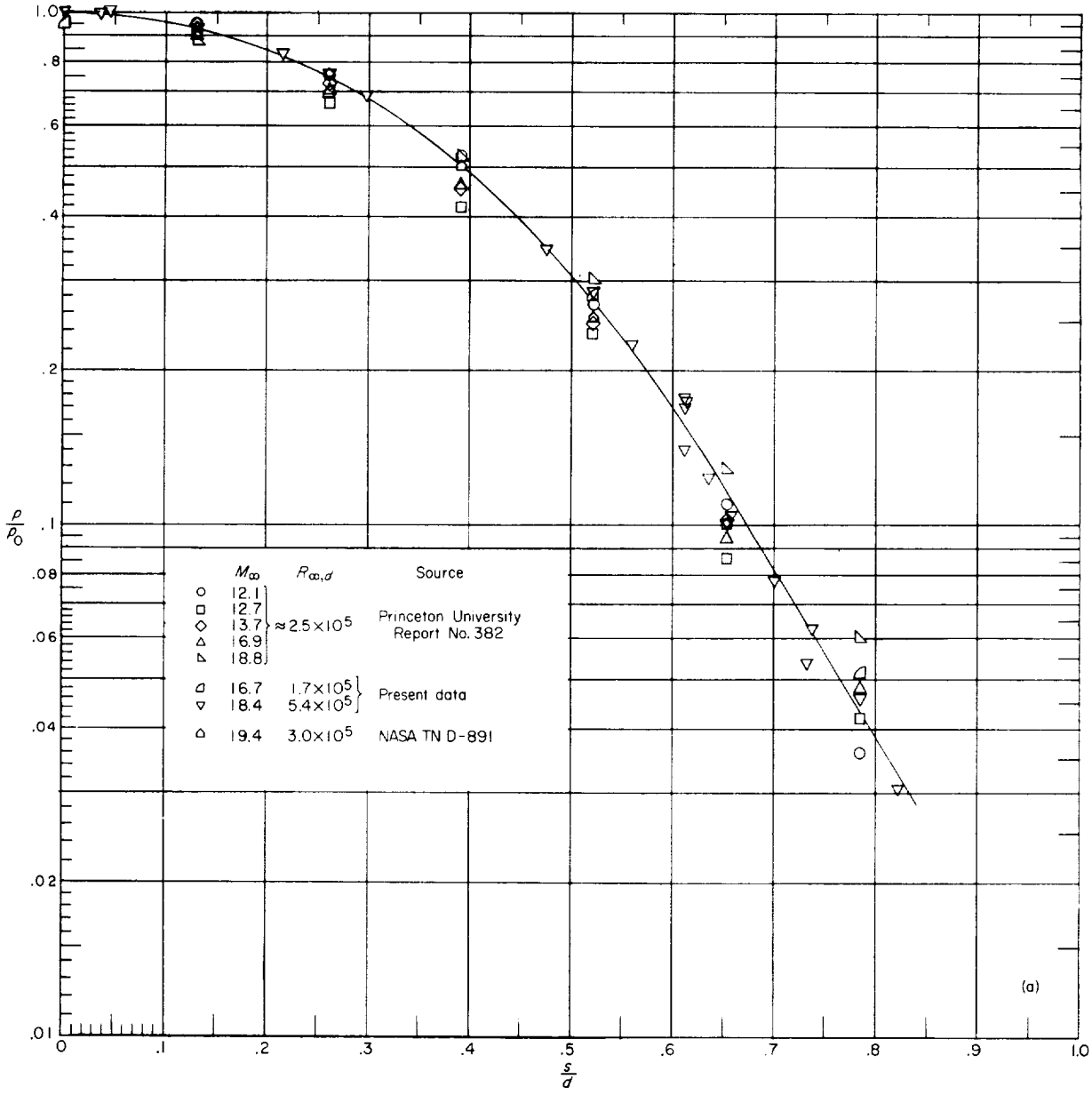

(a) Collected pressure data.

Figure 8.- Pressure, Mach number, and velocity distribution on sphere in helium.

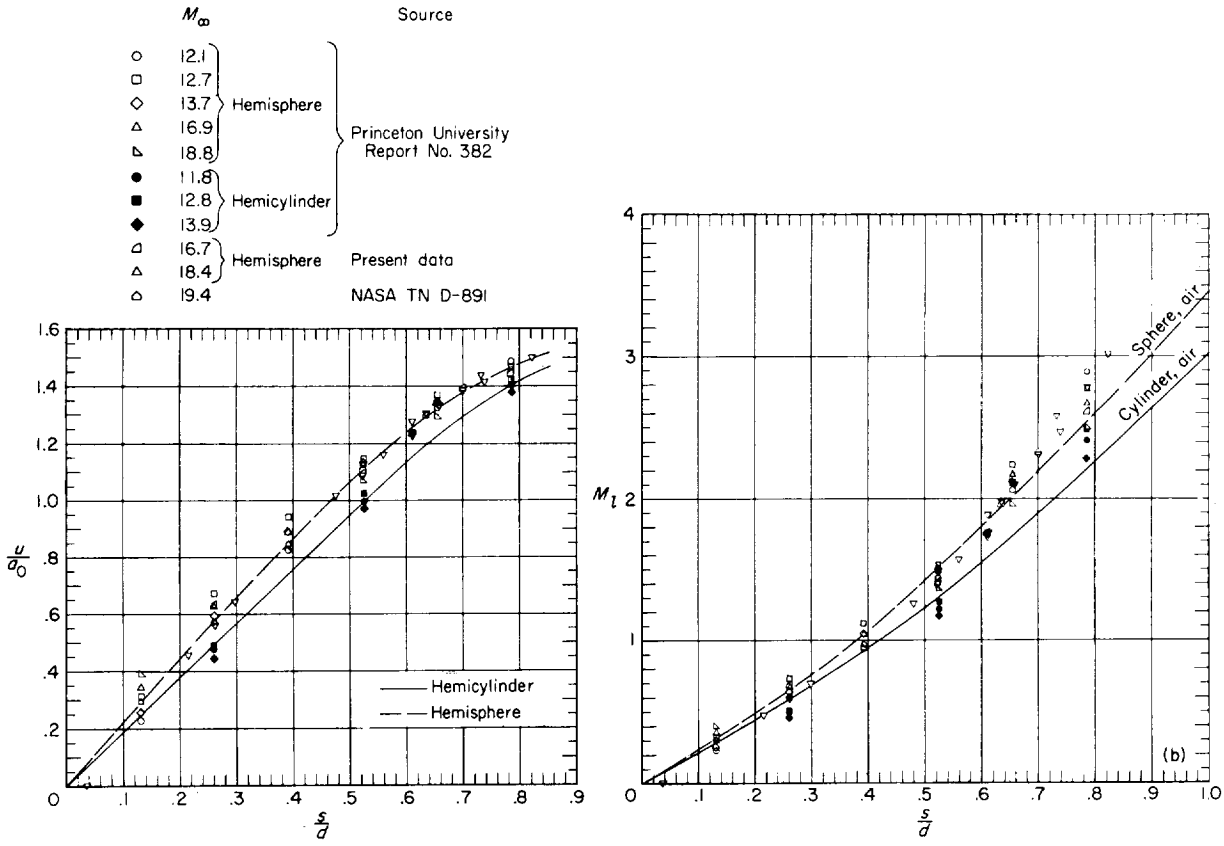

(b) Velocity and Mach number.

Figure 8.- Concluded.

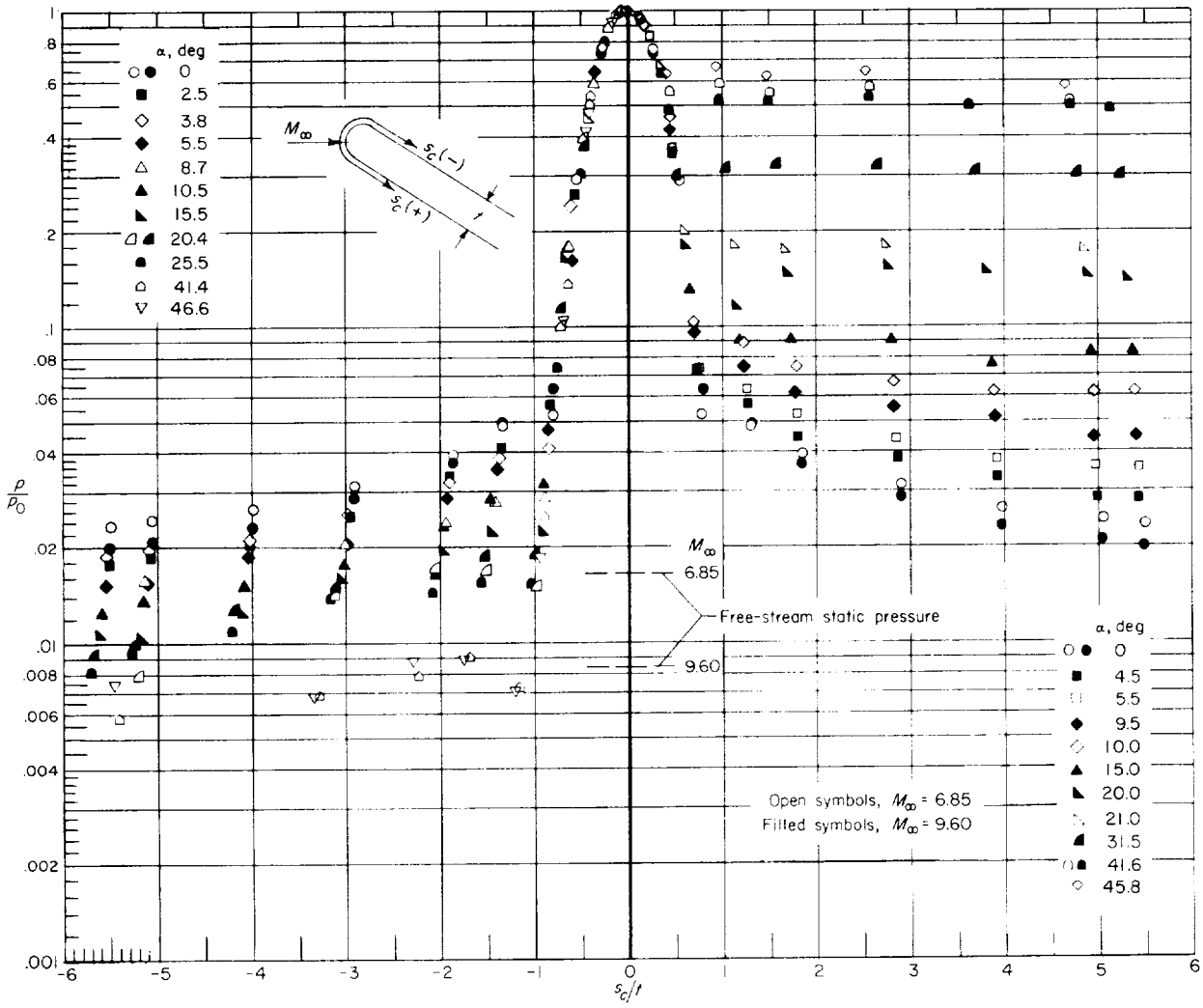

Figure 9.- Center-line distribution of pressure on spherical-nose slab delta wing. $\Lambda = 70^\circ$.

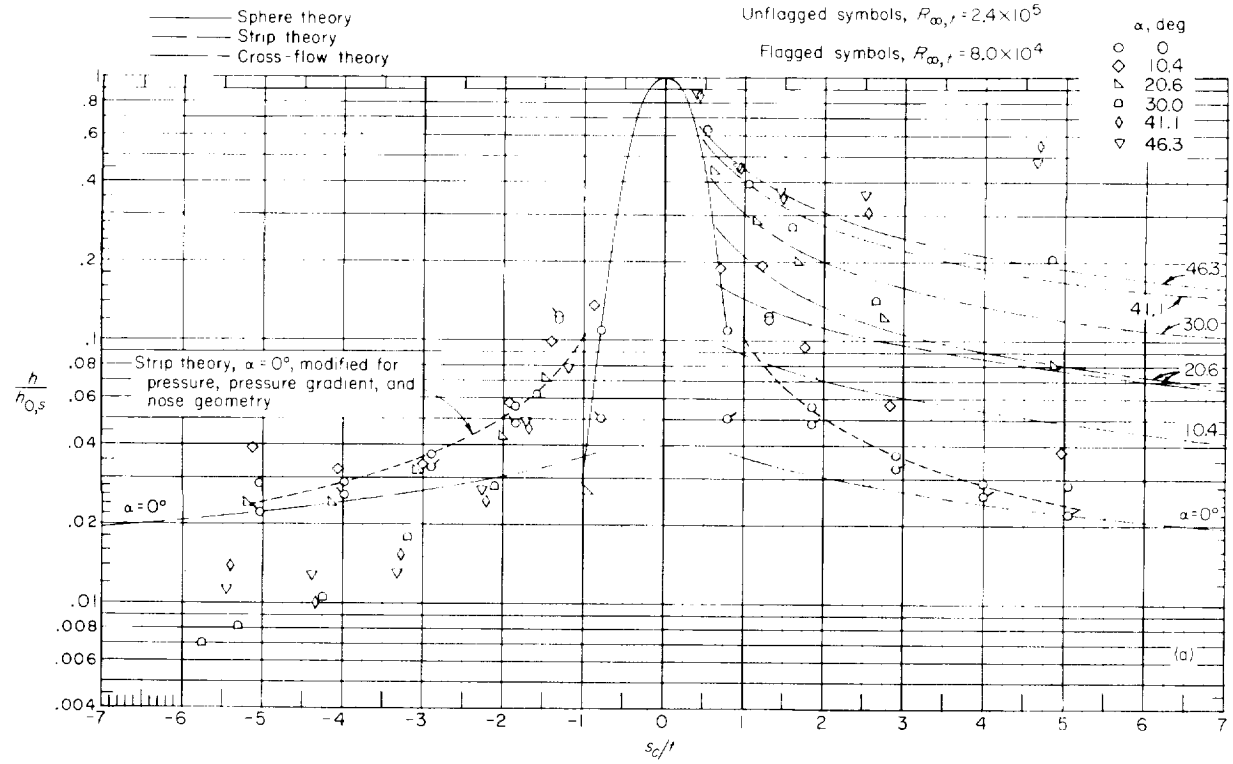

(a) $M_\infty = 6.8$.

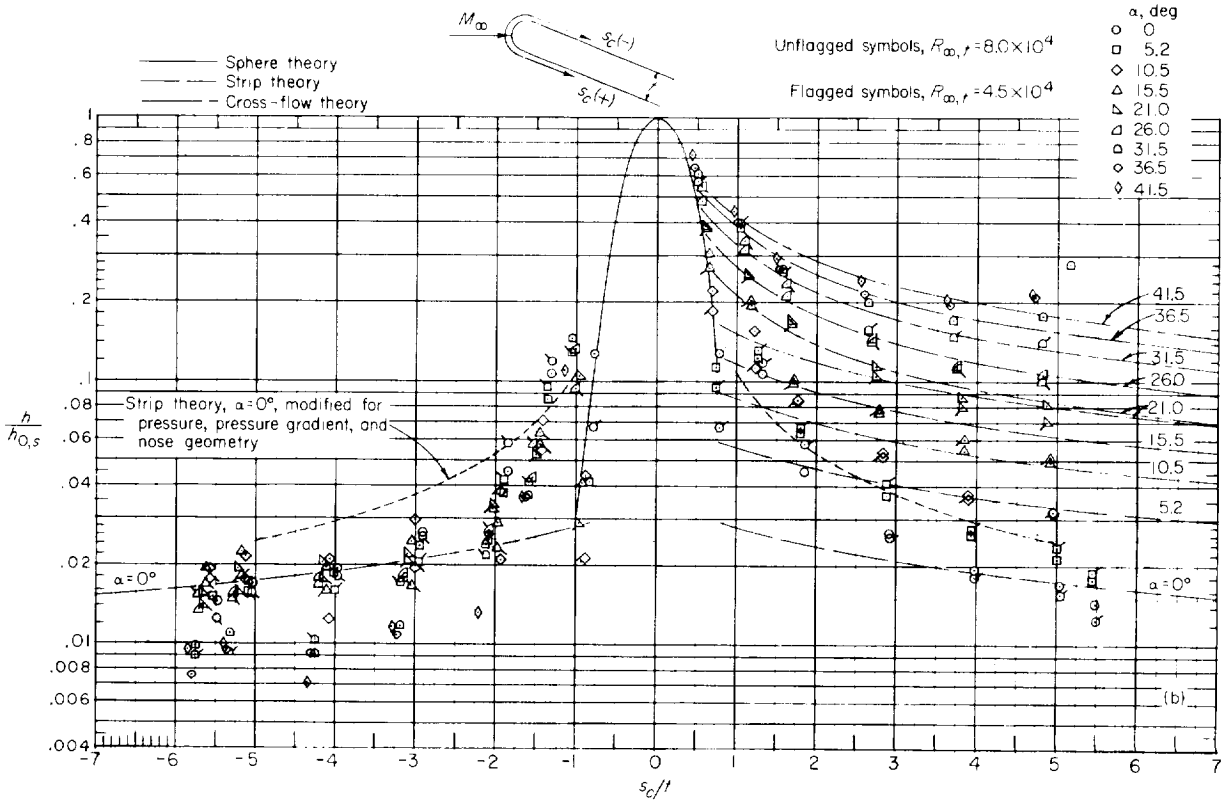

(b) $M_\infty = 9.6$.

Figure 10.- Center-line distribution of heat-transfer coefficient on spherical-nose slab delta wing. $\Lambda = 70^\circ$.

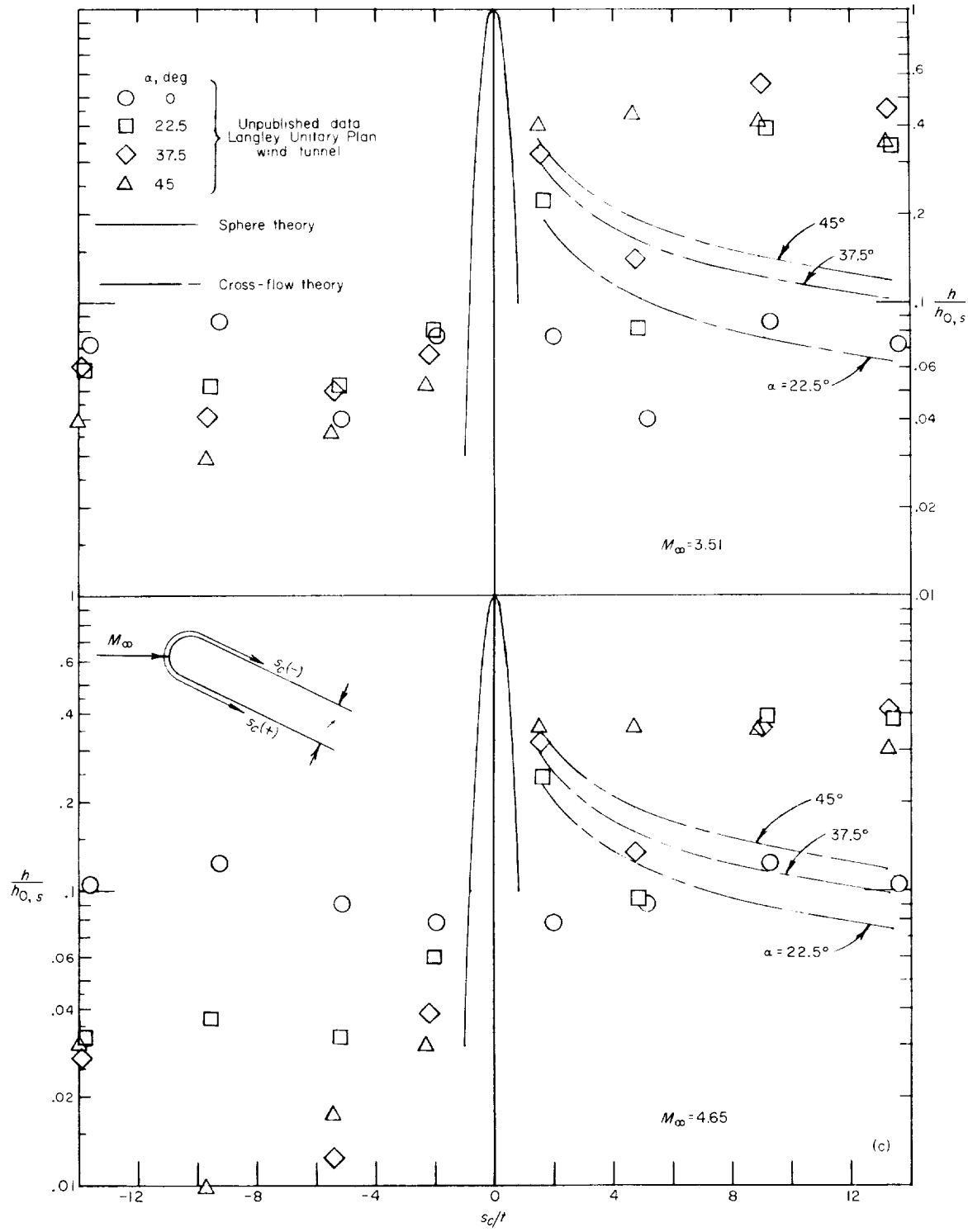

(c) M_∞ = 3.51 and 4.65; $R_{\infty,t}$ = 3.4 × 10^5.

Figure 10.- Concluded.

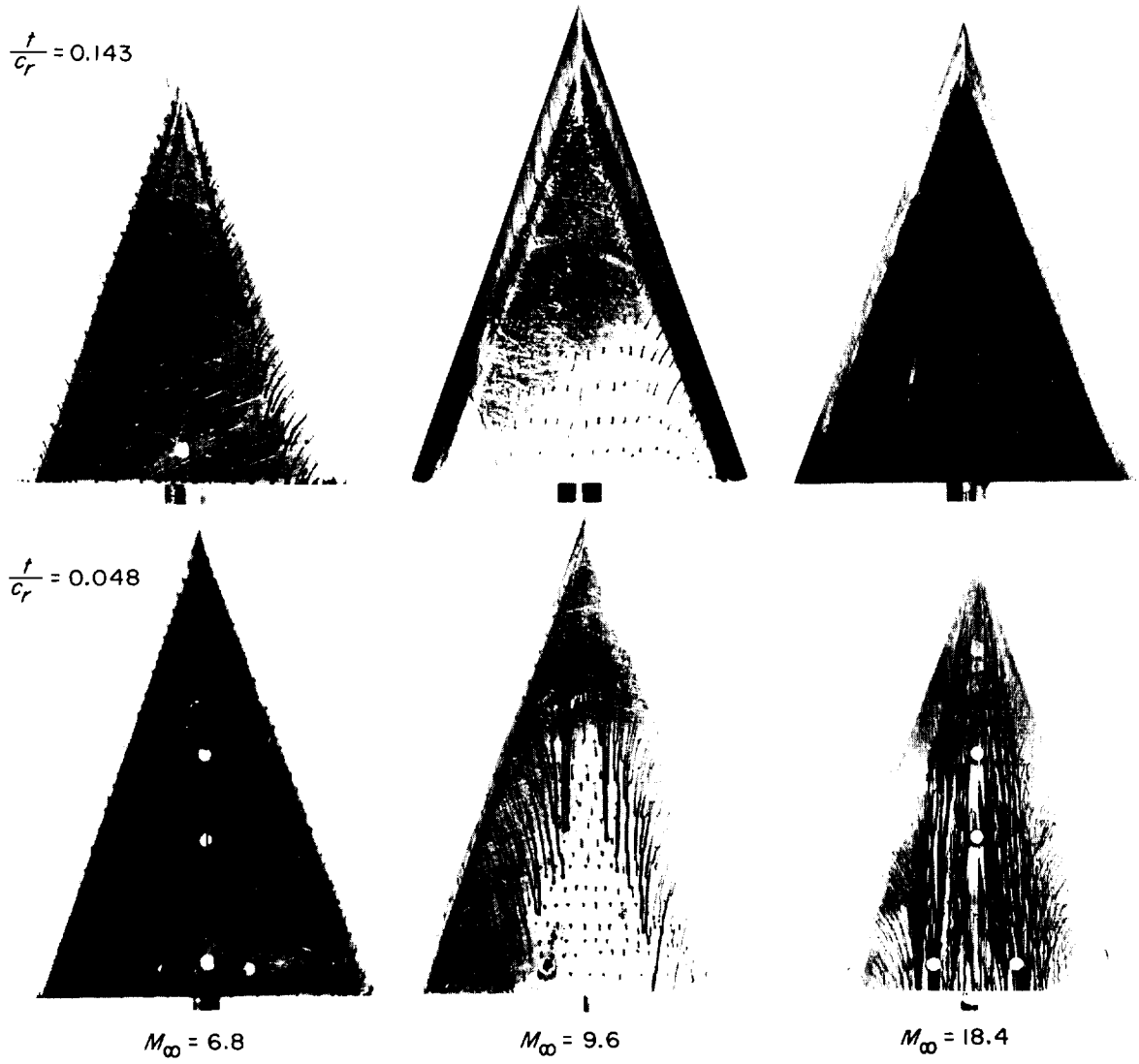

(a) Sharp prow. L-62-2142

Figure 11.- Surface flow studies at an angle of attack of 0°.

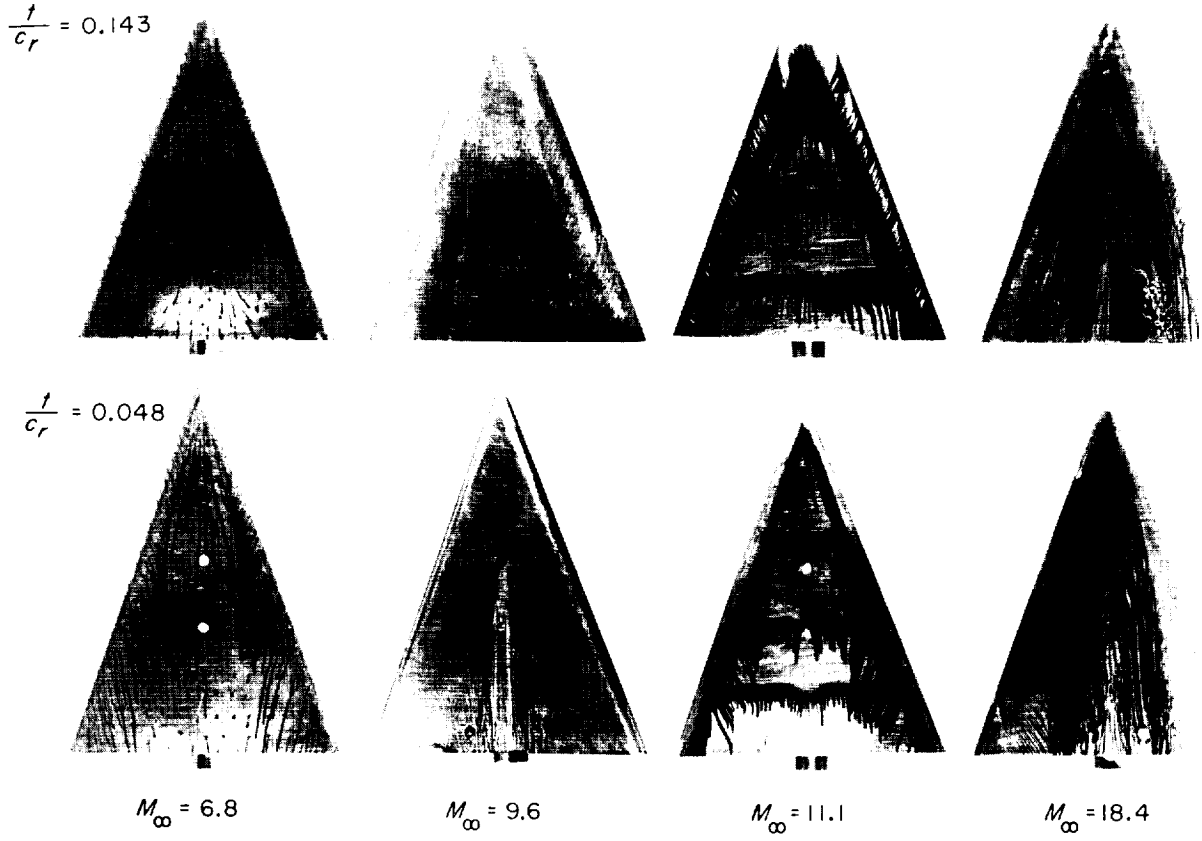

(b) Blunt prow. L-62-2143

Figure 11.- Concluded.

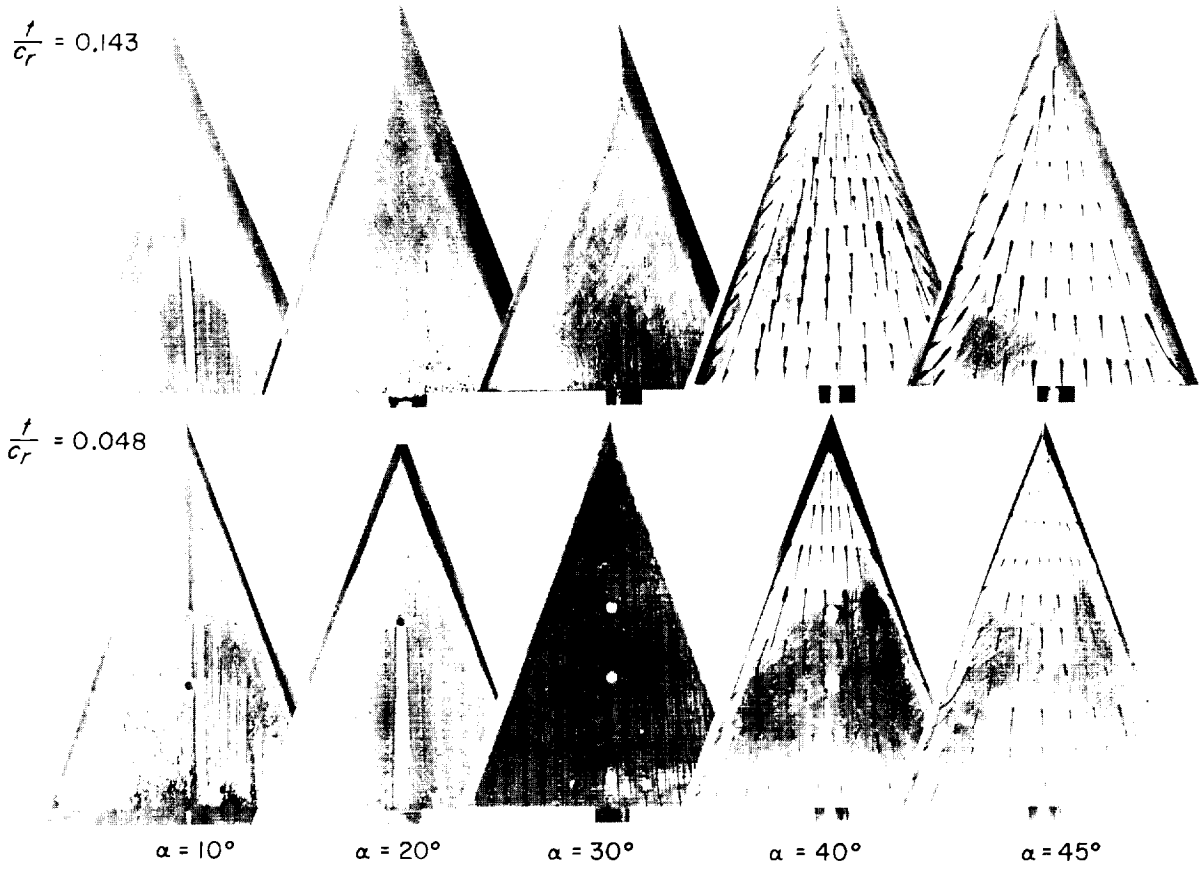

(a) Sharp prow; windward side. L-62-2144

Figure 12.- Surface flow studies at $M_\infty = 6.9$.

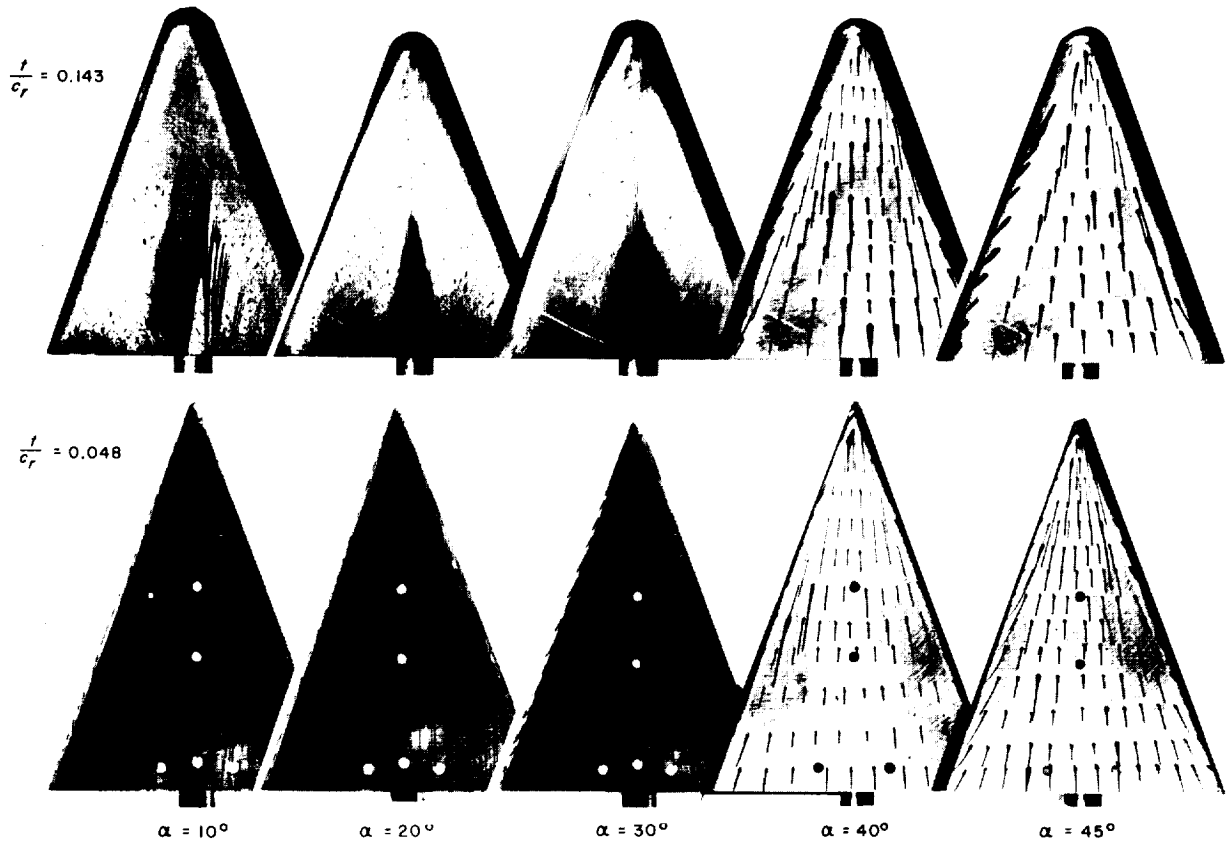

(b) Blunt prow; windward side. L-62-2145

Figure 12.- Continued.

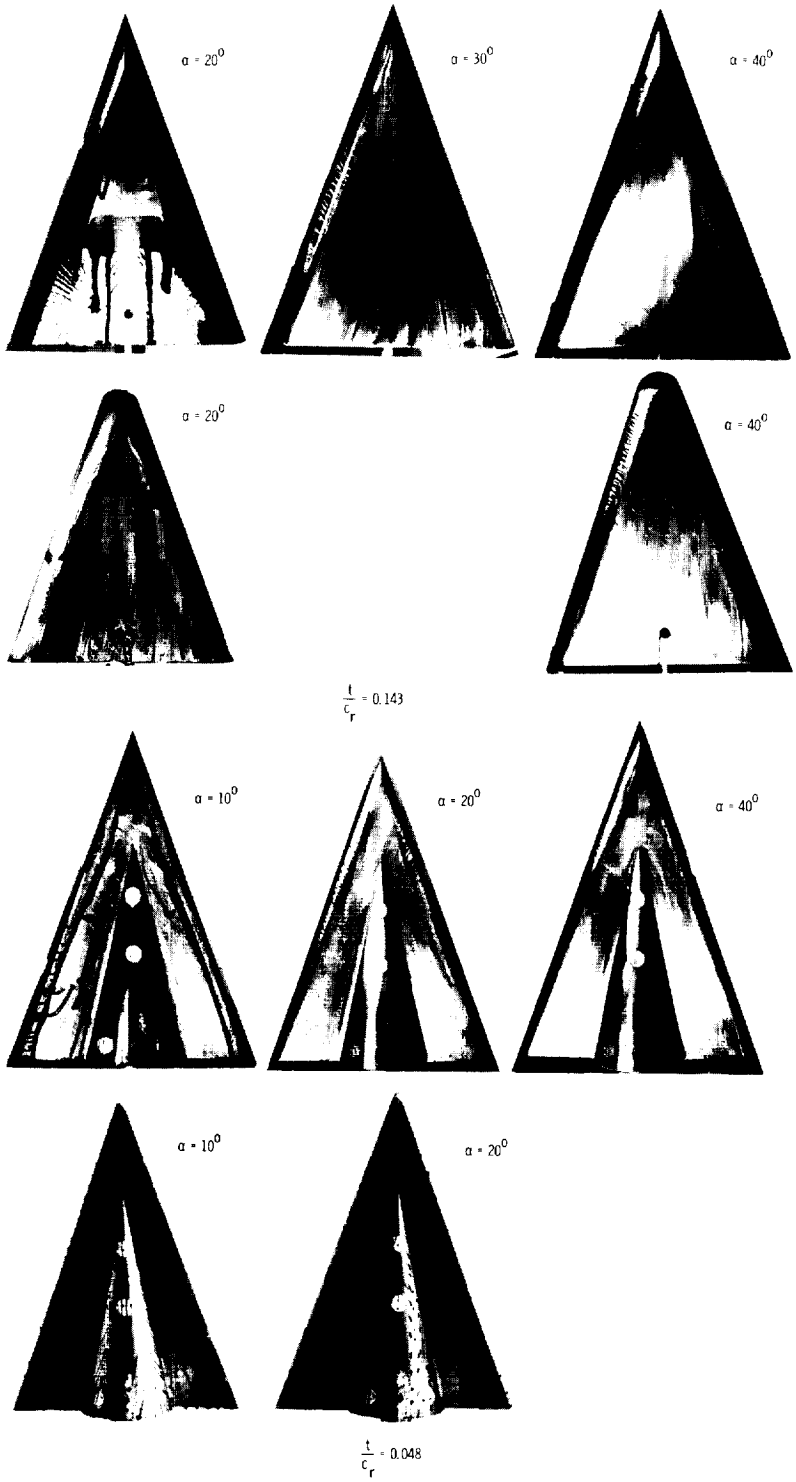

(c) Leeward side. L-62-2146

Figure 12.- Concluded.

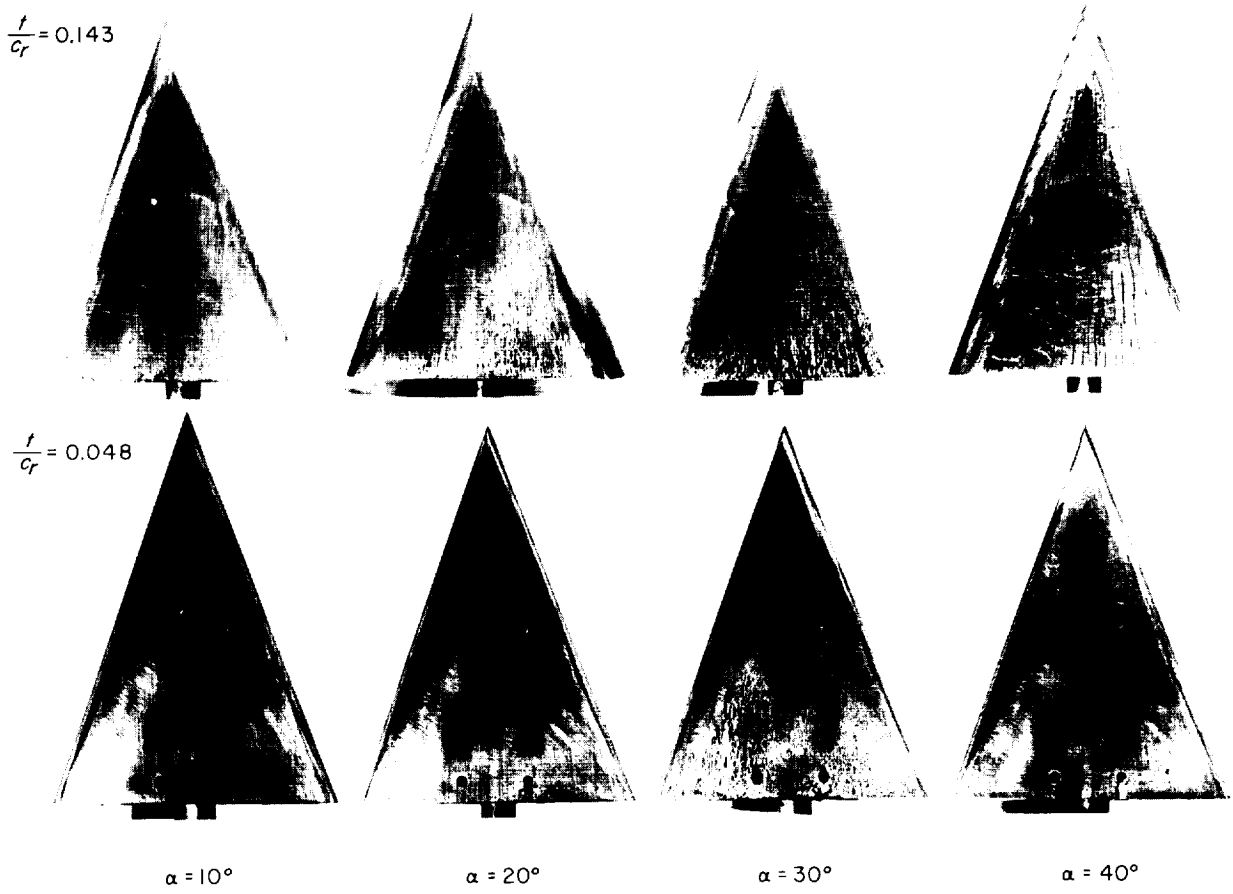

(a) Sharp prow; windward side. L-62-2147

Figure 13.- Surface flow studies at M_∞ = 9.6.

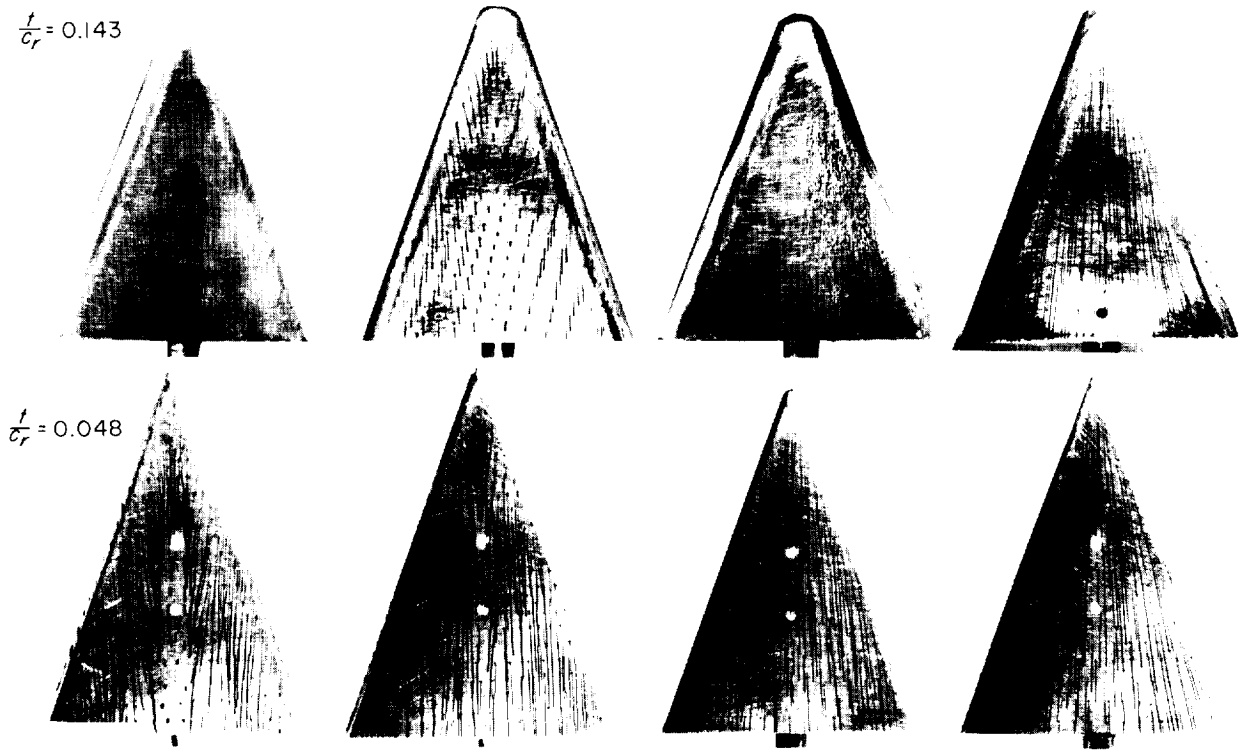

(b) Blunt prow; windward side. L-62-2148

Figure 13.- Continued.

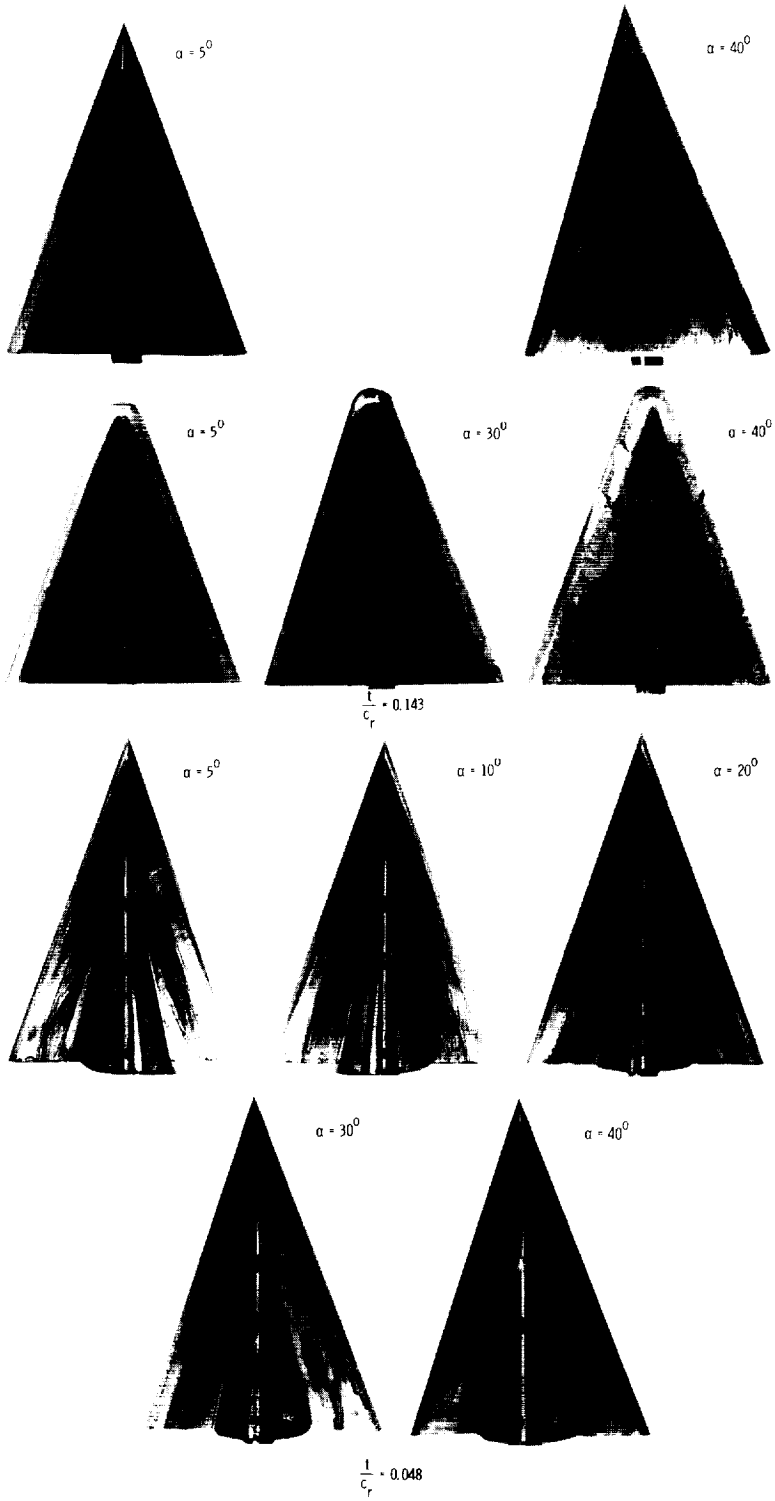

(c) Leeward side. L-62-2149

Figure 13.- Continued.

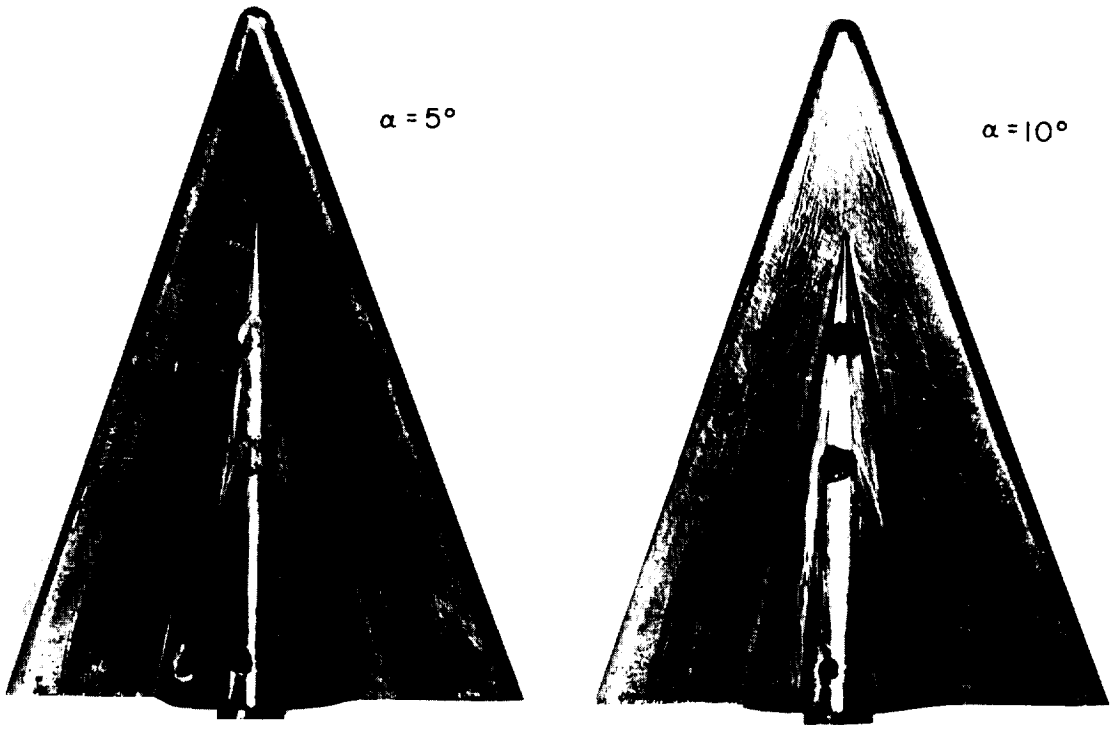

(d) Details of oil flow on leeward side at low angle of attack. L-62-2150

Figure 13.- Concluded.

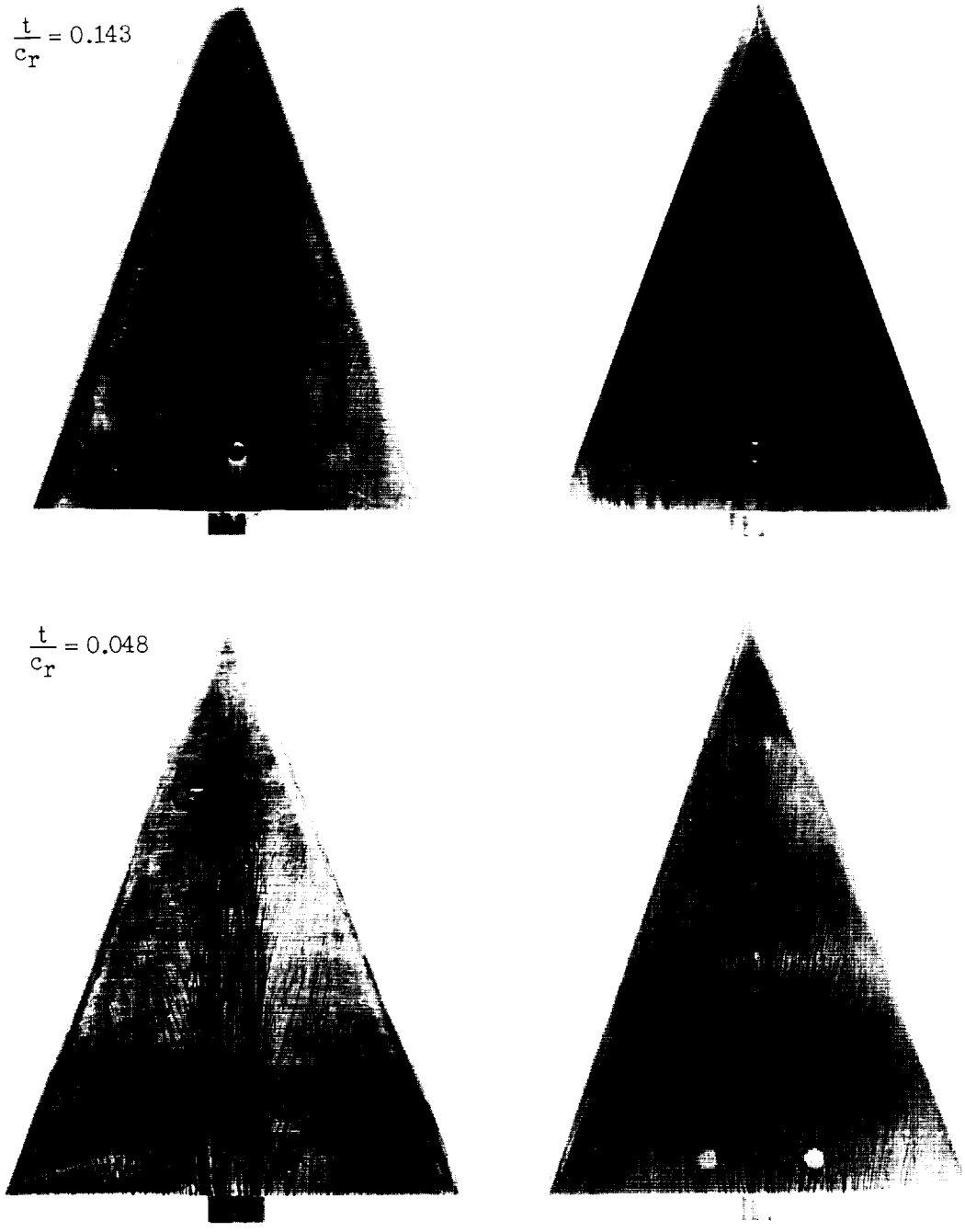

(a) $\alpha = 10^{\circ}$; windward side. L-62-7000

Figure 14.- Surface flow studies at $M_{\infty} = 18.4$.

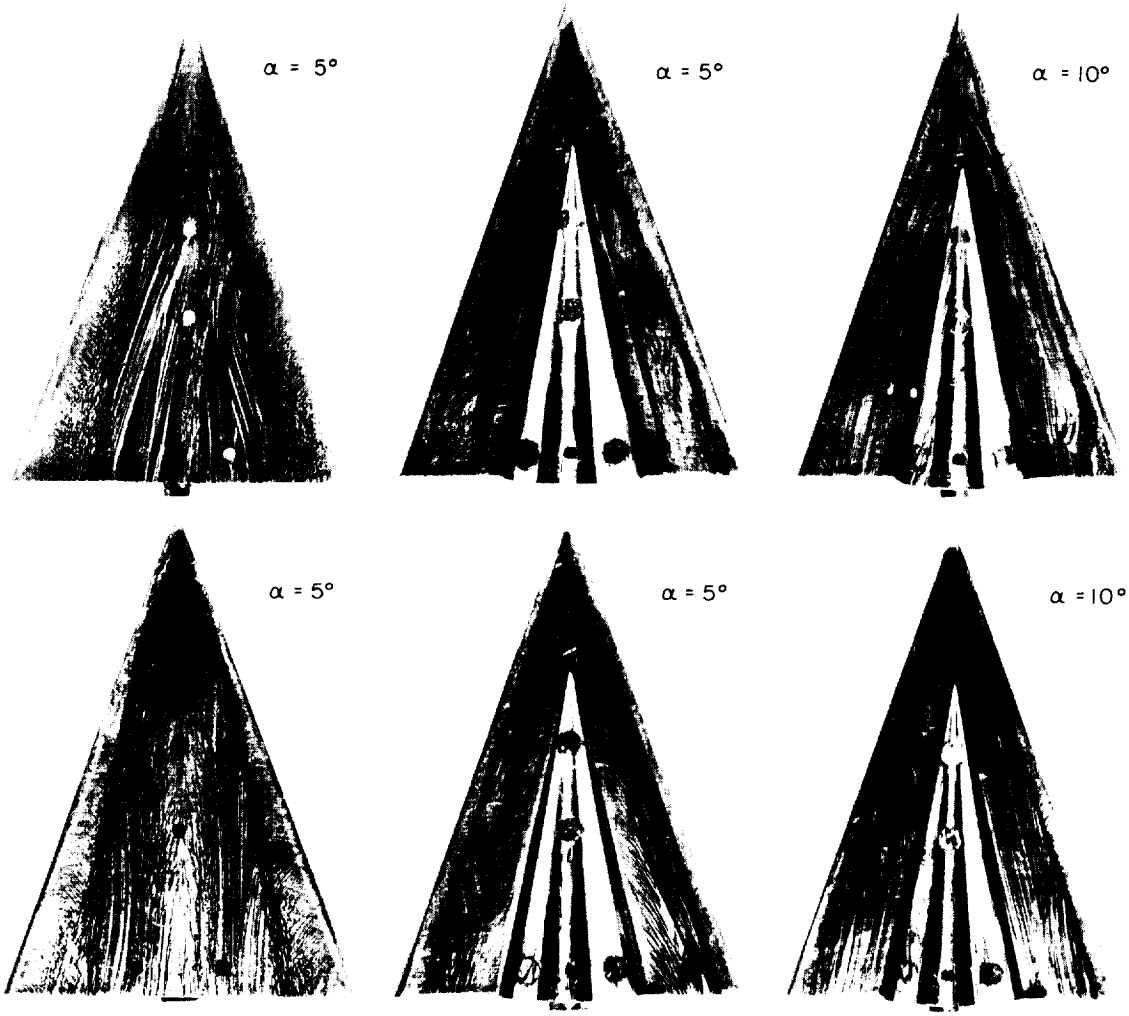

$\frac{t}{c_r} = 0.048$

(b) Leeward side.

L-62-7001

Figure 14.- Concluded.

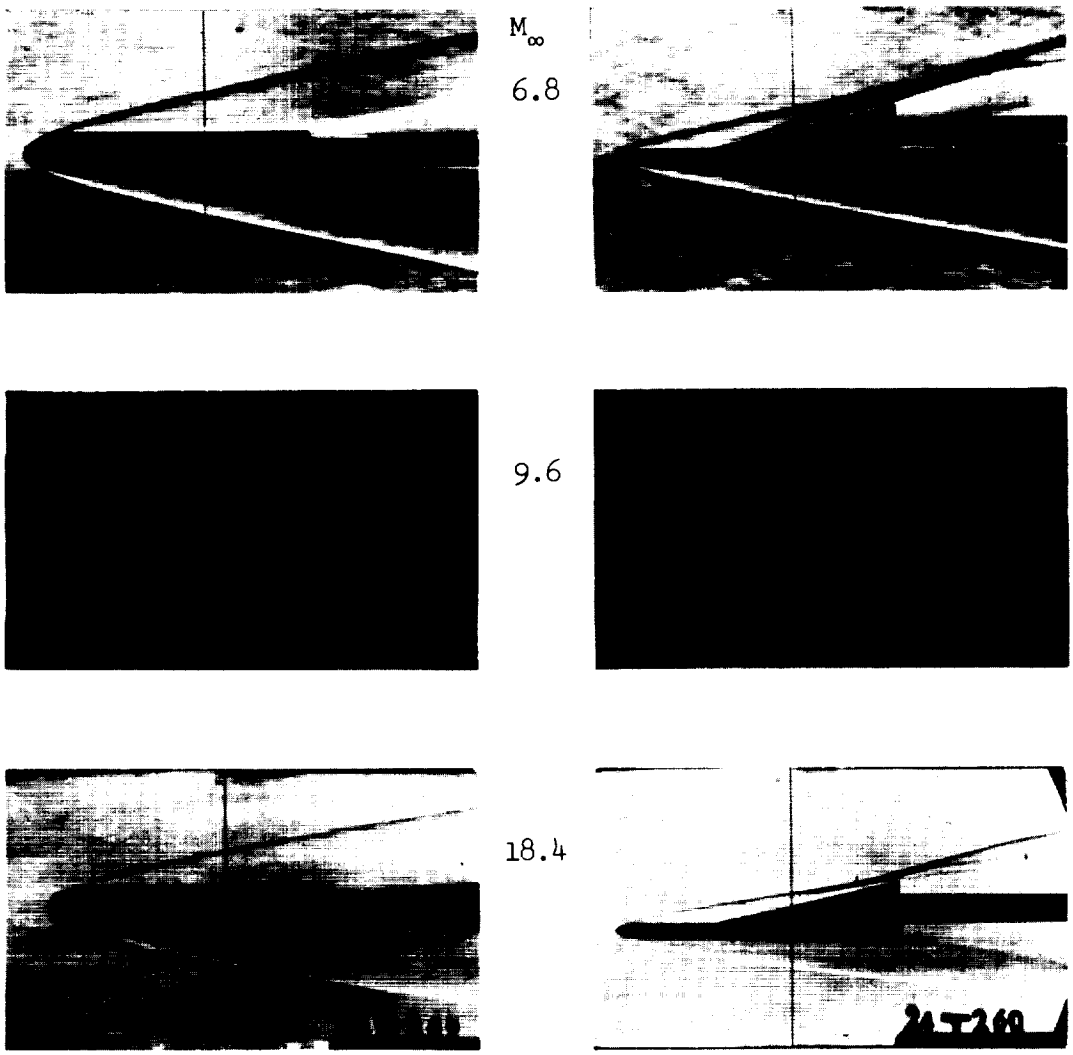

(a) Sharp prow. L-62-7002

Figure 15.- Side-view schlieren photographs. $\alpha = 0^\circ$.

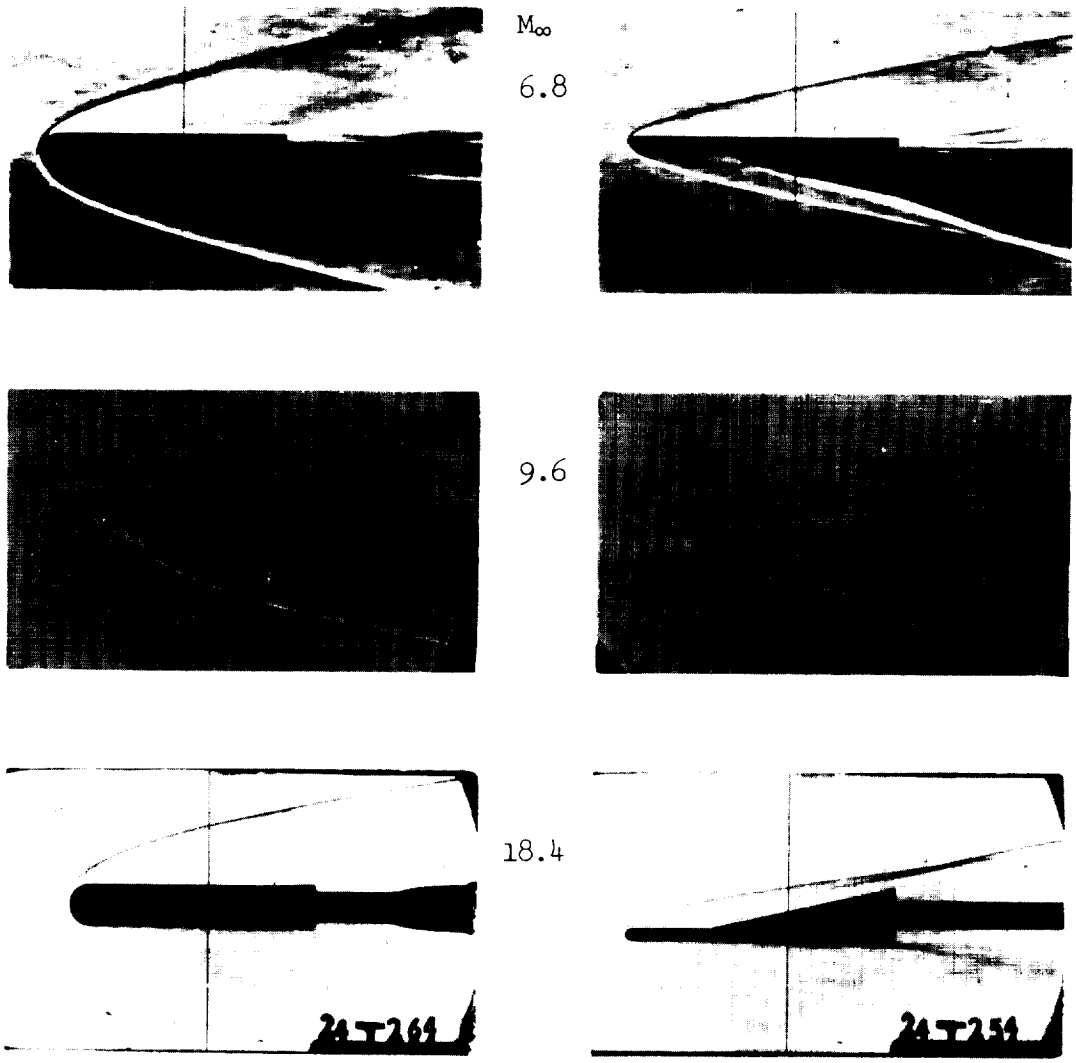

(b) Blunt prow.

L-62-7003

Figure 15.- Concluded.

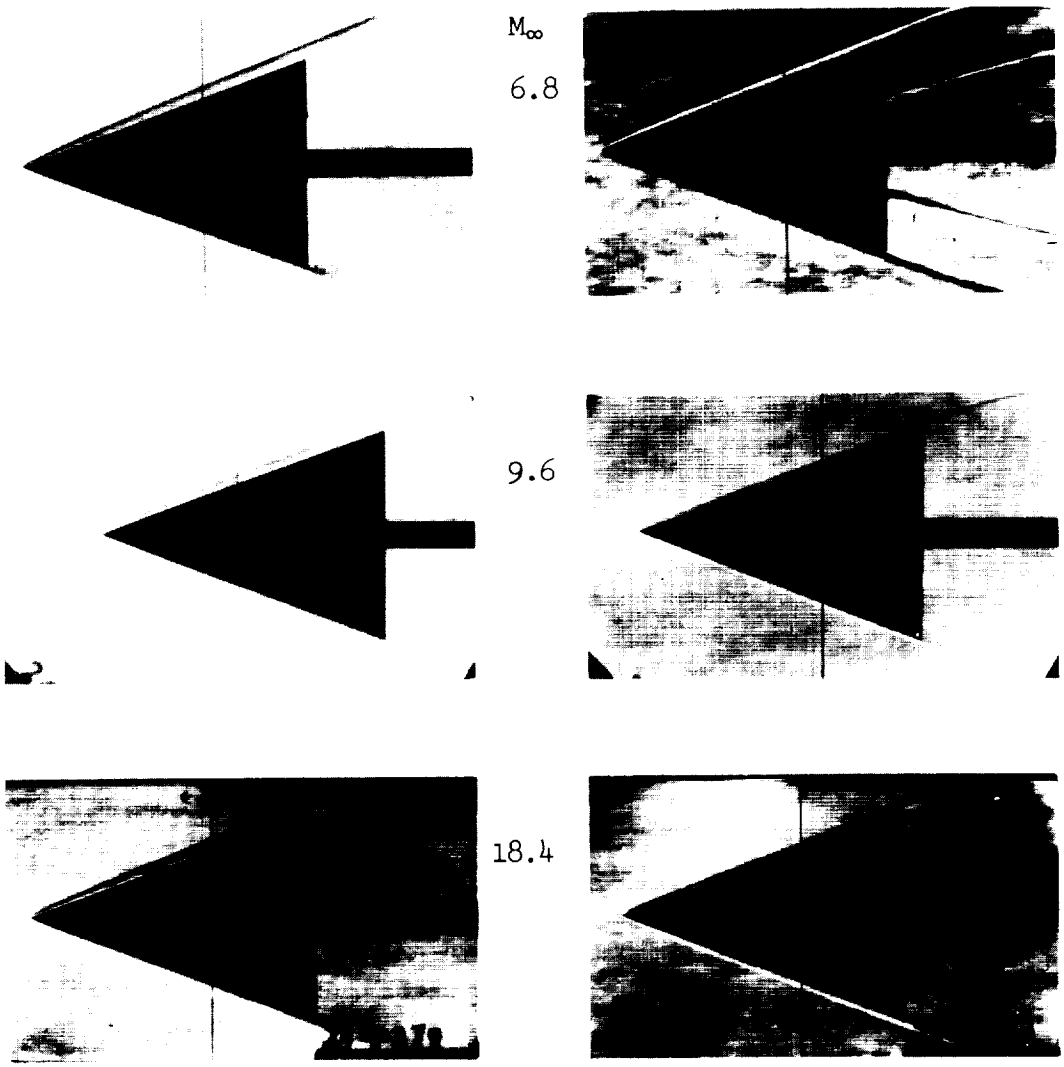

(a) Sharp prow. L-62-7004

Figure 16.- Top view schlieren photographs. $\alpha = 0^\circ$.

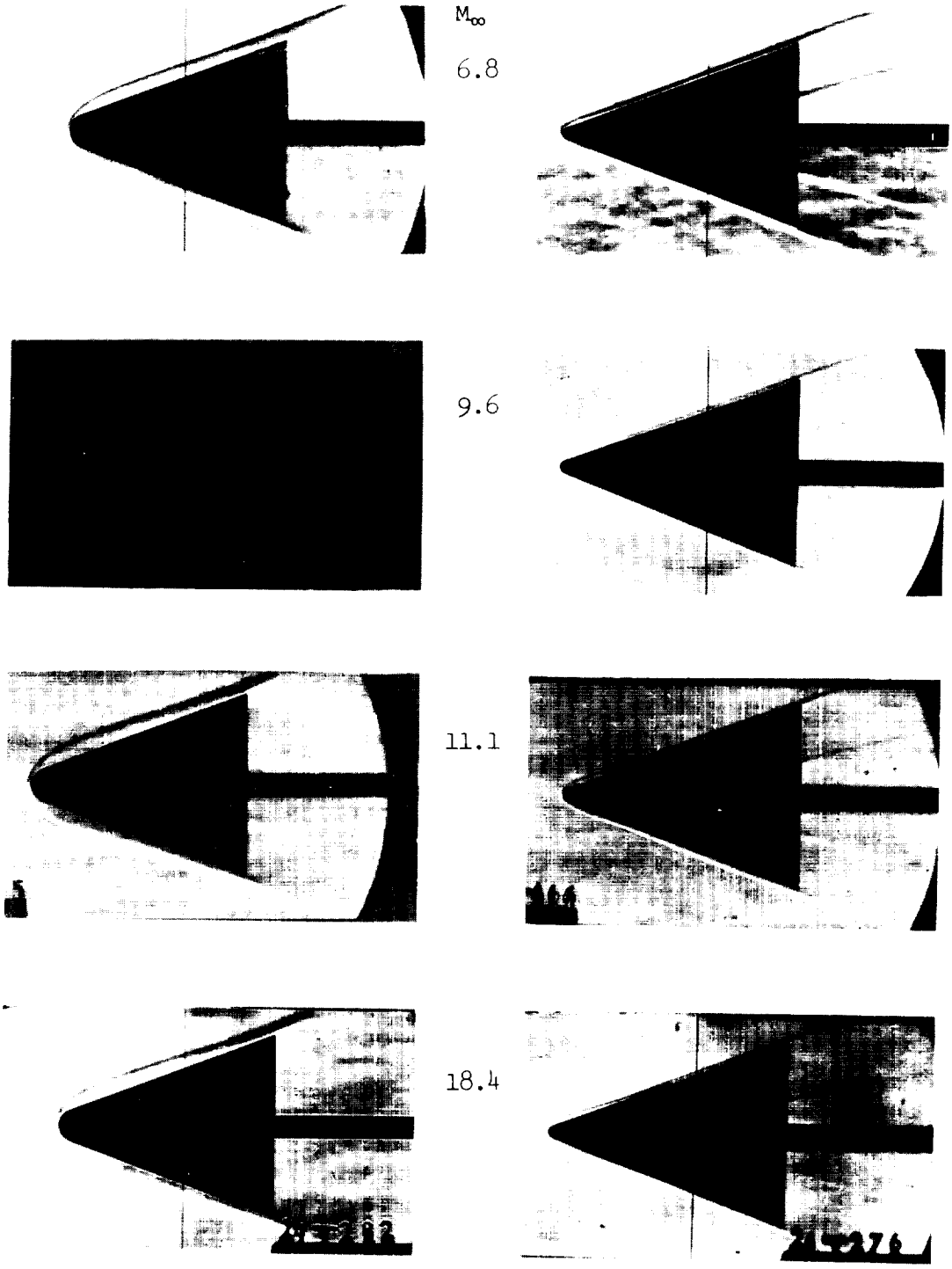

(b) Blunt prow. L-62-7005

Figure 16.- Concluded.

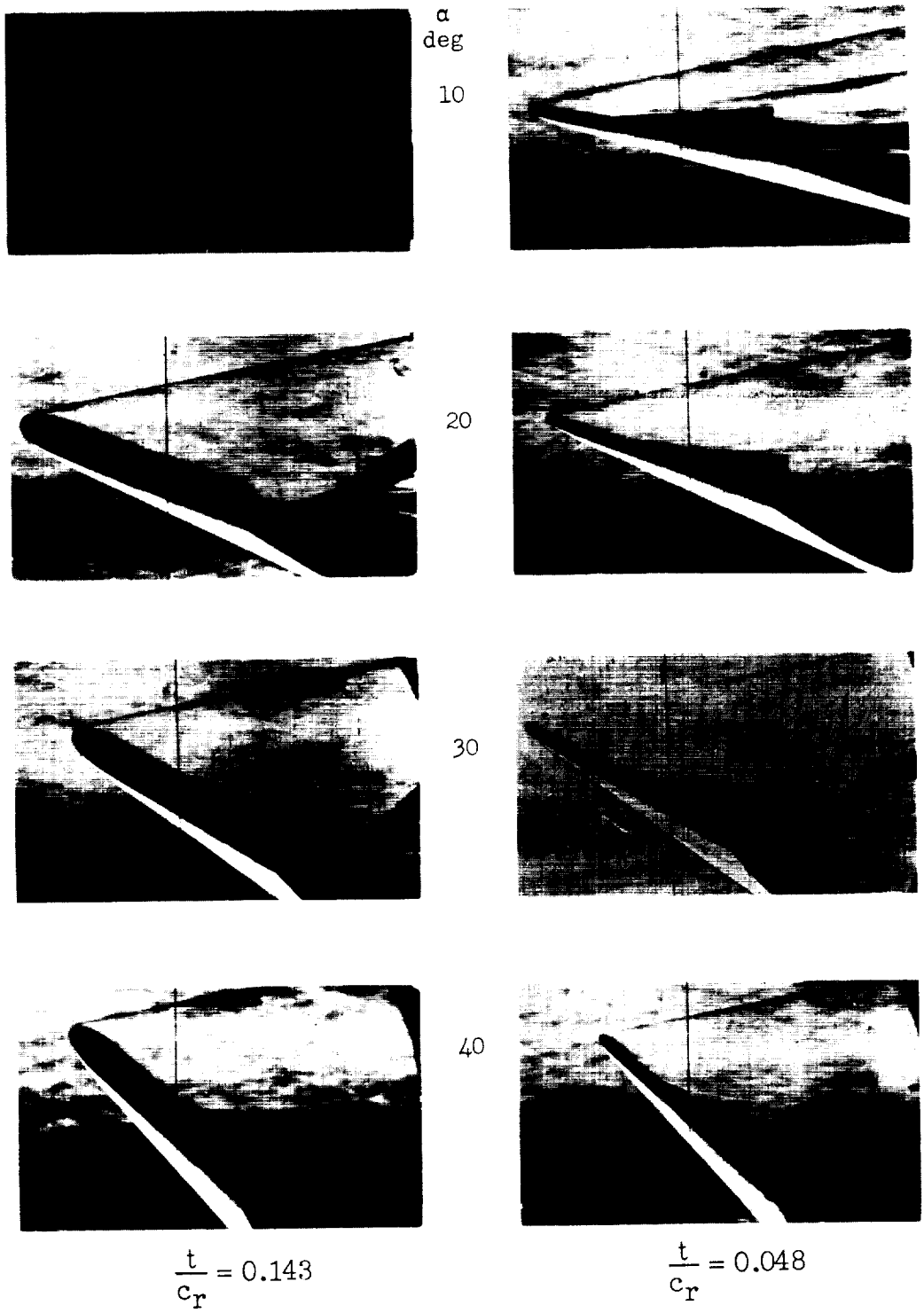

(a) Sharp prow.

L-62-7006

Figure 17.- Side-view schlieren photographs. $M_\infty = 6.8$.

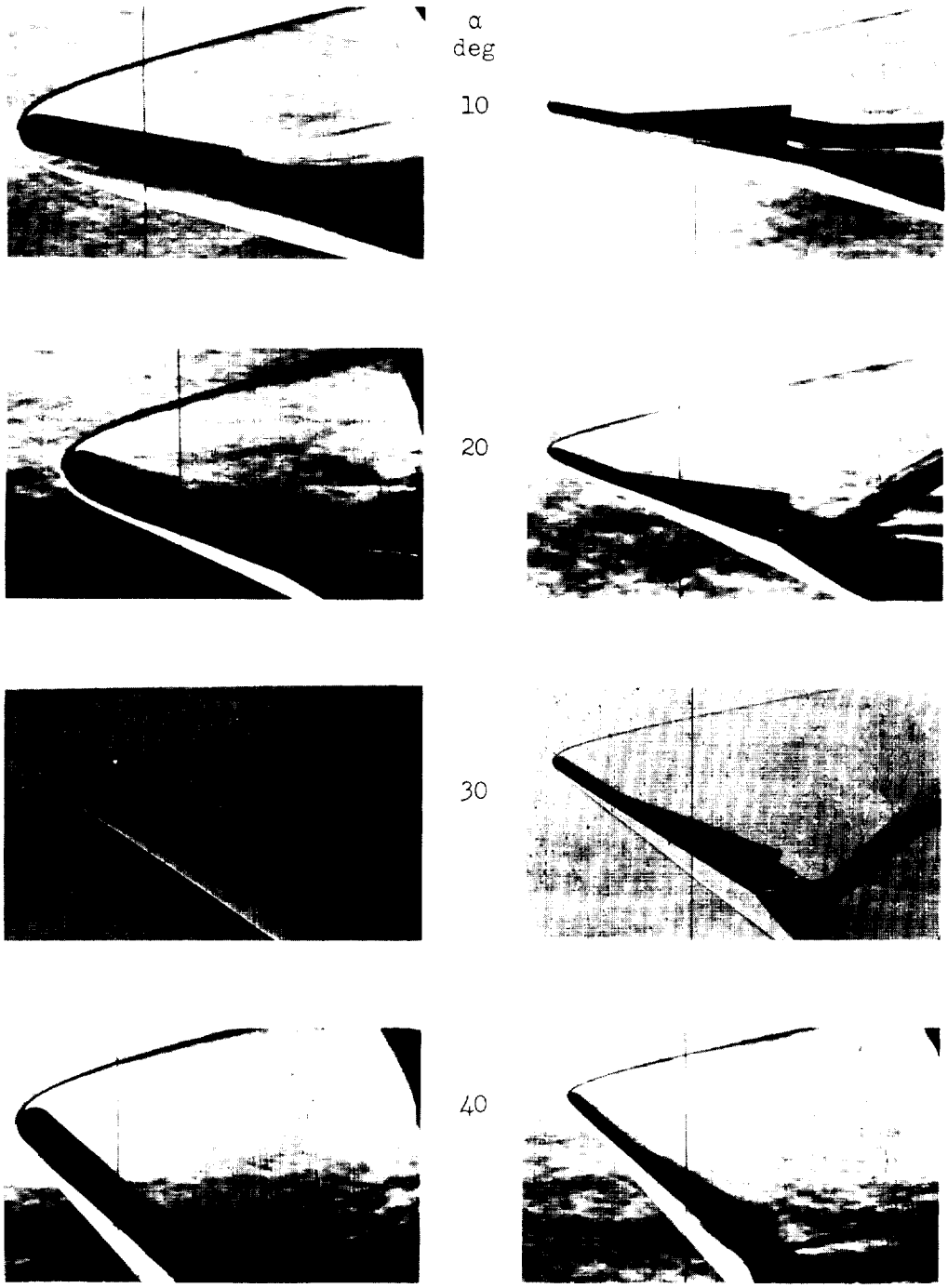

(b) Blunt prow.

L-62-7007

Figure 17.- Concluded.

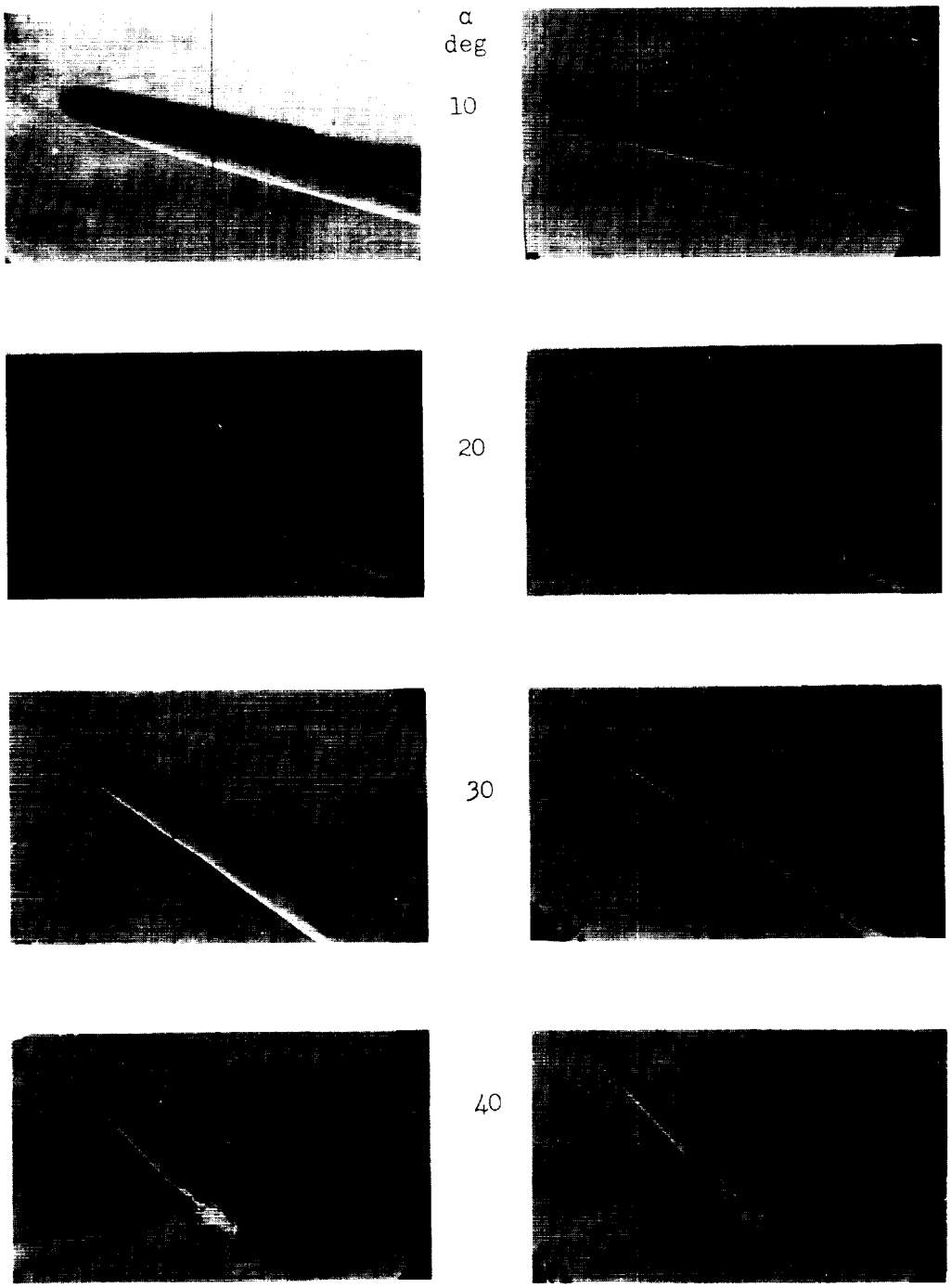

(a) Sharp prow.

L-62-7008

Figure 18.- Side-view schlieren photographs. $M_\infty = 9.6$.

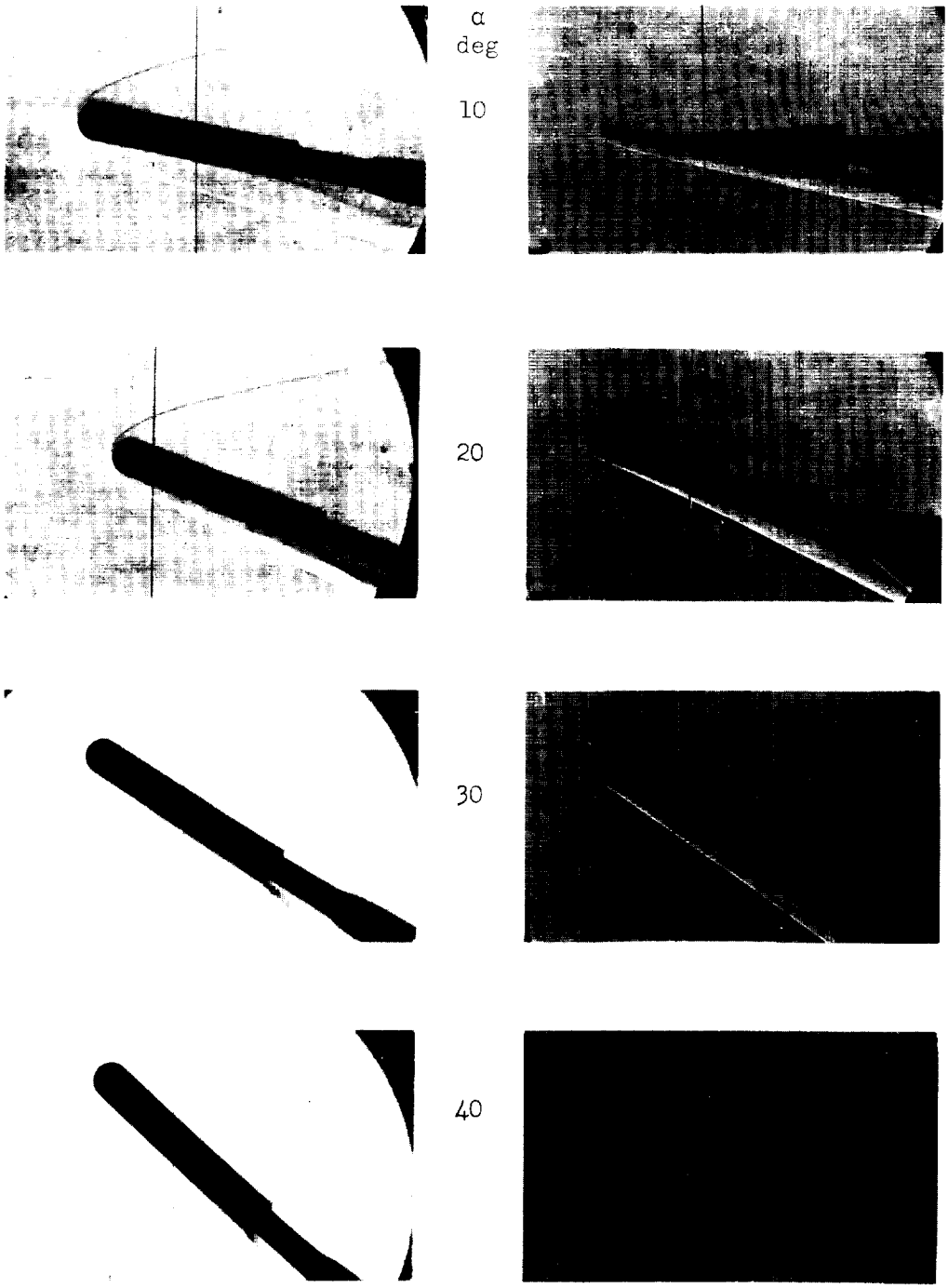

(b) Blunt prow.

L-62-7009

Figure 18.- Concluded.

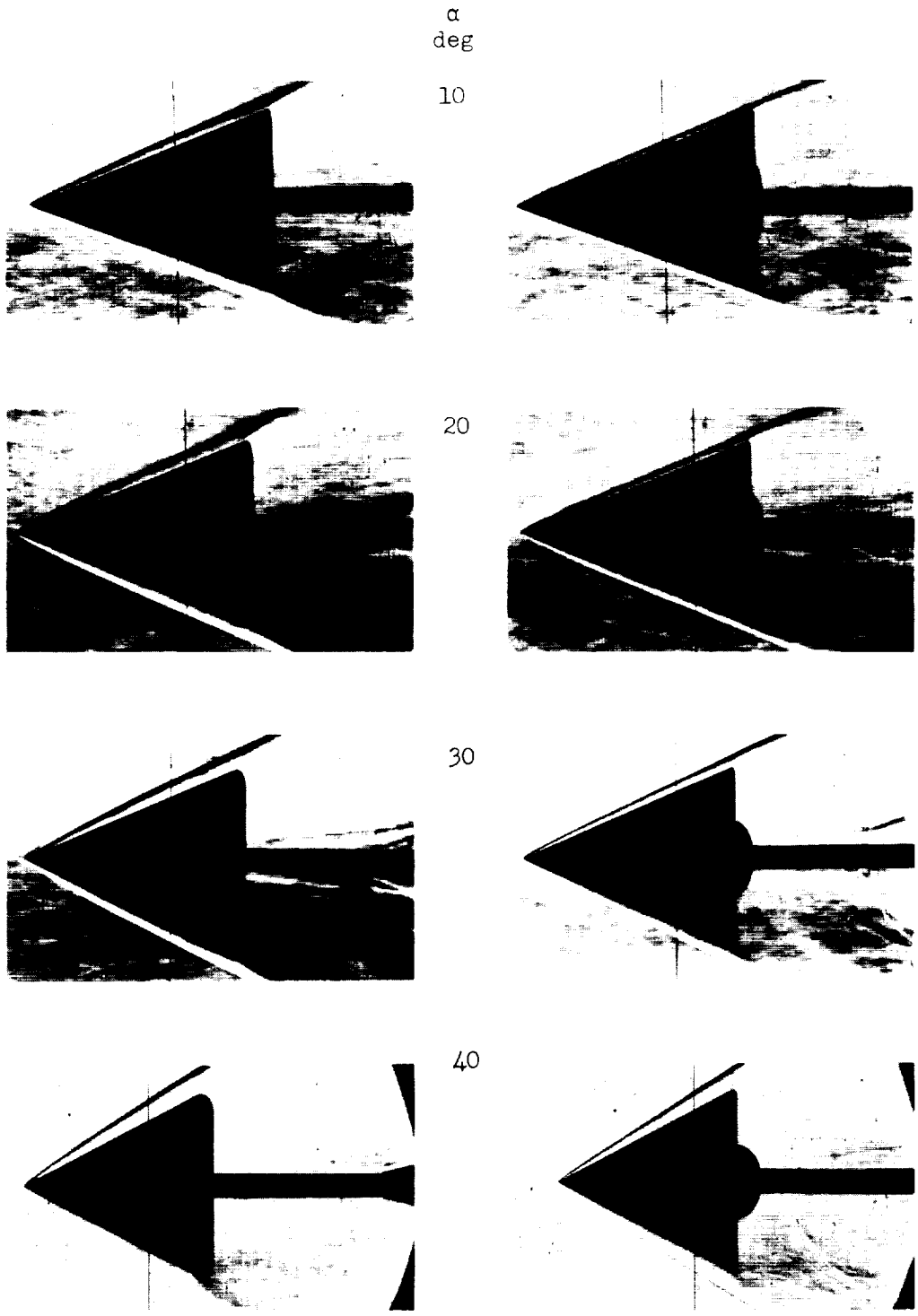

(a) Sharp prow.

L-62-7010

Figure 19.- Top view schlieren photographs. $M_\infty = 6.8$.

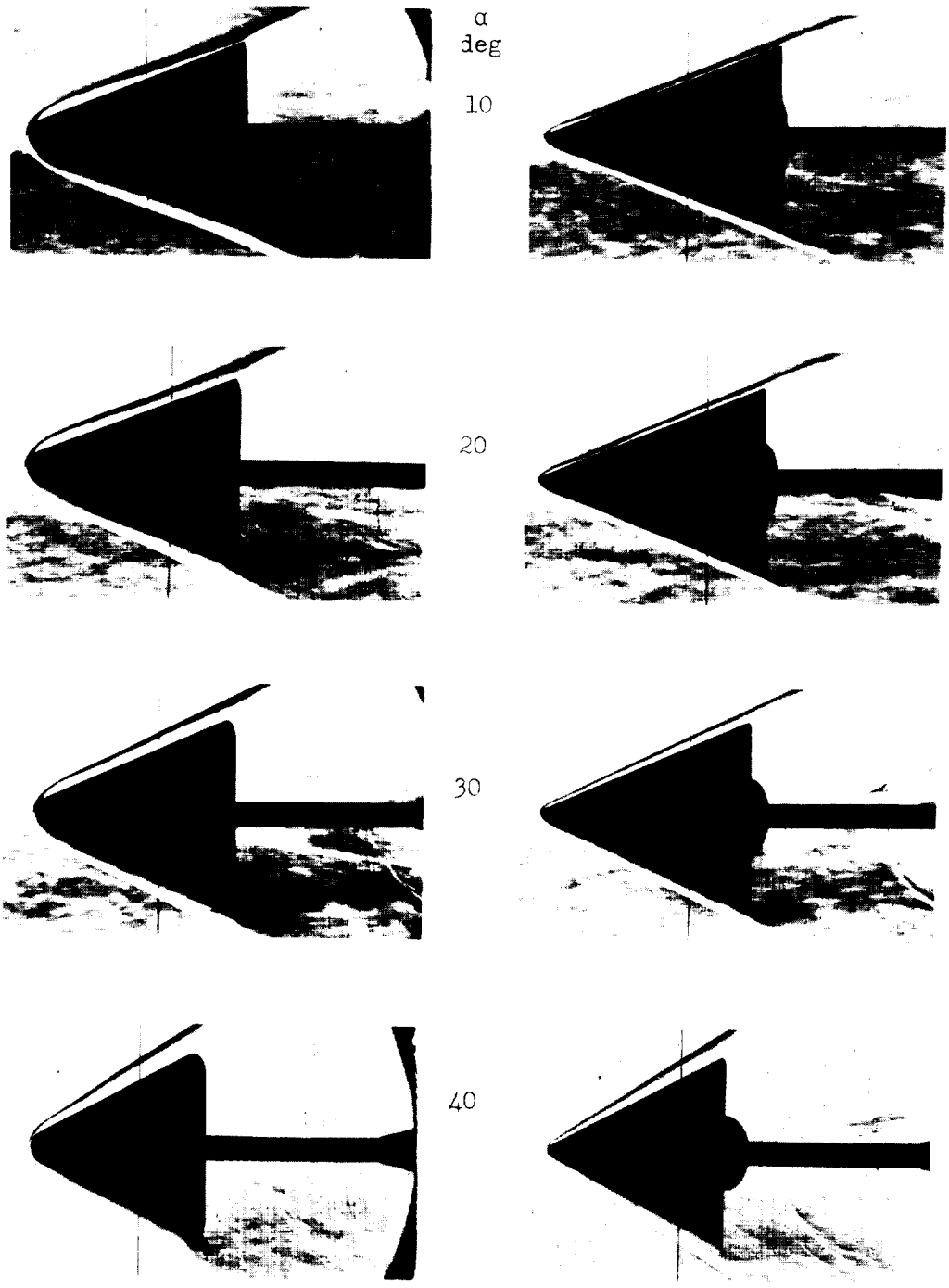

(b) Blunt prow. L-62-7011

Figure 19.- Concluded.

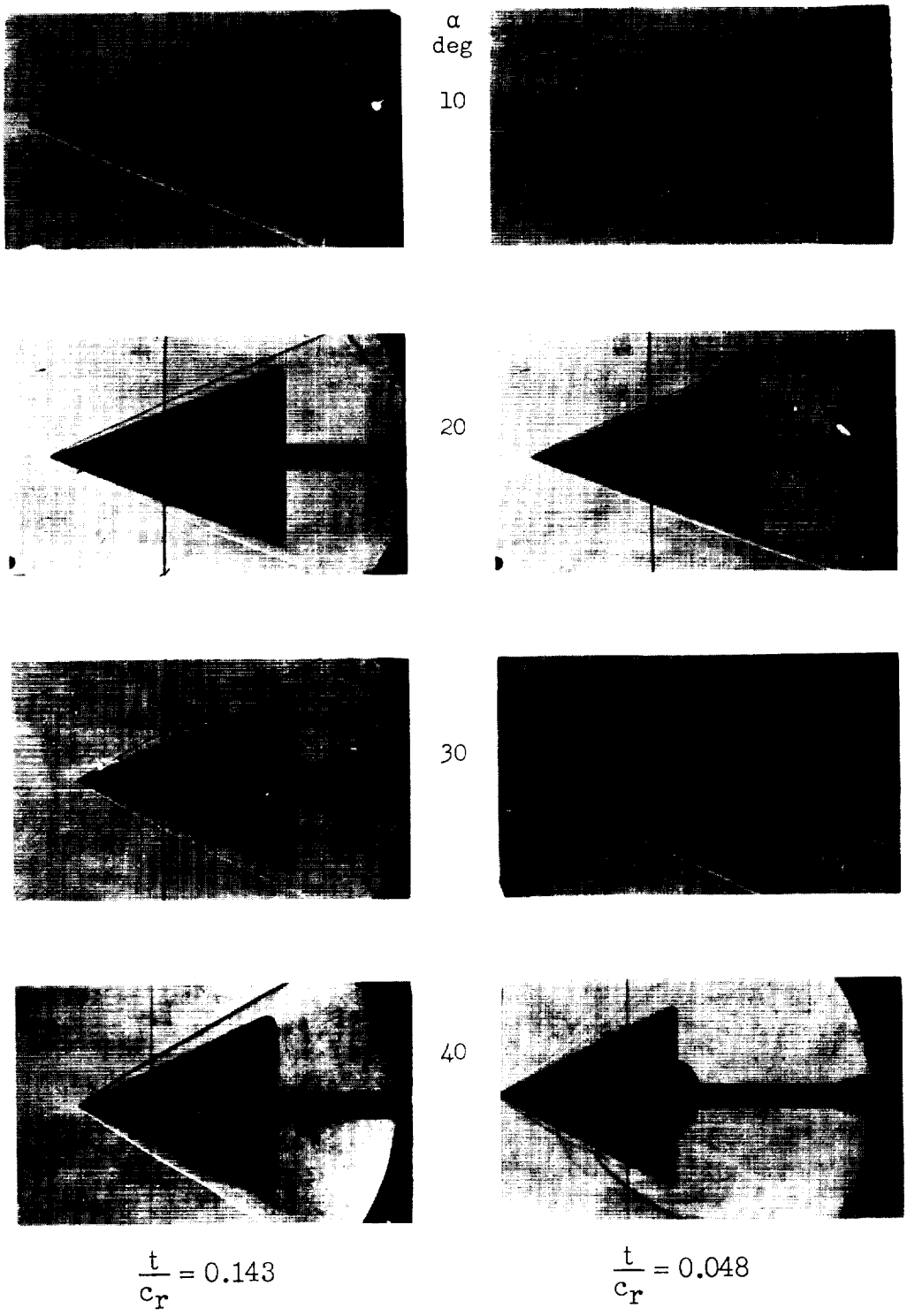

(a) Sharp prow. L-62-7012

Figure 20.- Top view schlieren photographs. $M_\infty = 9.6$.

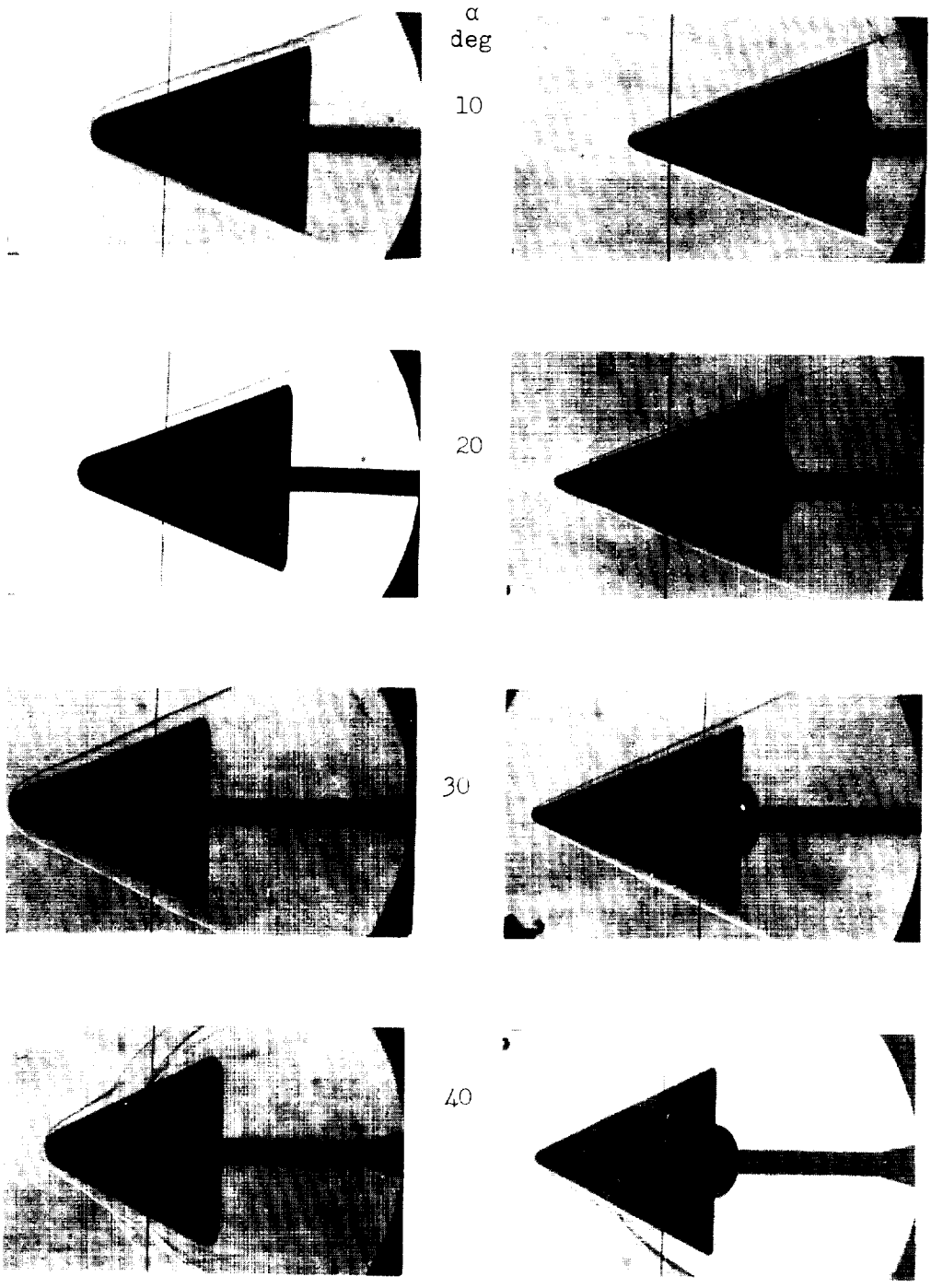

(b) Blunt prow.

L-62-7013

Figure 20.- Concluded.

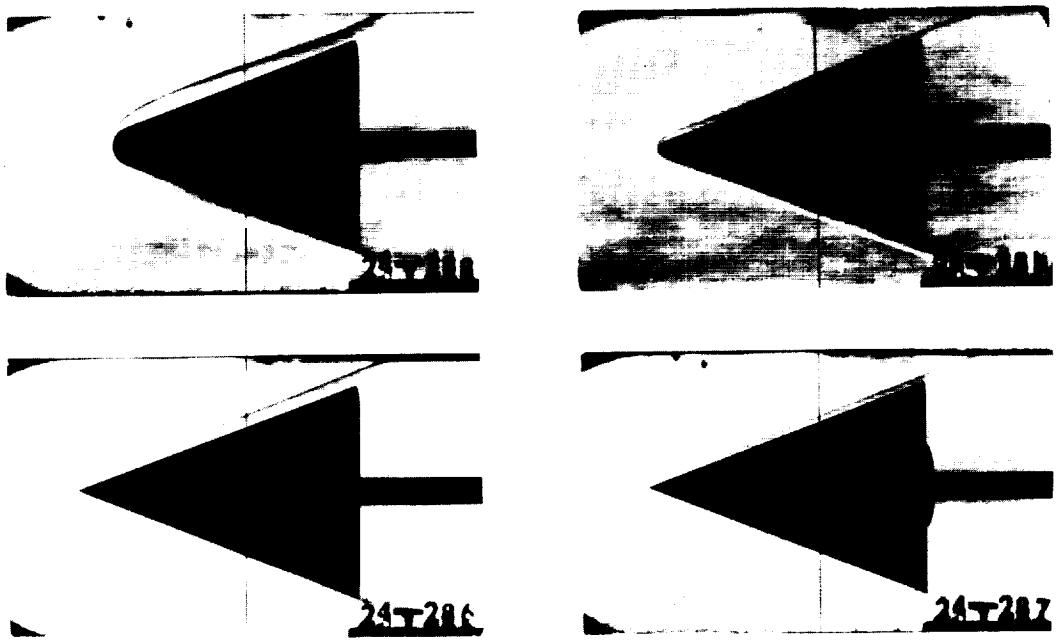

$\frac{t}{c_r} = 0.143$ $\frac{t}{c_r} = 0.048$

(a) Top view.

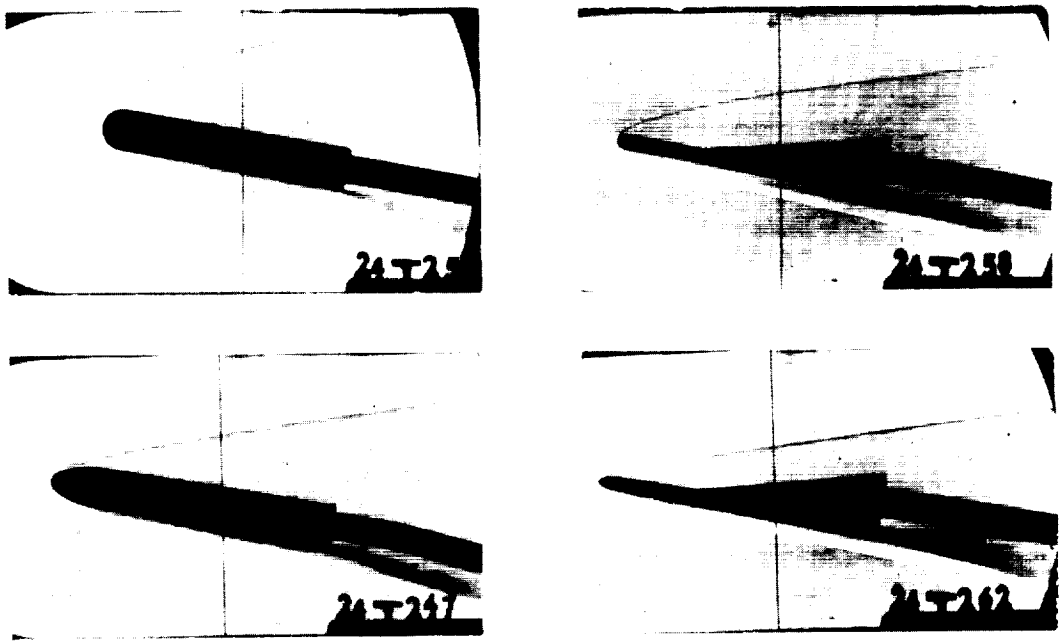

$\frac{t}{c_r} = 0.143$ $\frac{t}{c_r} = 0.048$

(b) Side view. L-62-7014

Figure 21.- Schlieren photographs. $\alpha = 10^{\circ}$; $M_{\infty} = 18.4$.

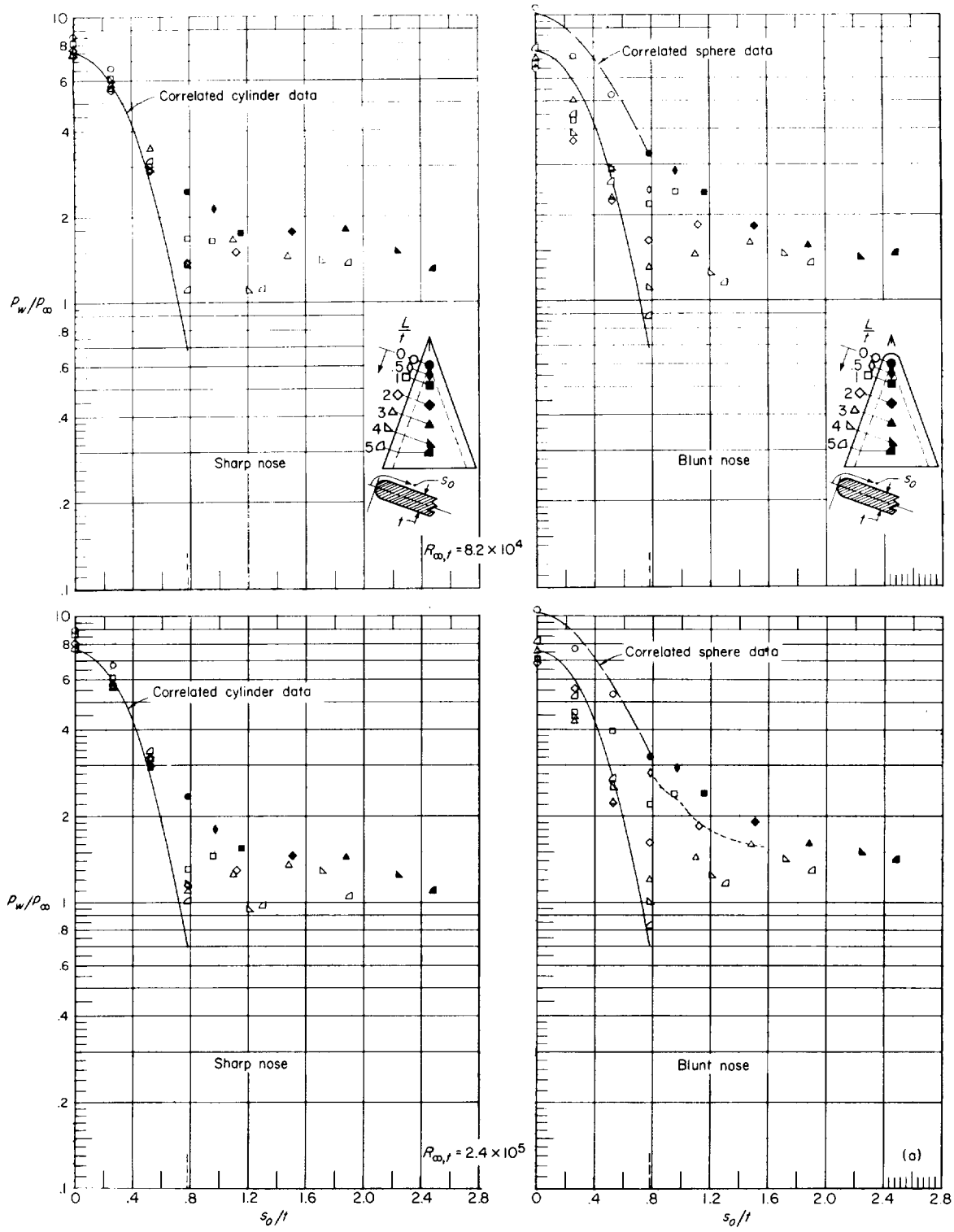

(a) $M_\infty = 6.8$, air.

Figure 22.- Pressure distribution normal to the leading edge on slab delta wing at various stations along the leading edge at an angle of attack of 0°.

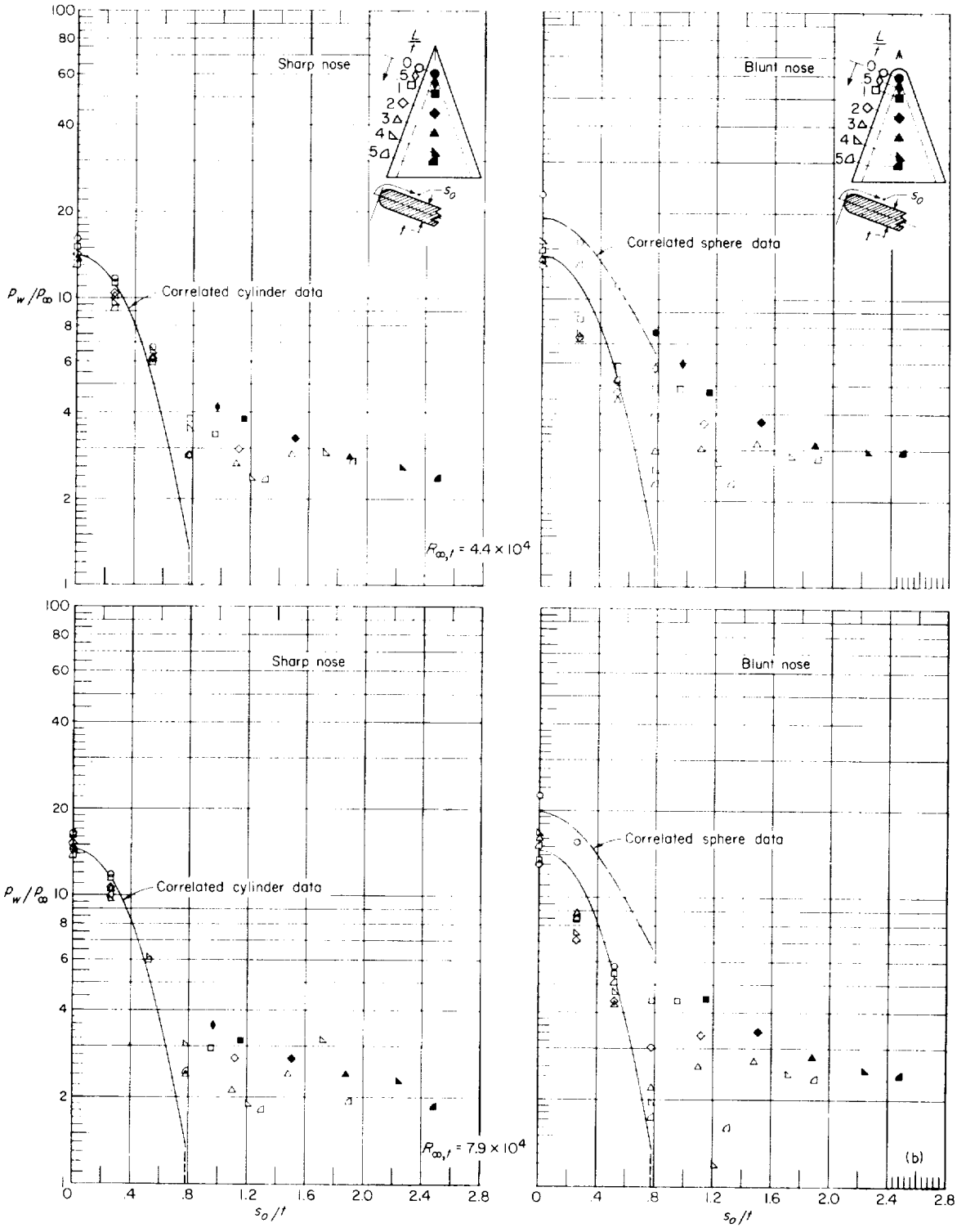

(b) $M_\infty = 9.6$, air.

Figure 22.- Continued.

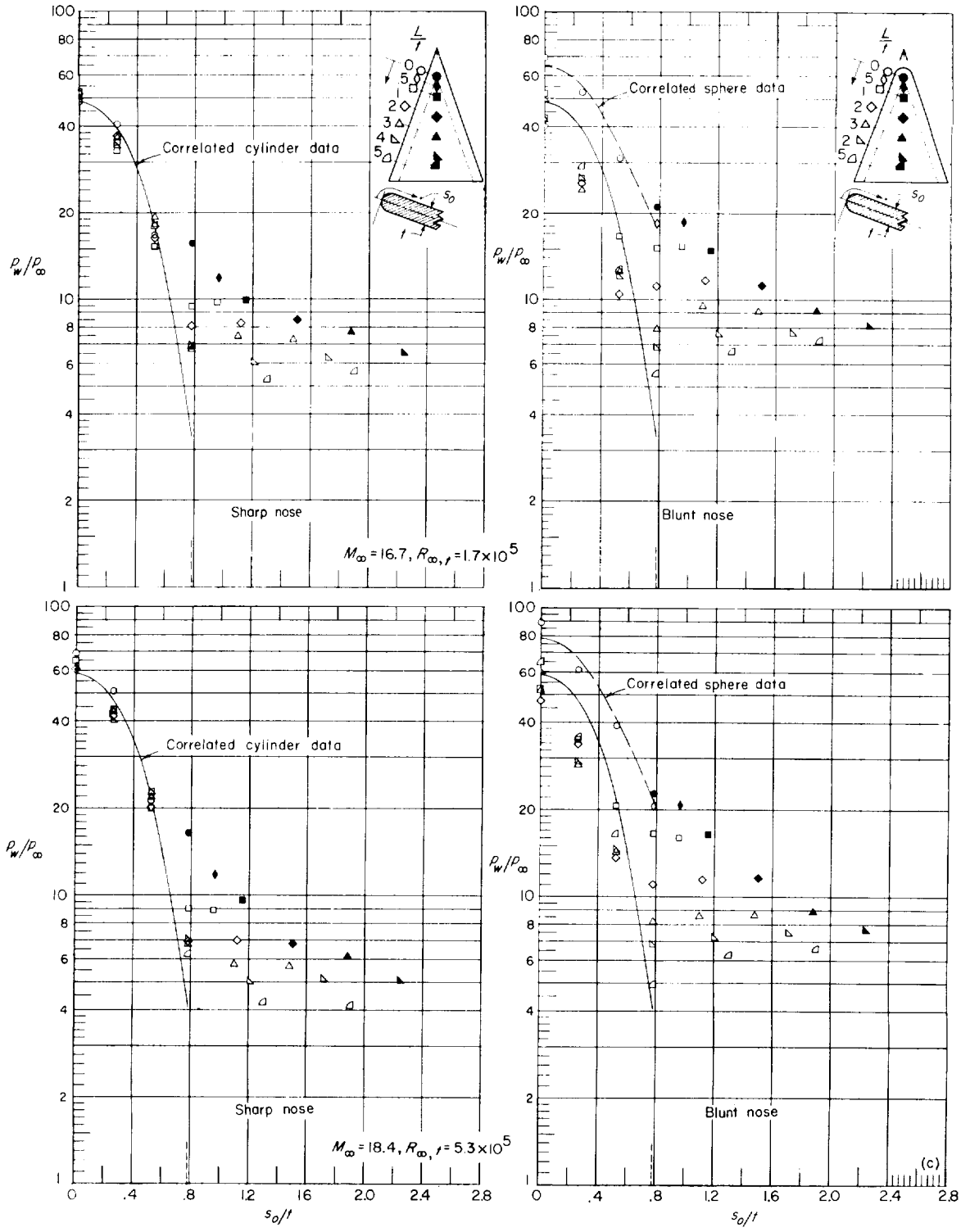

(c) $M_\infty \approx 18$, helium.

Figure 22.- Concluded.

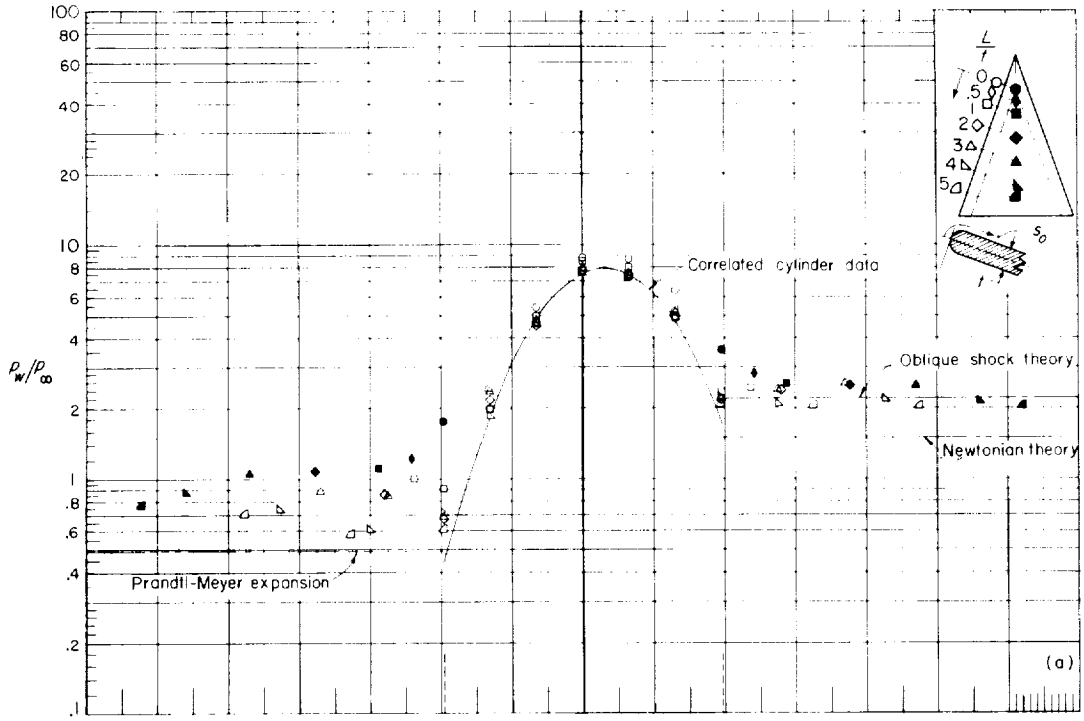

(a) $\alpha = 5^{\circ}$.

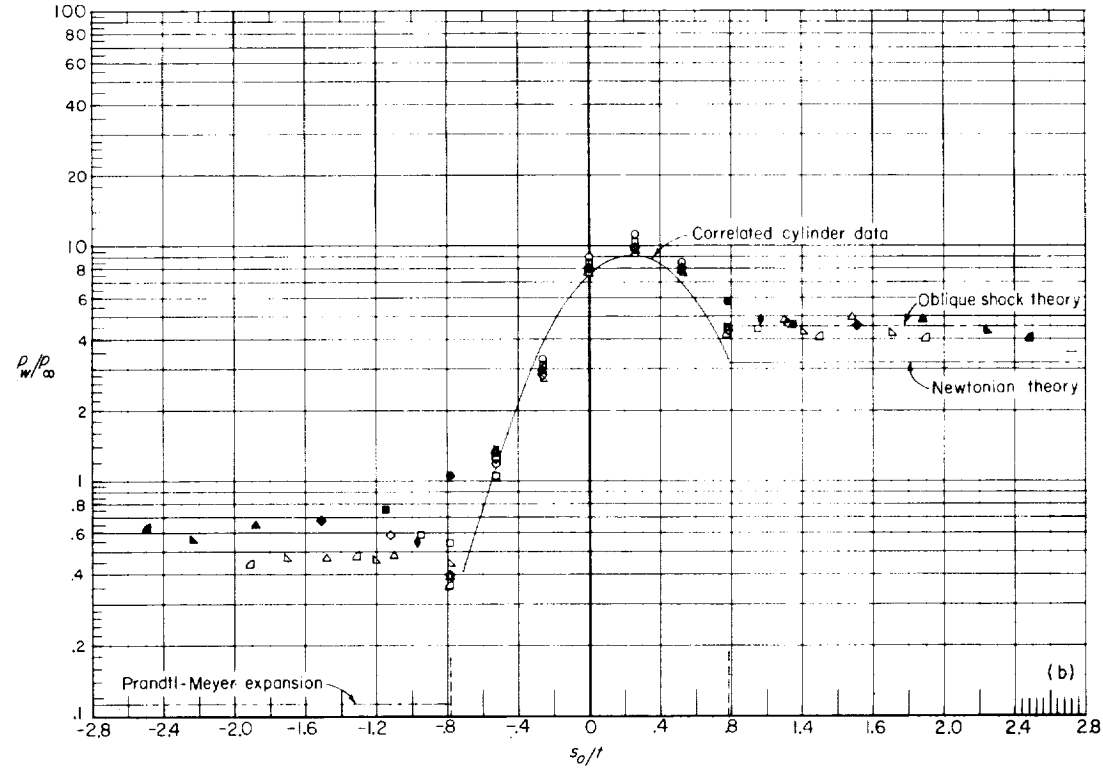

(b) $\alpha = 10.5^{\circ}$.

Figure 23.- Pressure distribution normal to the leading edge on sharp-prow slab delta wing at various stations along the leading edge at angle of attack. $M_\infty = 6.8$; $R_{\infty,t} = 2.4 \times 10^5$; air.

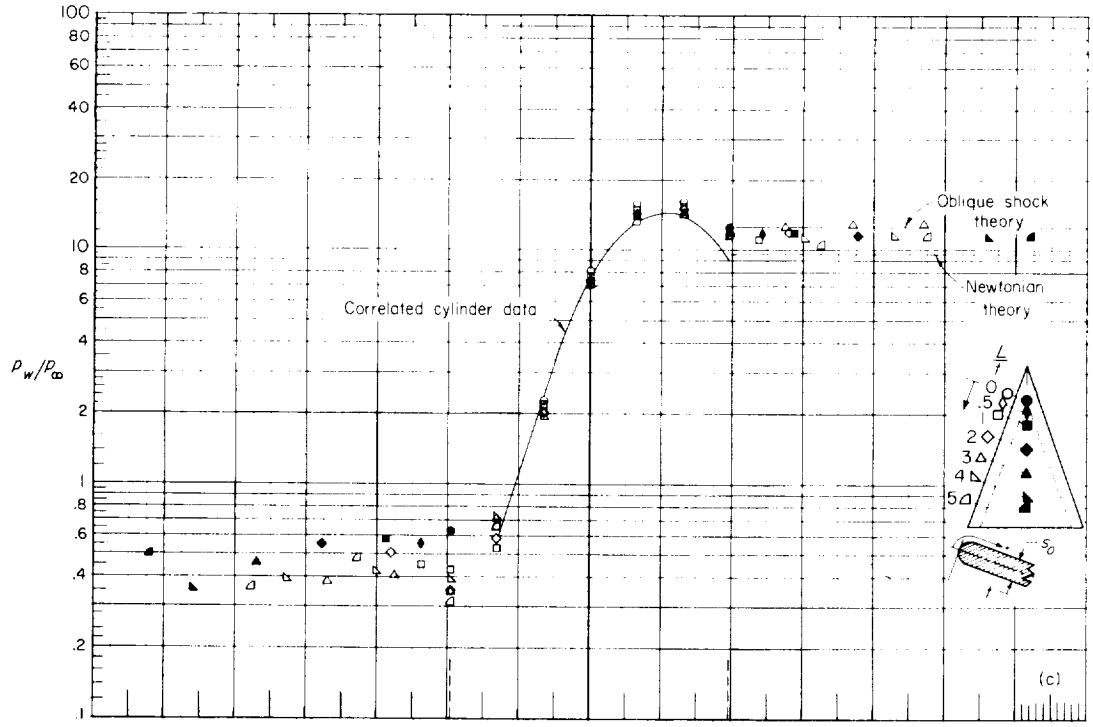

(c) $\alpha = 21.2^\circ$.

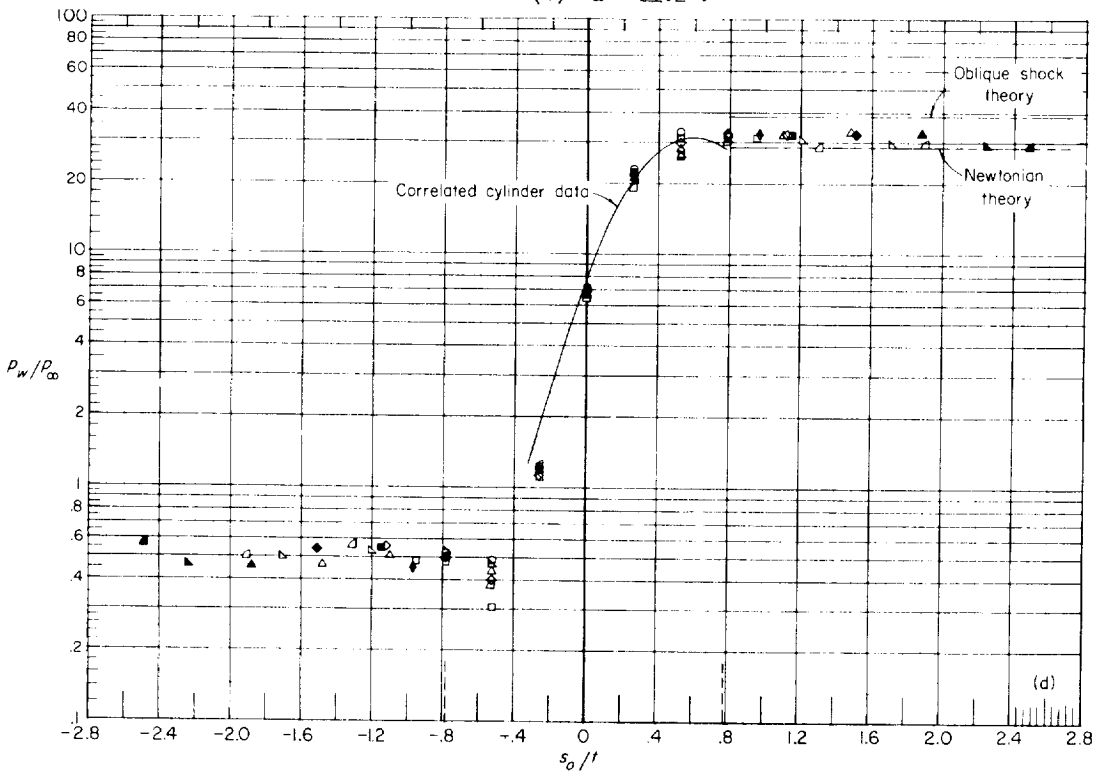

(d) $\alpha = 40.2^\circ$.

Figure 23.- Continued.

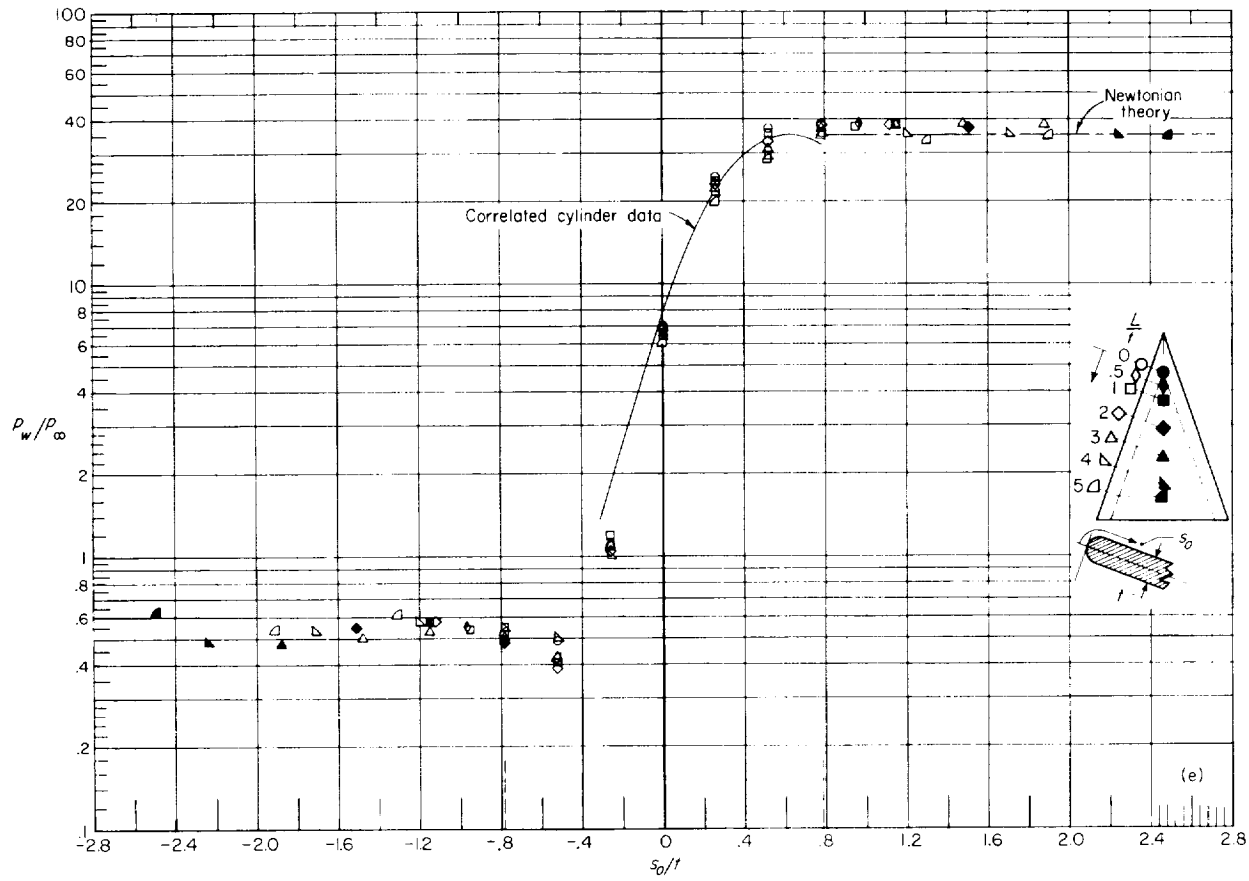

(e) $\alpha = 46^\circ$.

Figure 23.- Concluded.

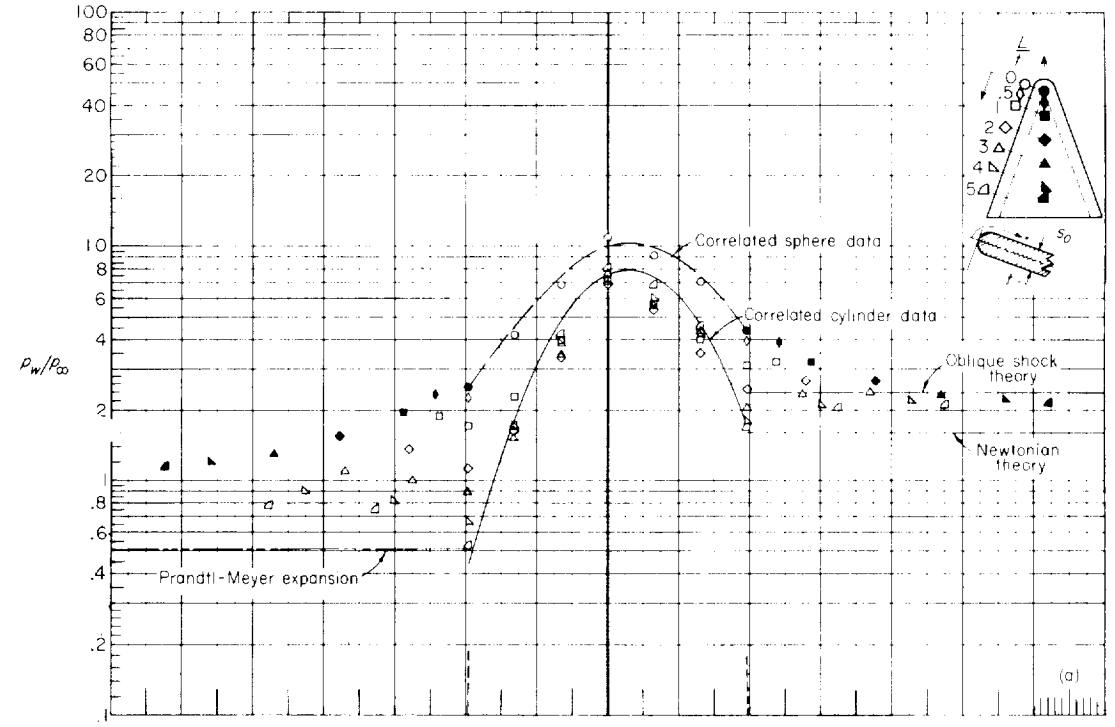

(a) $\alpha = 5.5^\circ$.

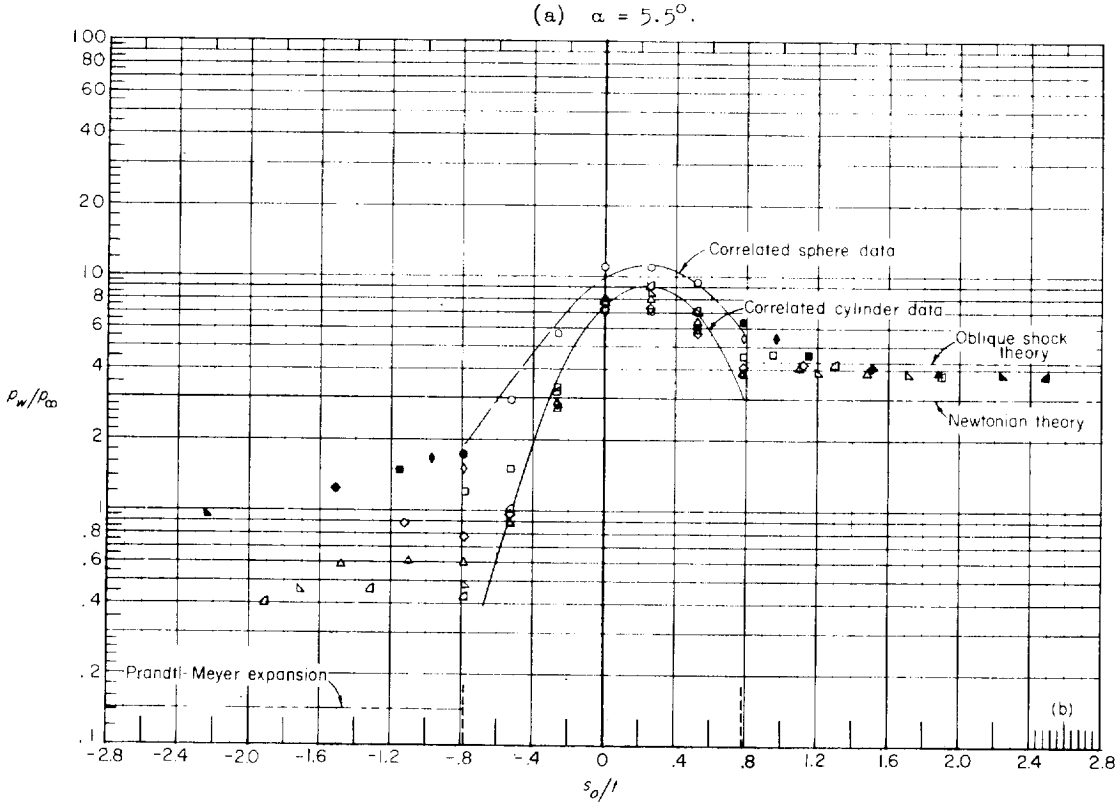

(b) $\alpha = 10^\circ$.

Figure 24.- Pressure distribution normal to the leading edge on blunt-prow slab delta wing at various stations along the leading edge at angle of attack. $M_\infty = 6.8$; $R_{\infty,t} = 2.4 \times 10^5$; air.

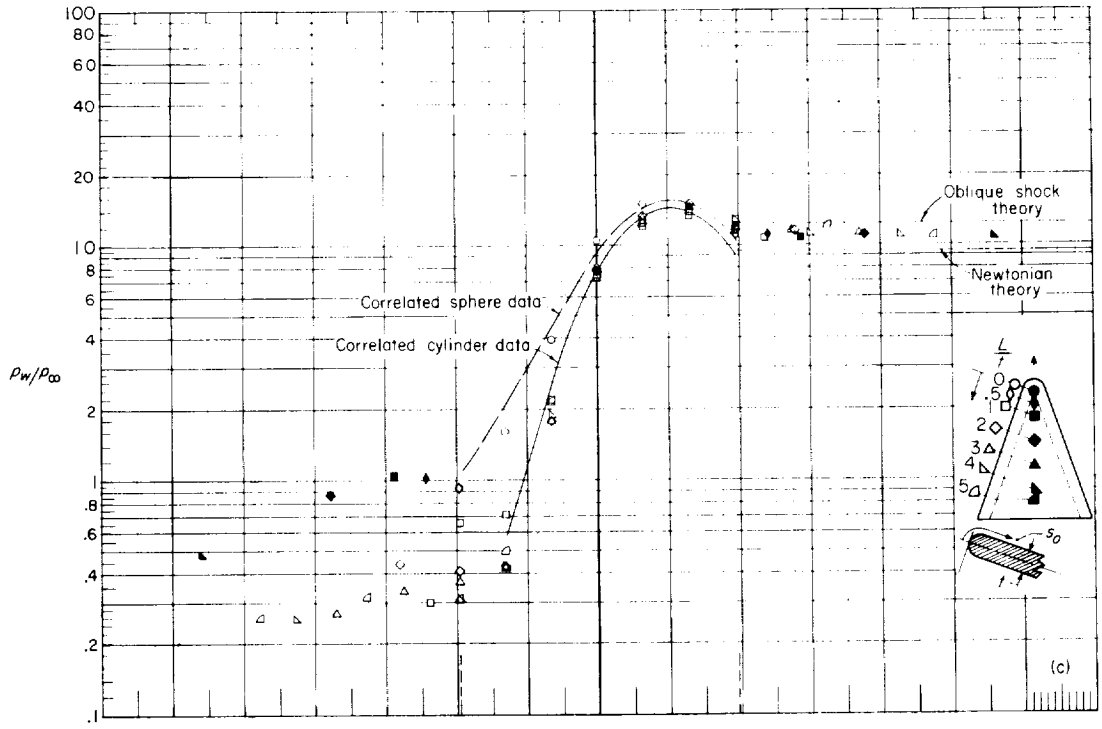

(c) $\alpha = 21^\circ$.

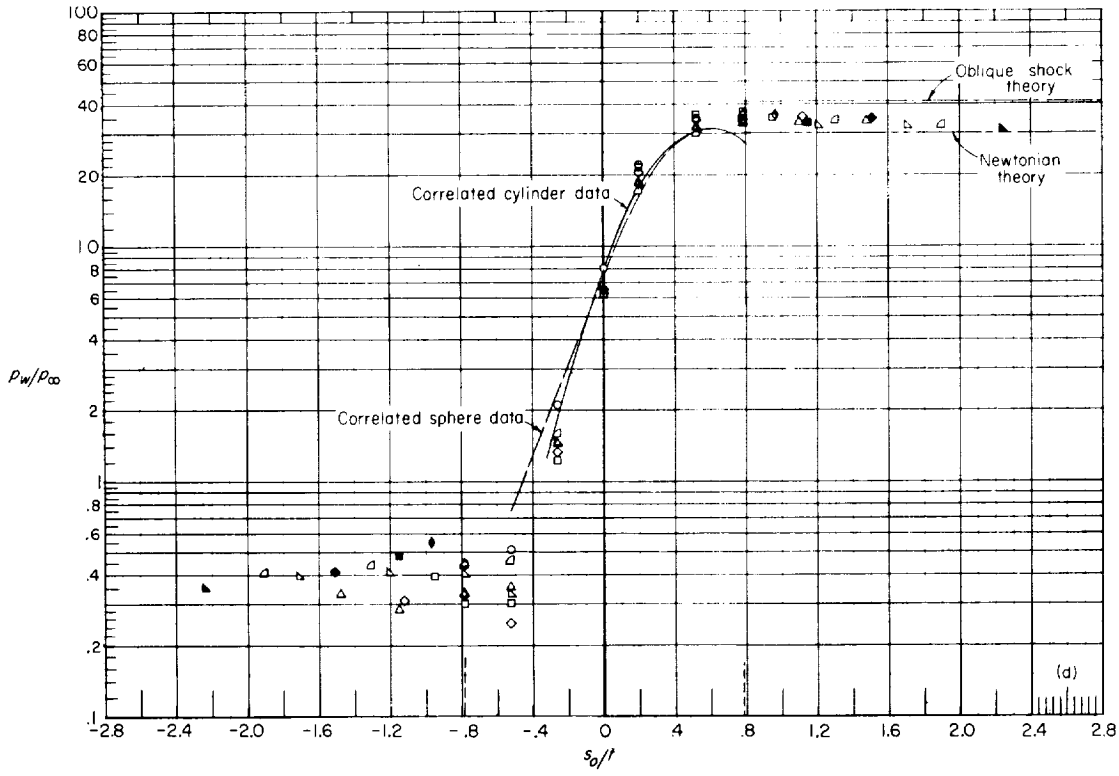

(d) $\alpha = 41.8^\circ$.

Figure 24.- Continued.

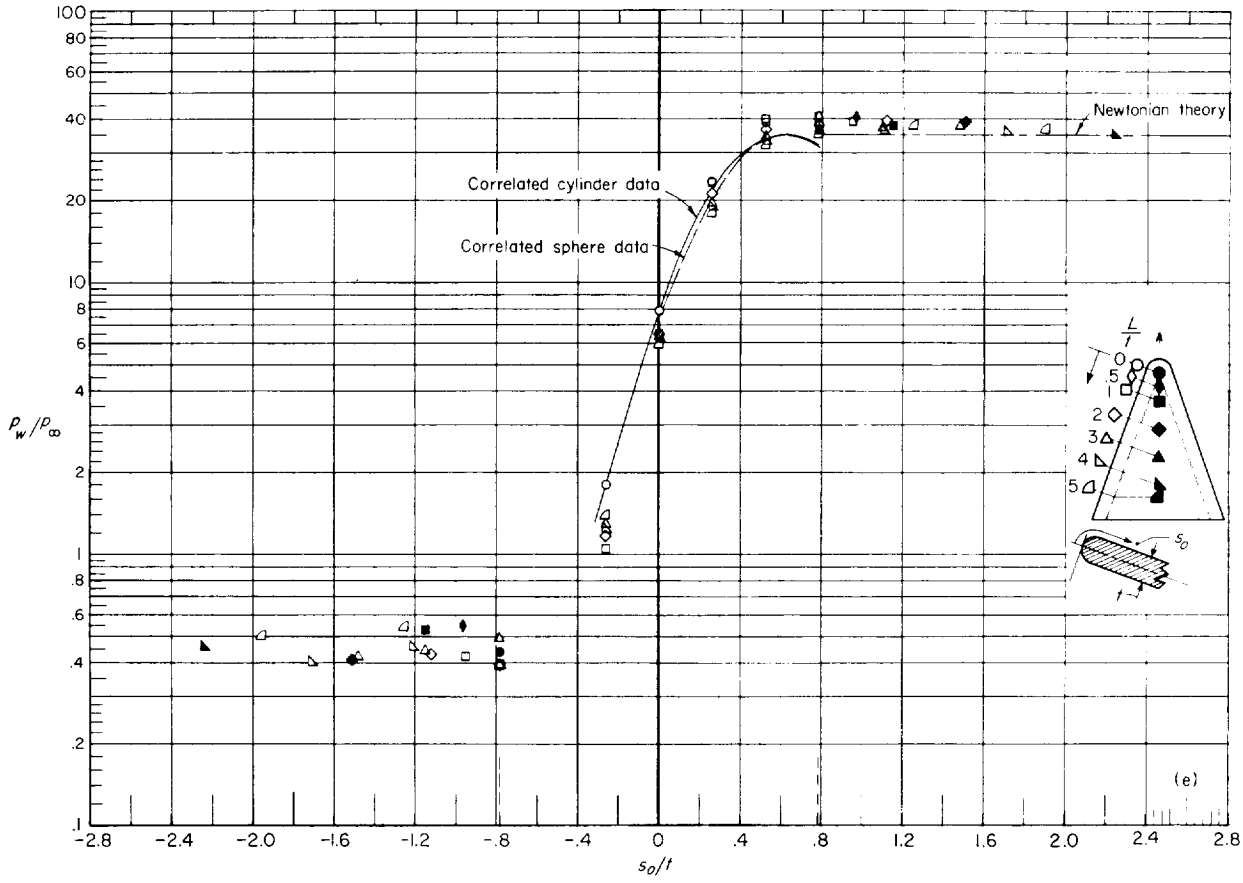

(e) $\alpha = 45.8^\circ$.

Figure 24.- Concluded.

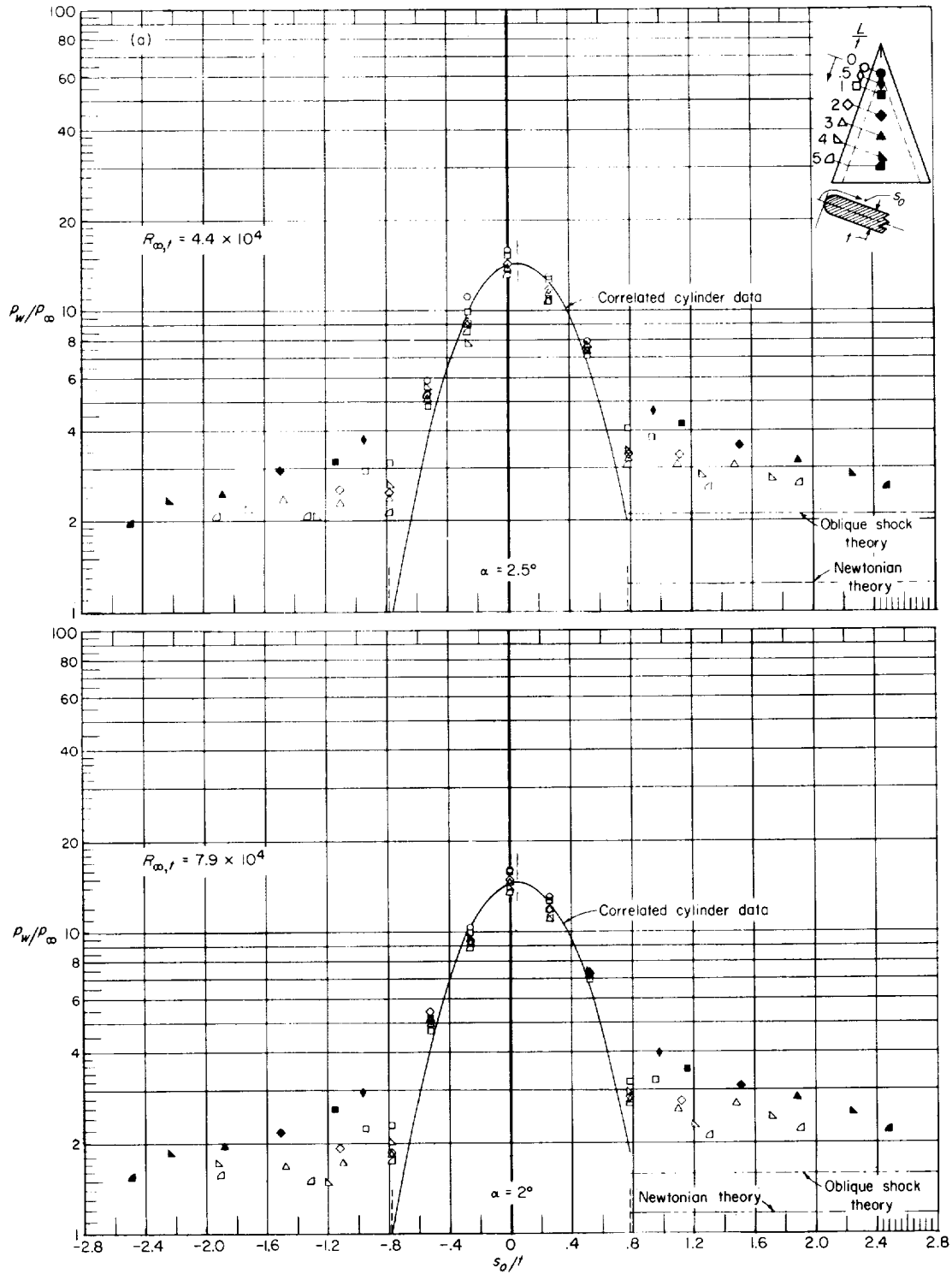

(a) $\alpha \approx 2^{\circ}$.

Figure 25.- Pressure distribution normal to the leading edge on sharp-prow slab delta wing at various stations along the leading edge at angle of attack. $M_\infty = 9.6$; air.

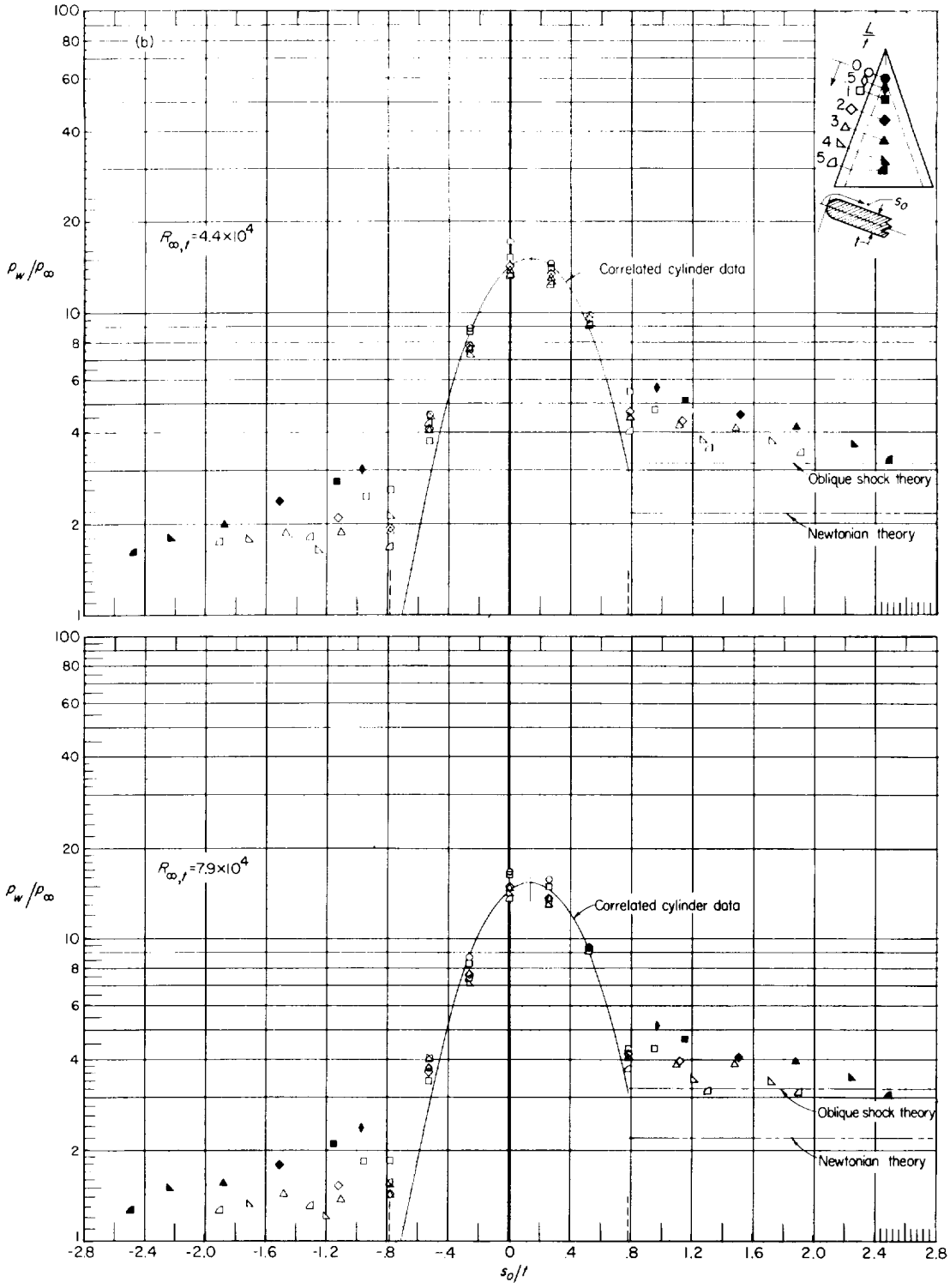

(b) $\alpha = 5.5^\circ$.

Figure 25.- Continued.

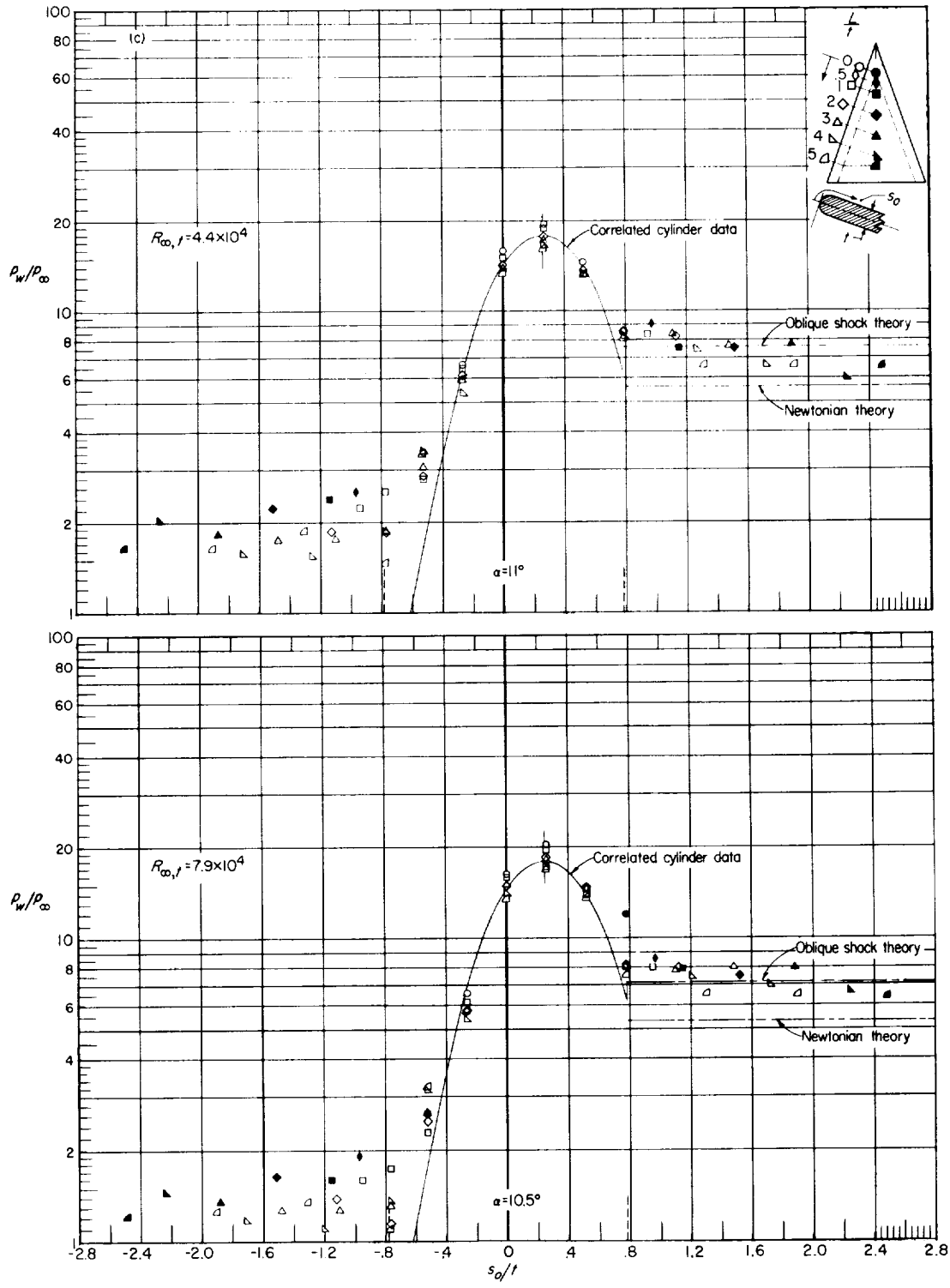

(c) $\alpha \approx 10.5^\circ$.

Figure 25.- Continued.

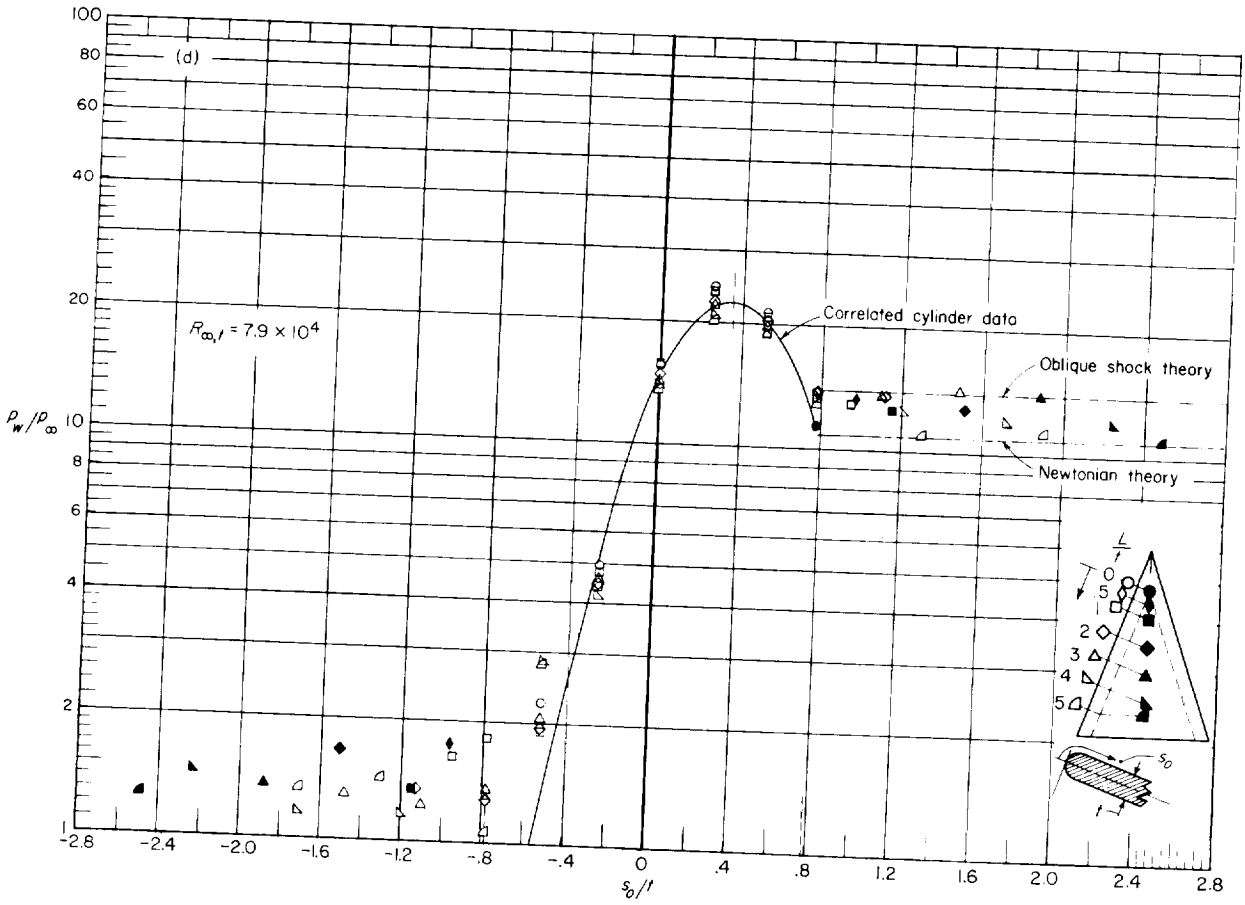

(d) $\alpha = 16°$.

Figure 25.- Continued.

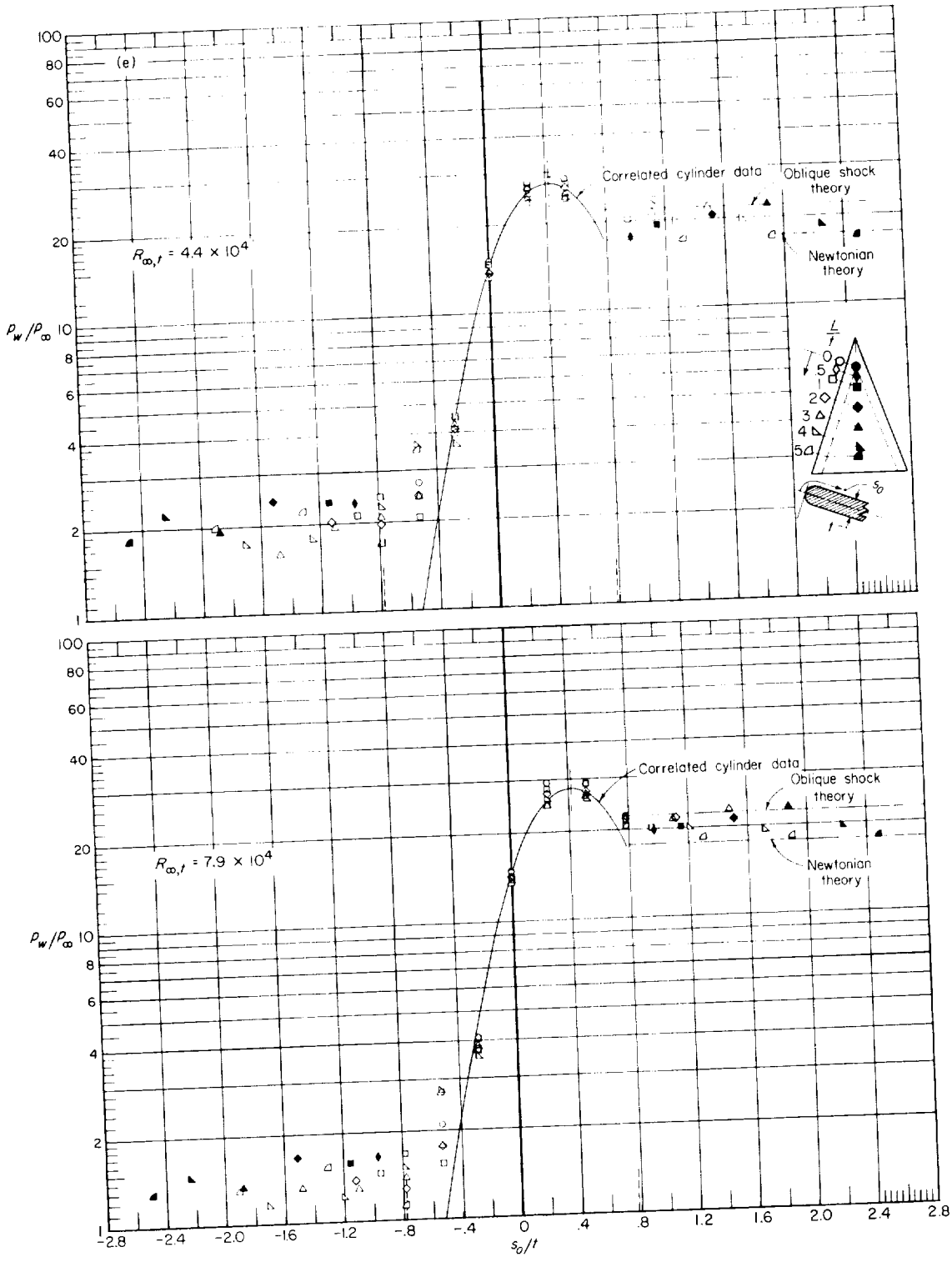

(e) $\alpha = 21^\circ$.

Figure 25.- Continued.

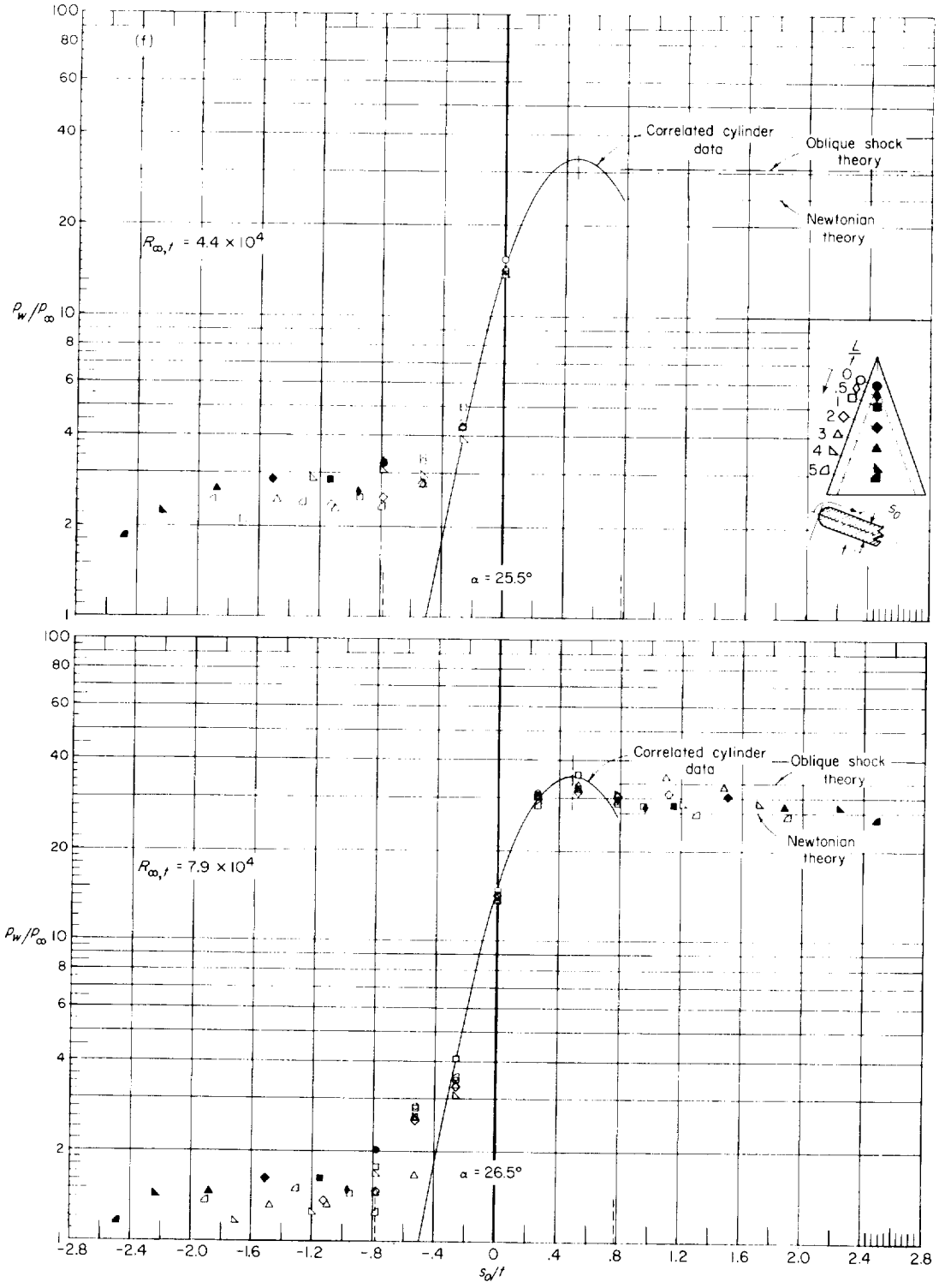

(f) $\alpha \approx 26°$.

Figure 25.- Continued.

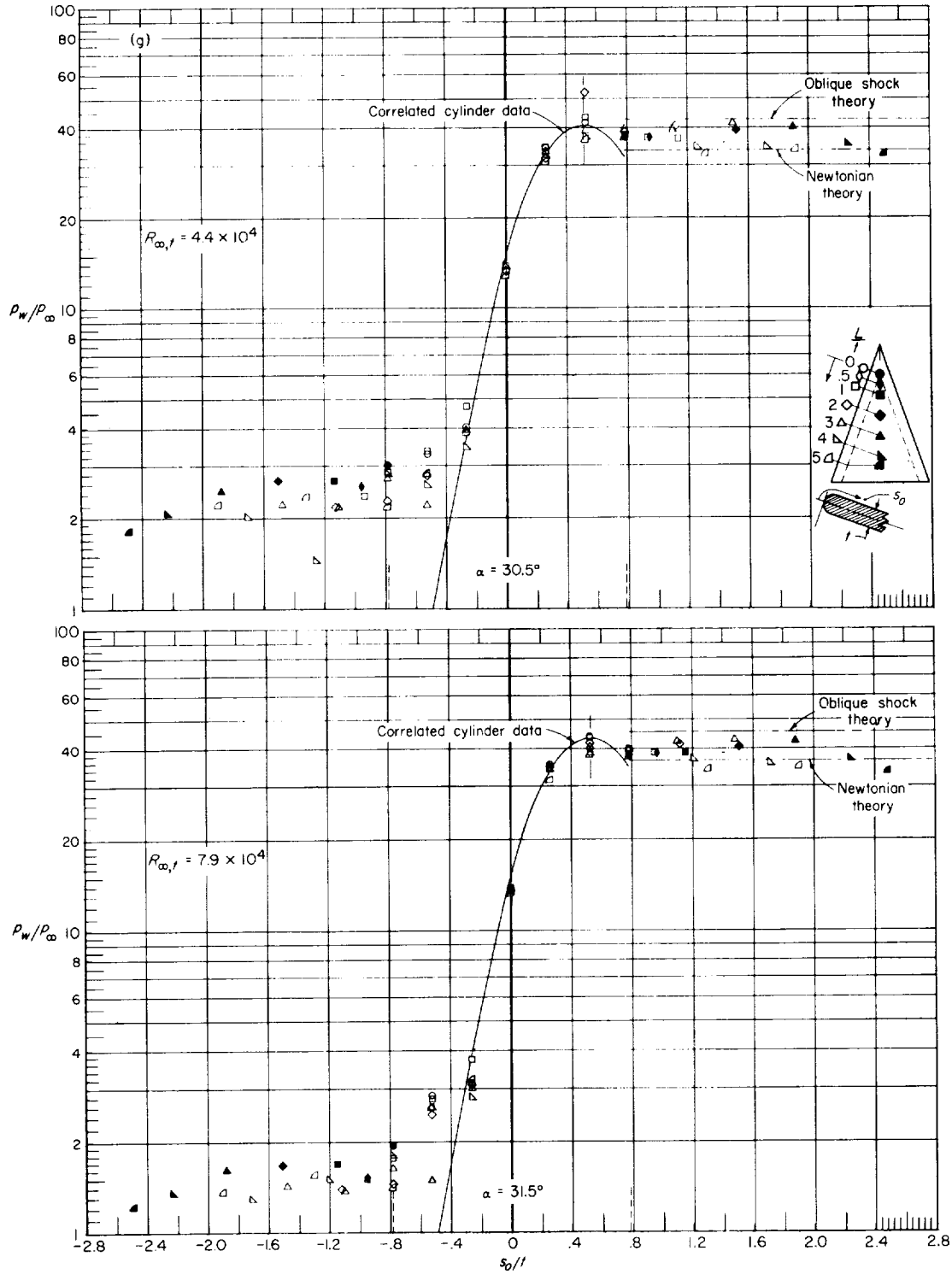

(g) $\alpha \approx 31^\circ$.

Figure 25.- Continued.

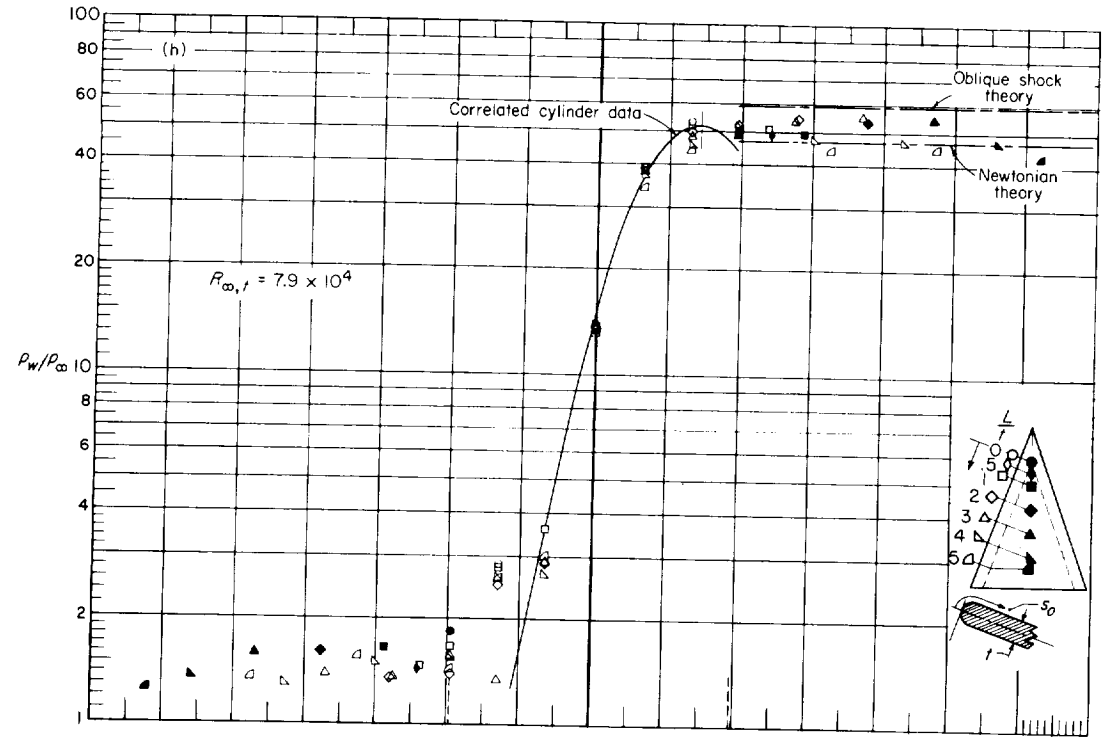

(h) $\alpha = 36.5°$.

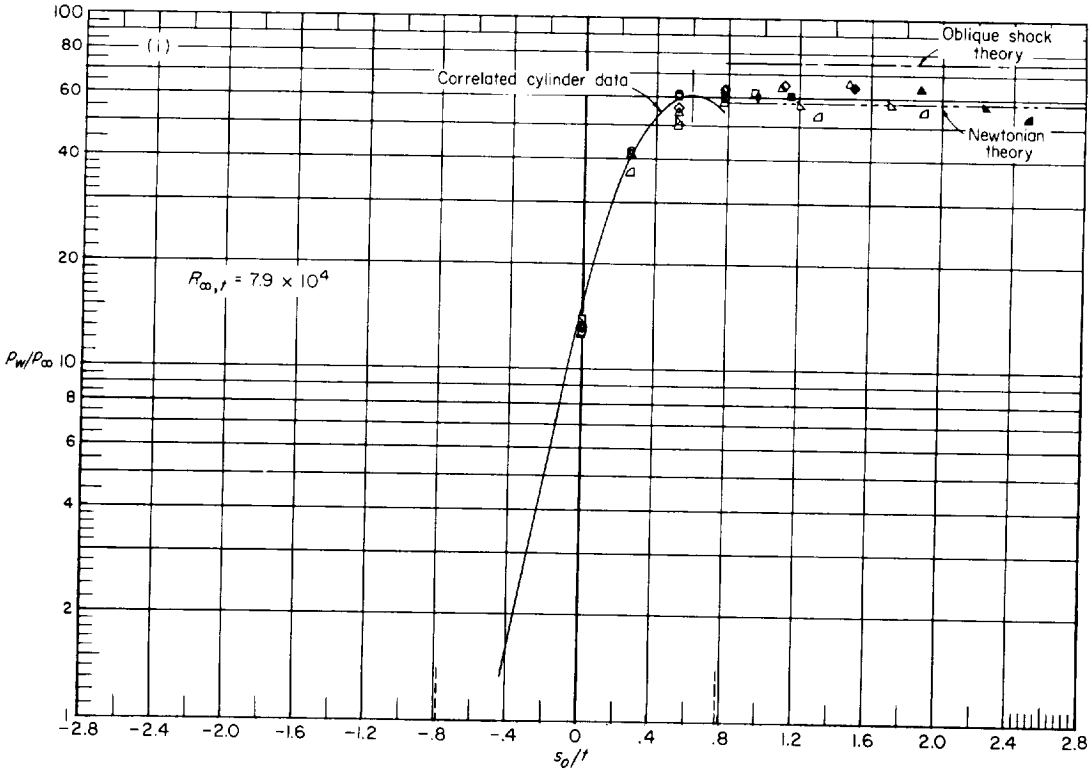

(i) $\alpha = 41.5°$.

Figure 25.- Concluded.

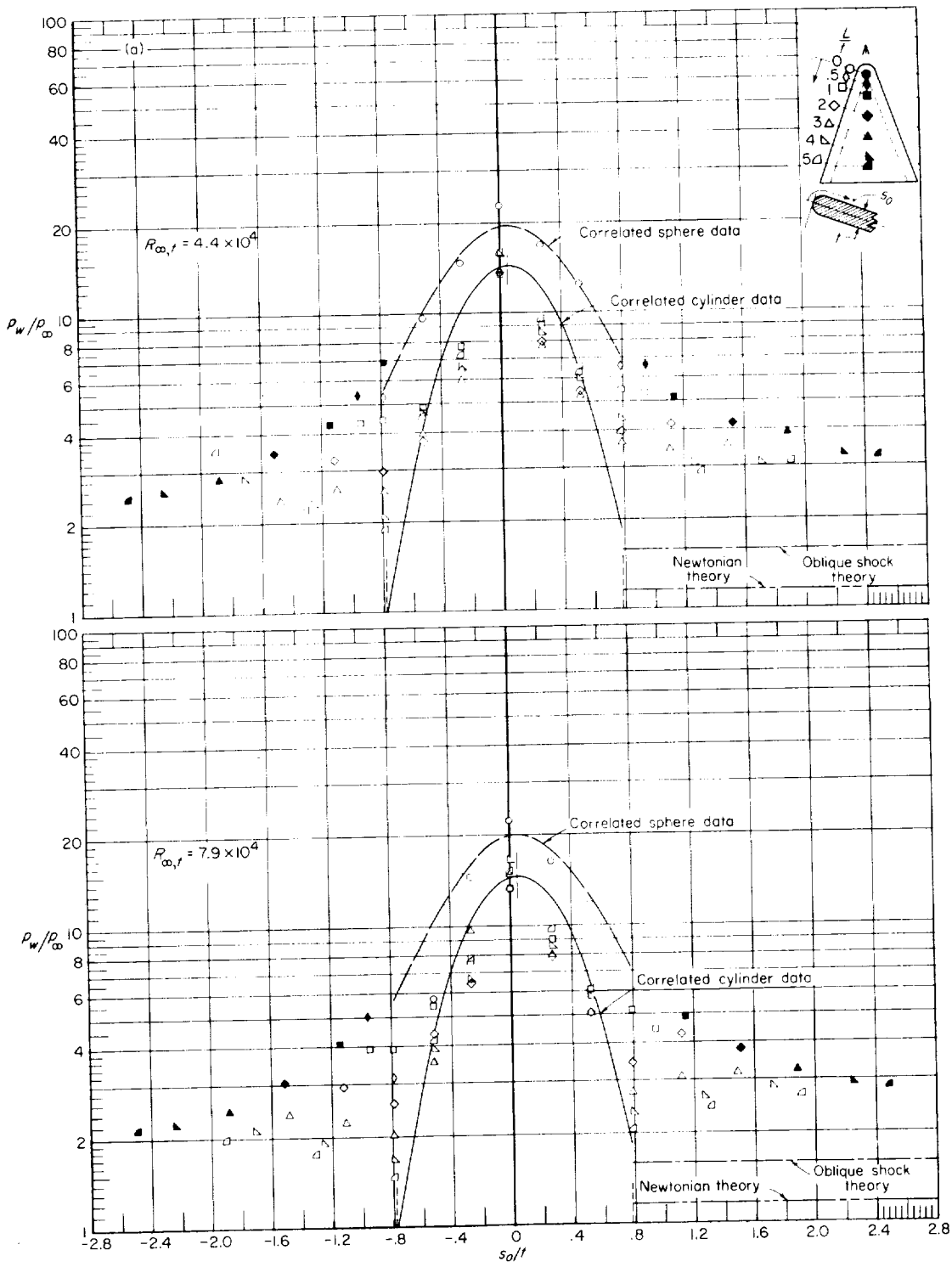

(a) $\alpha = 2^\circ$.

Figure 26.- Pressure distribution normal to the leading edge on blunt-prow slab delta wing at various stations along the leading edge at angle of attack. $M_\infty = 9.6$; air.

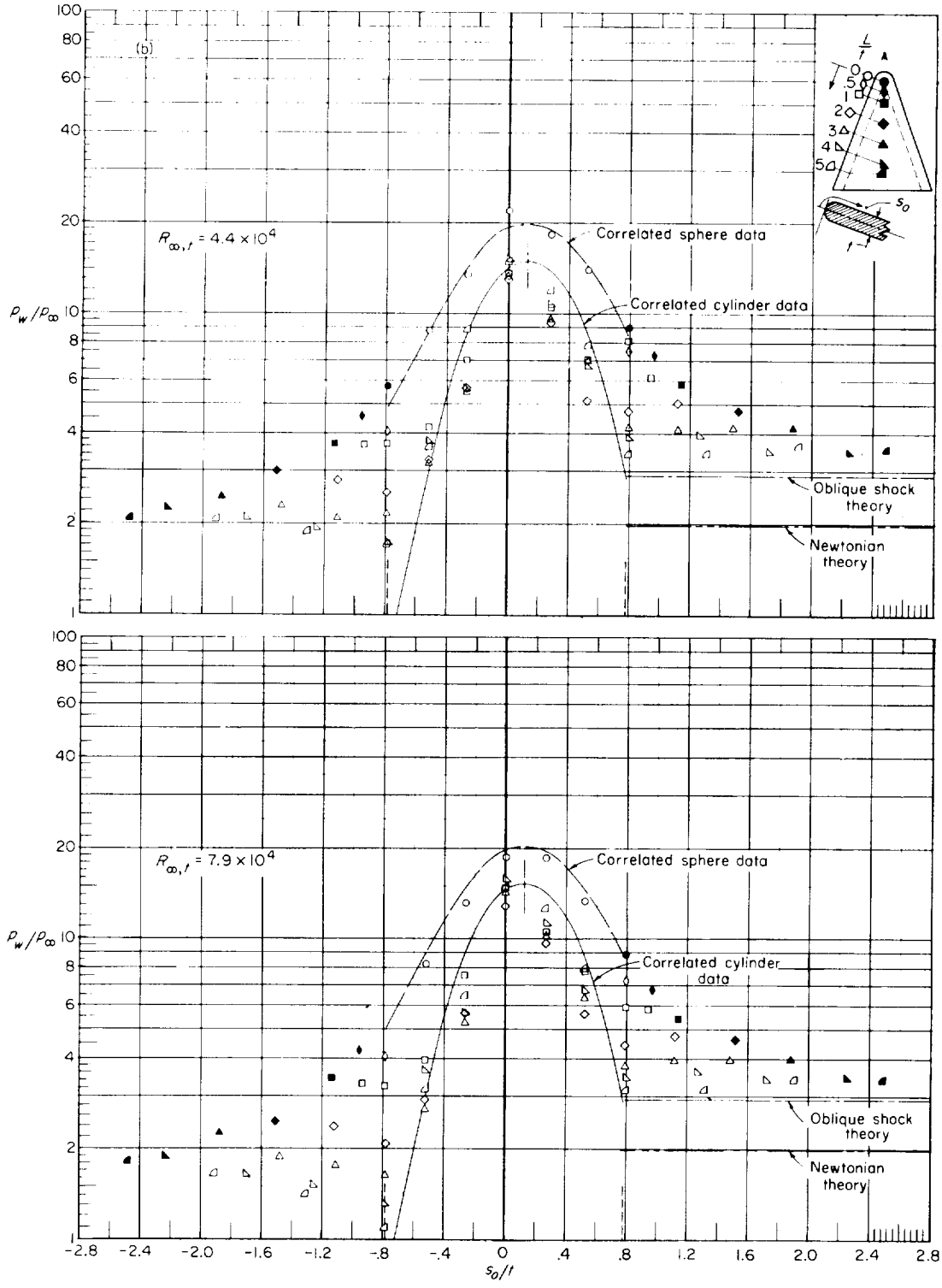

(b) $\alpha = 5^\circ$.

Figure 26.- Continued.

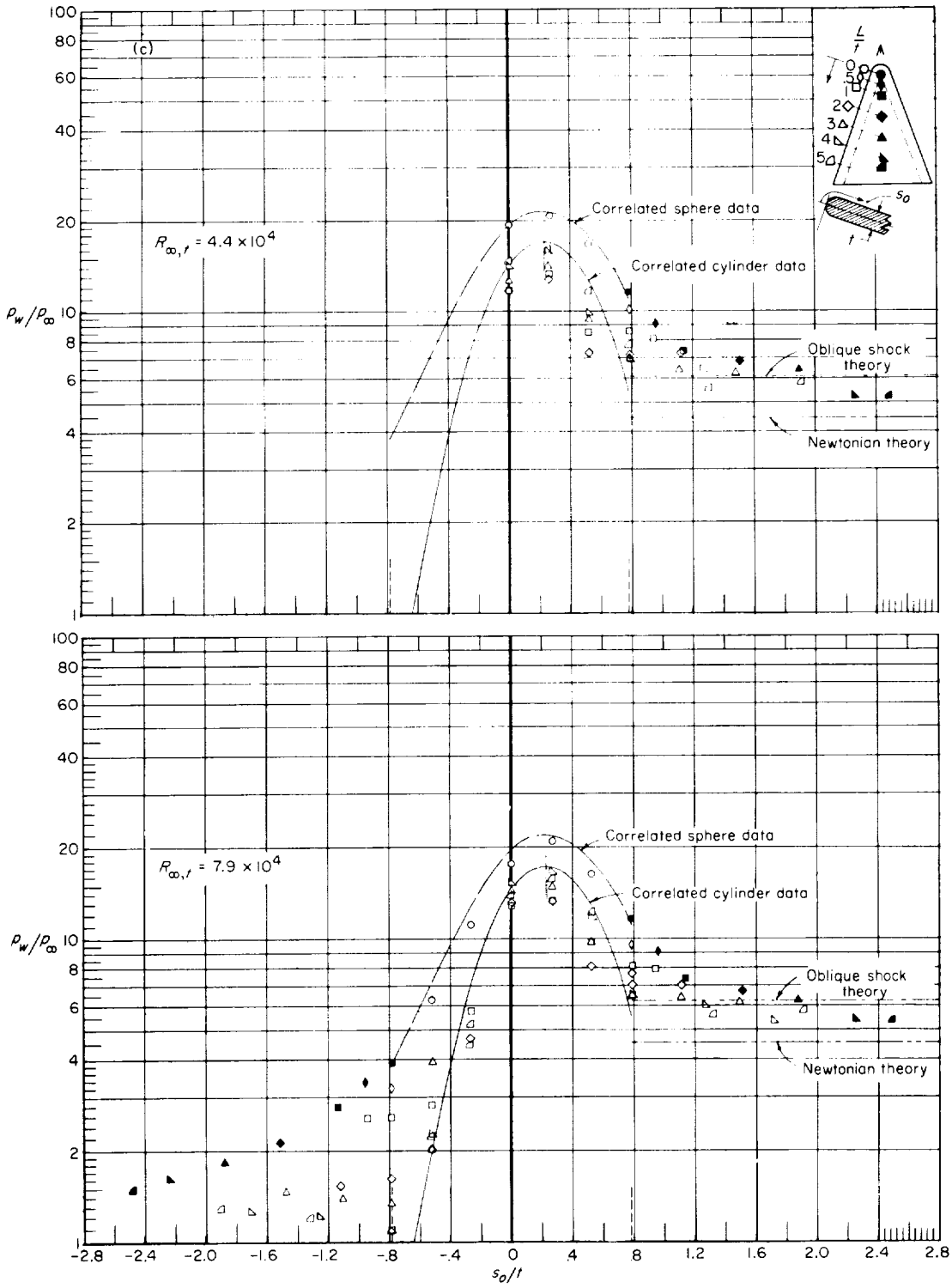

(c) $\alpha = 9.5^\circ$.

Figure 26.- Continued.

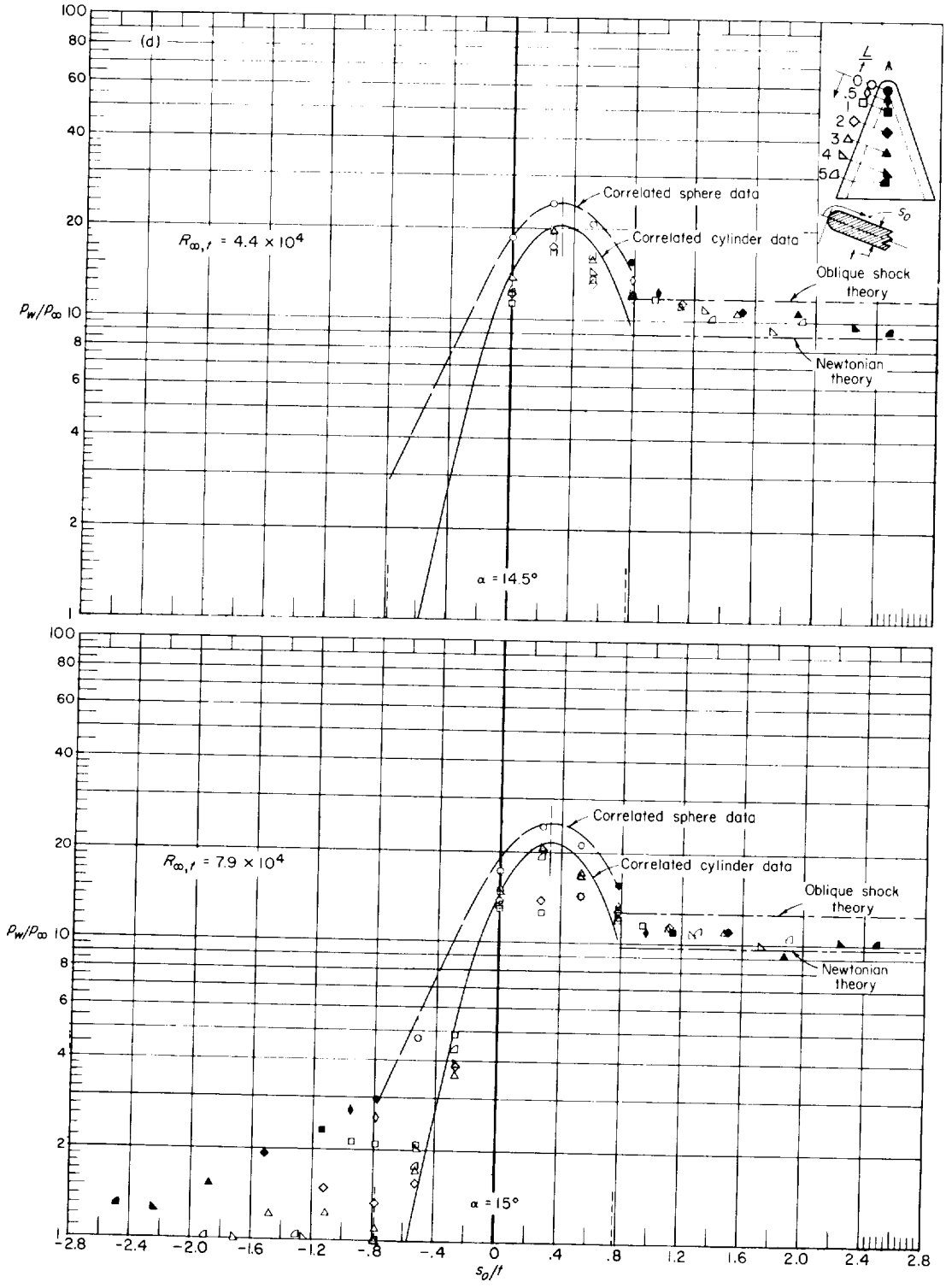

(d) $\alpha \approx 15°$.

Figure 26.- Continued.

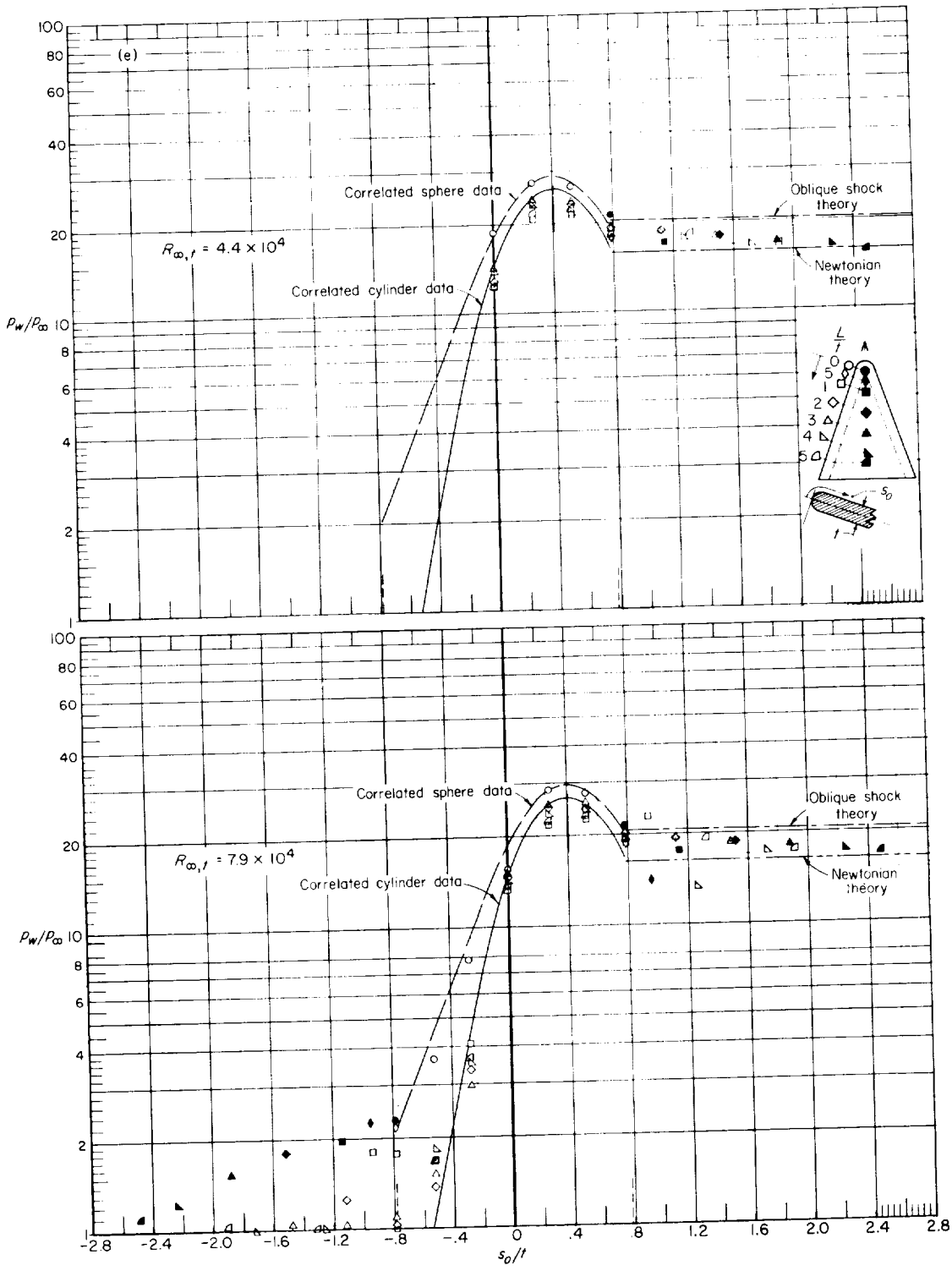

(e) $\alpha = 20^\circ$.

Figure 26.- Continued.

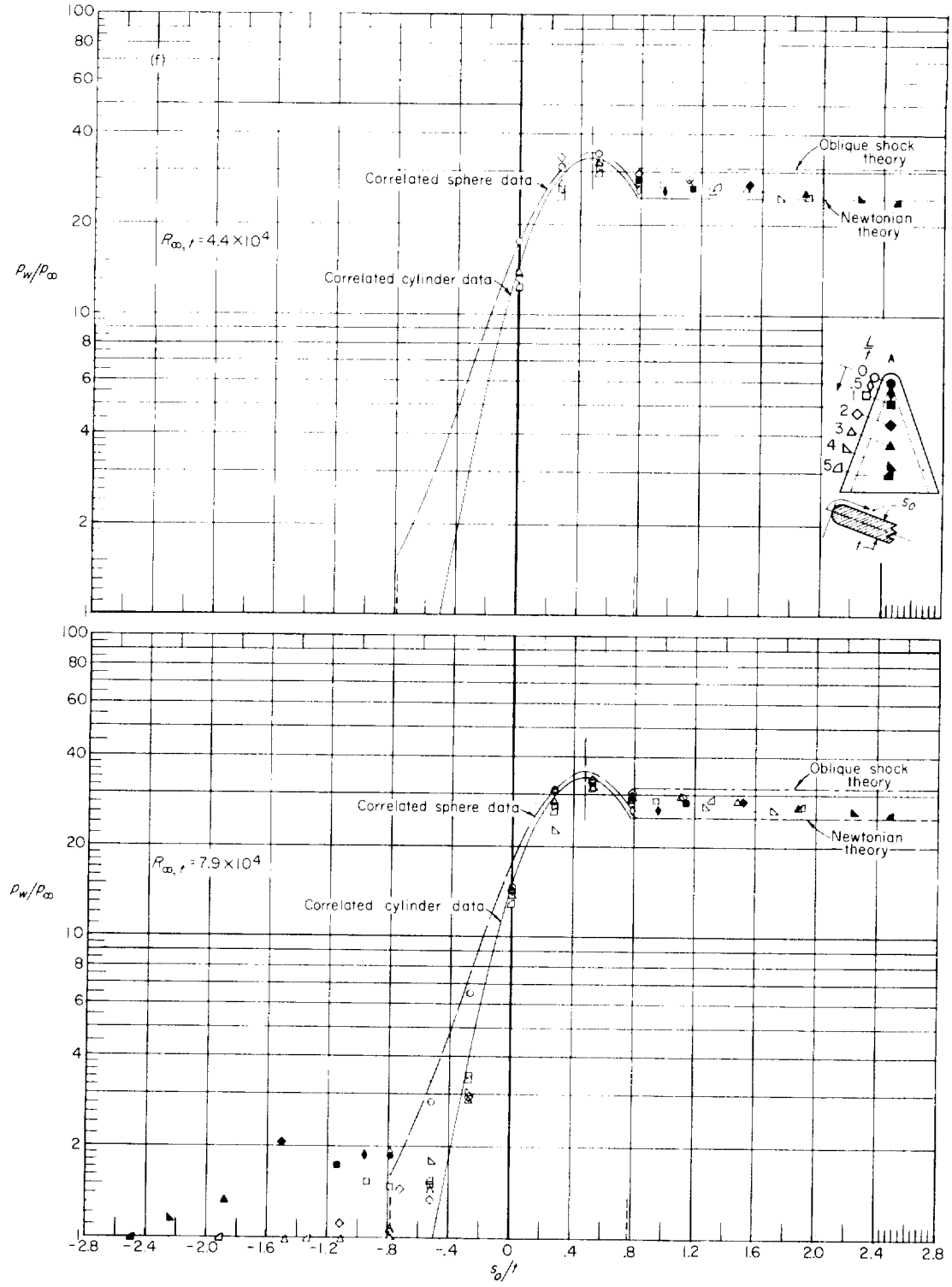

(f) $\alpha = 25.5^\circ$.

Figure 26.- Continued.

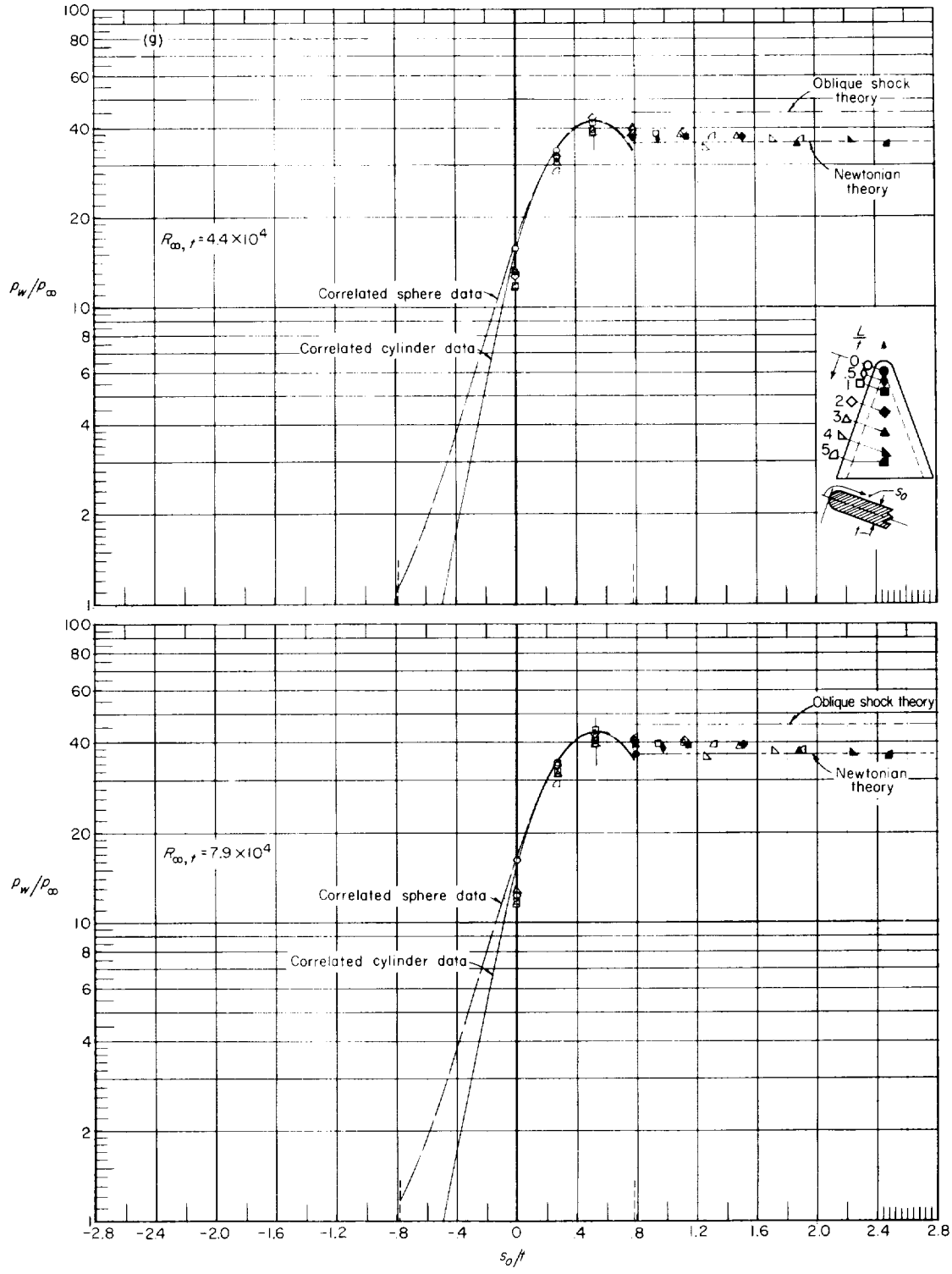

(g) $\alpha = 31.5^\circ$.

Figure 26.- Continued.

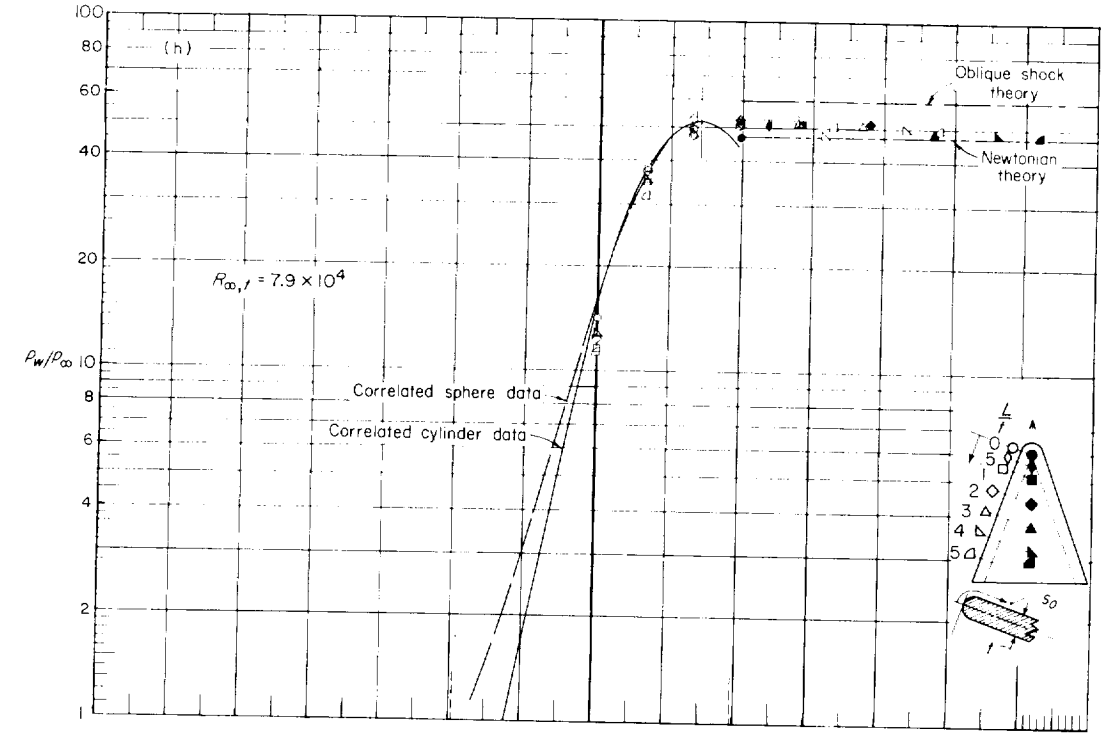

(h) $\alpha = 36.5^\circ$.

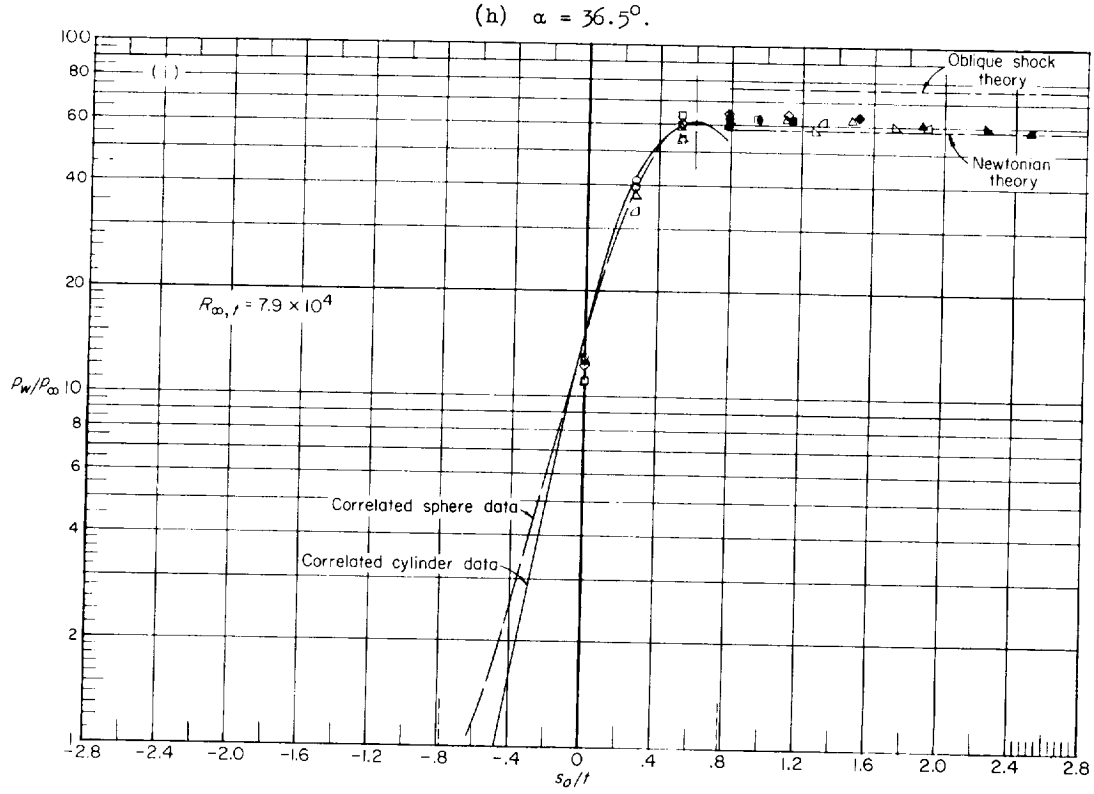

(i) $\alpha = 41.5^\circ$.

Figure 26.- Concluded.

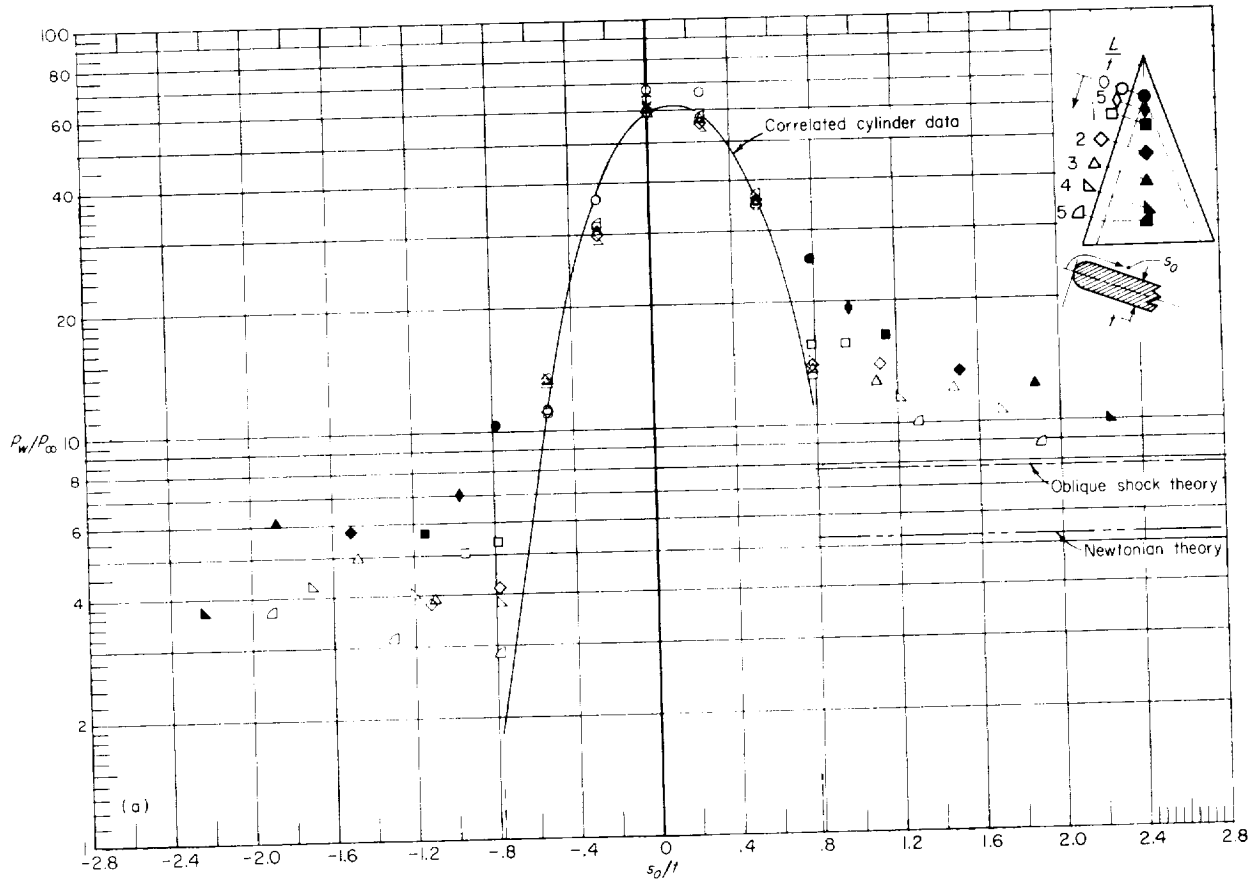

(a) $\alpha = 5^{\circ}$; sharp prow.

Figure 27.- Pressure distribution normal to leading edge on slab delta wing at various stations along the leading edge at angle of attack. $M_\infty = 18.4$; $R_{\infty,t} = 5.3 \times 10^5$; helium.

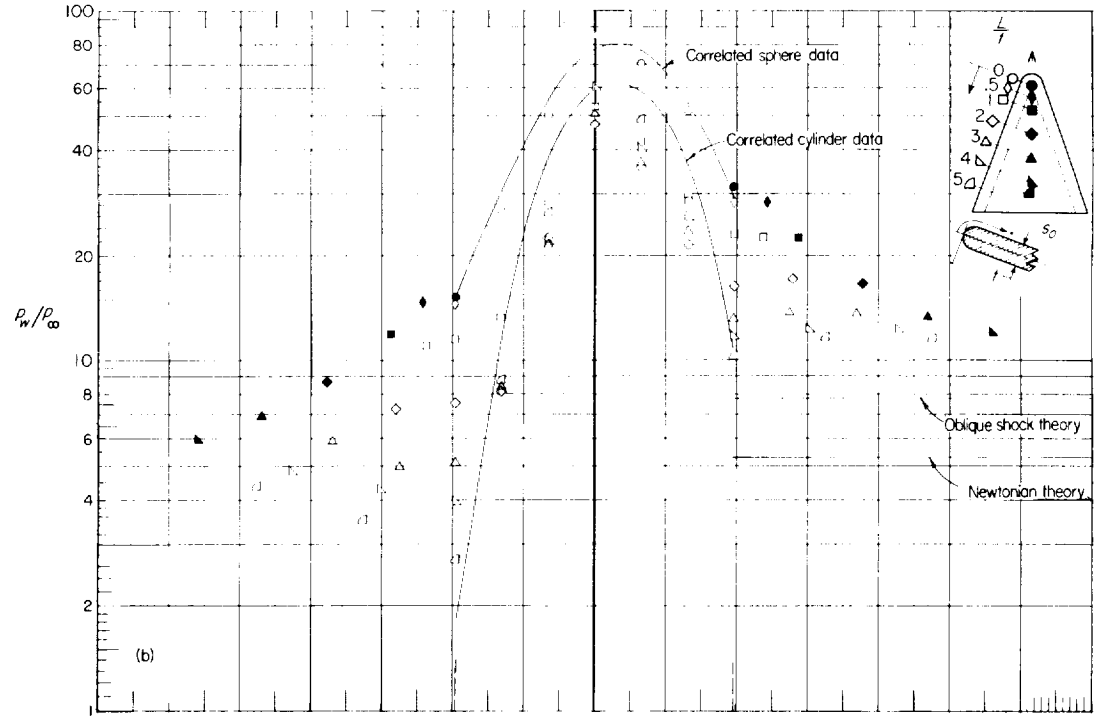

(b) $\alpha = 5^\circ$; blunt prow.

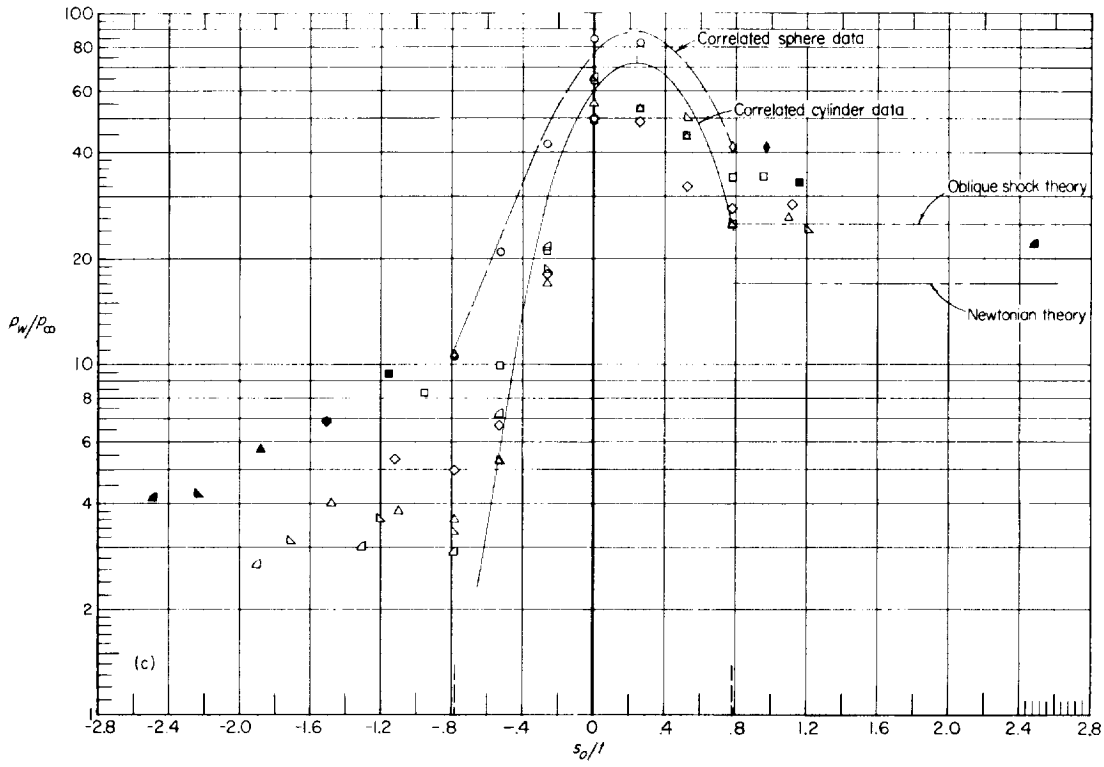

(c) $\alpha = 10^\circ$; blunt prow.

Figure 27.- Concluded.

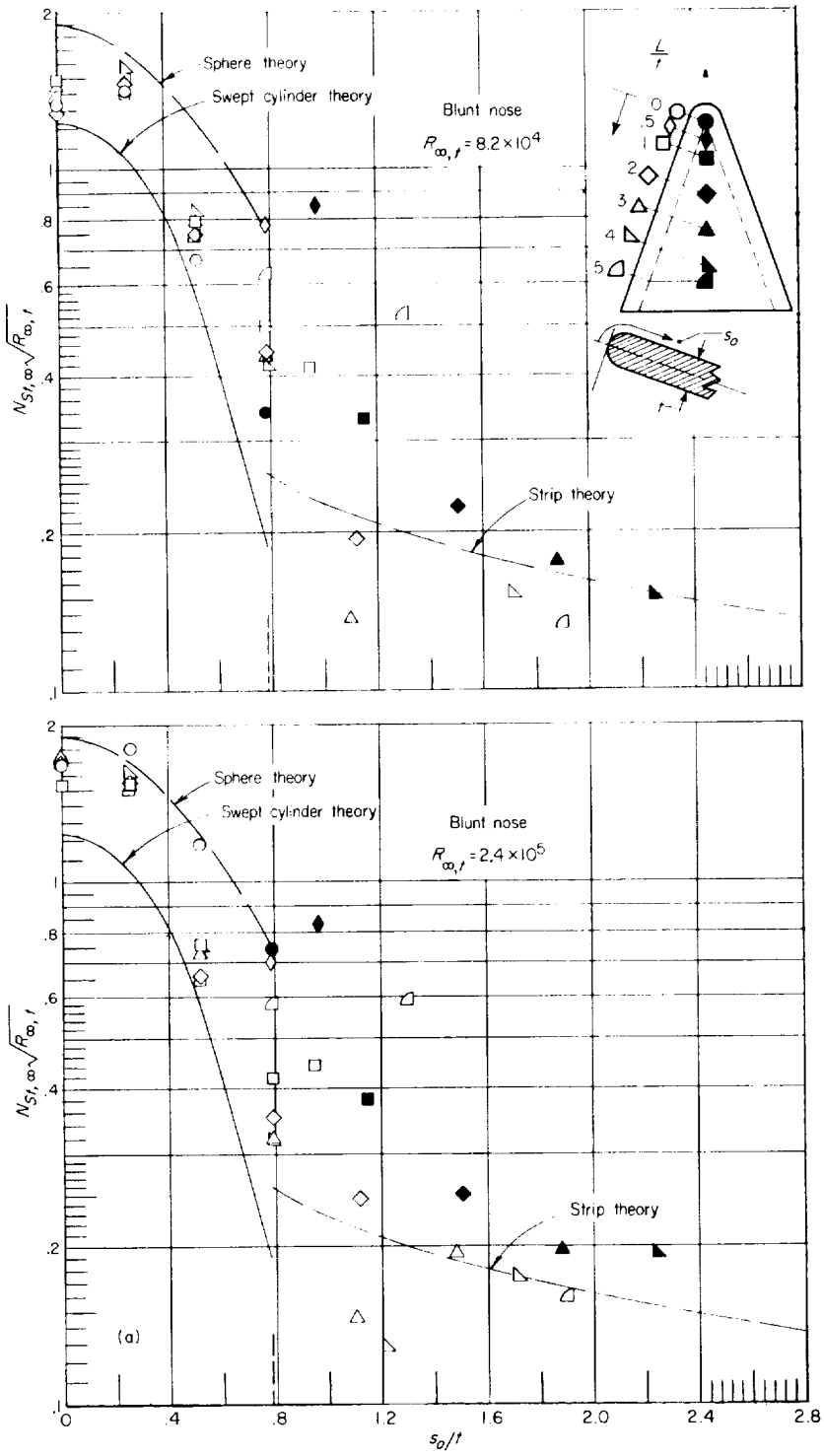

(a) $M_\infty = 6.8$; air.

Figure 28.- Stanton number distribution normal to the leading edge on slab delta wing at various stations along the leading edge at an angle of attack of 0°.

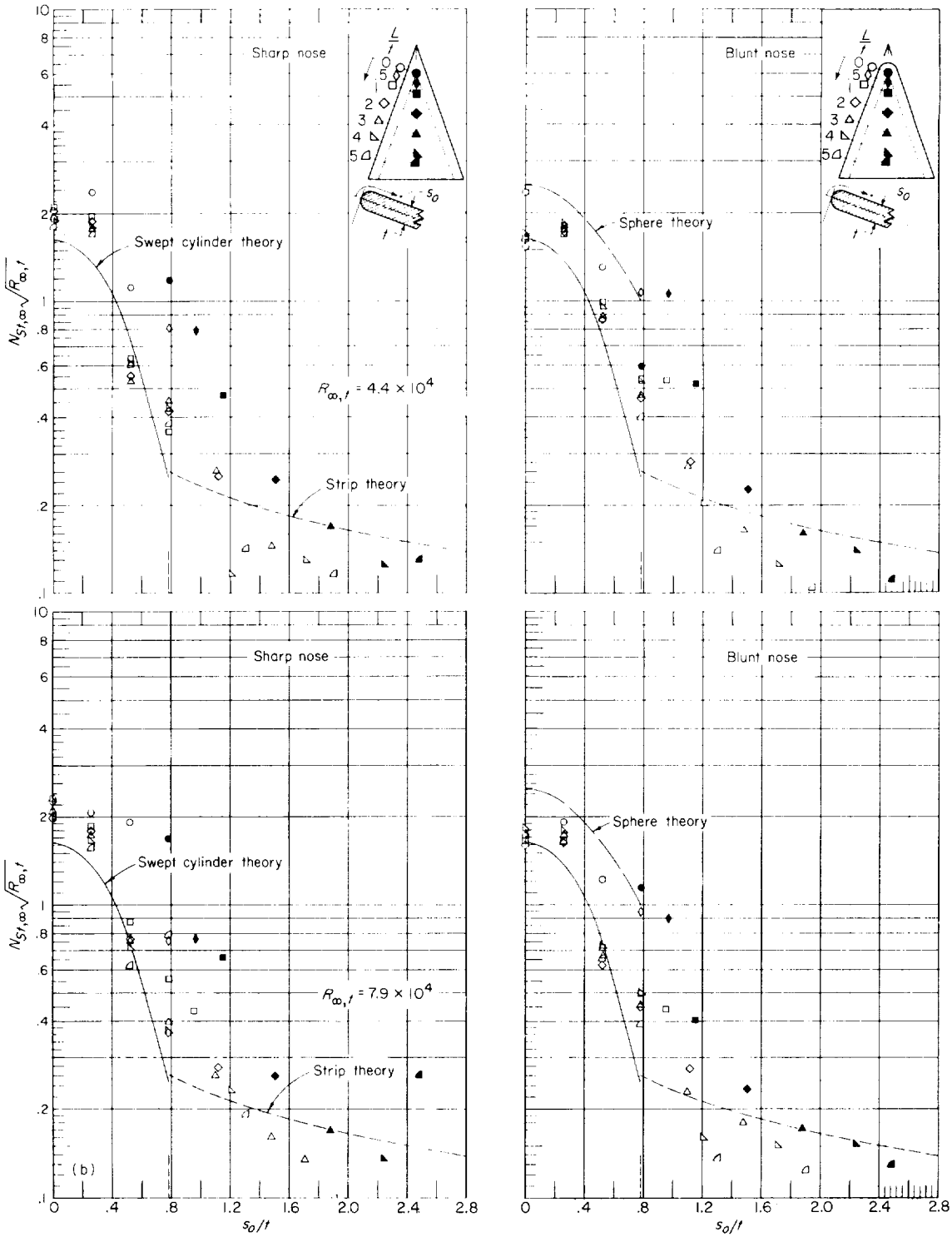

(b) $M_\infty = 9.6$; air.

Figure 28.- Concluded.

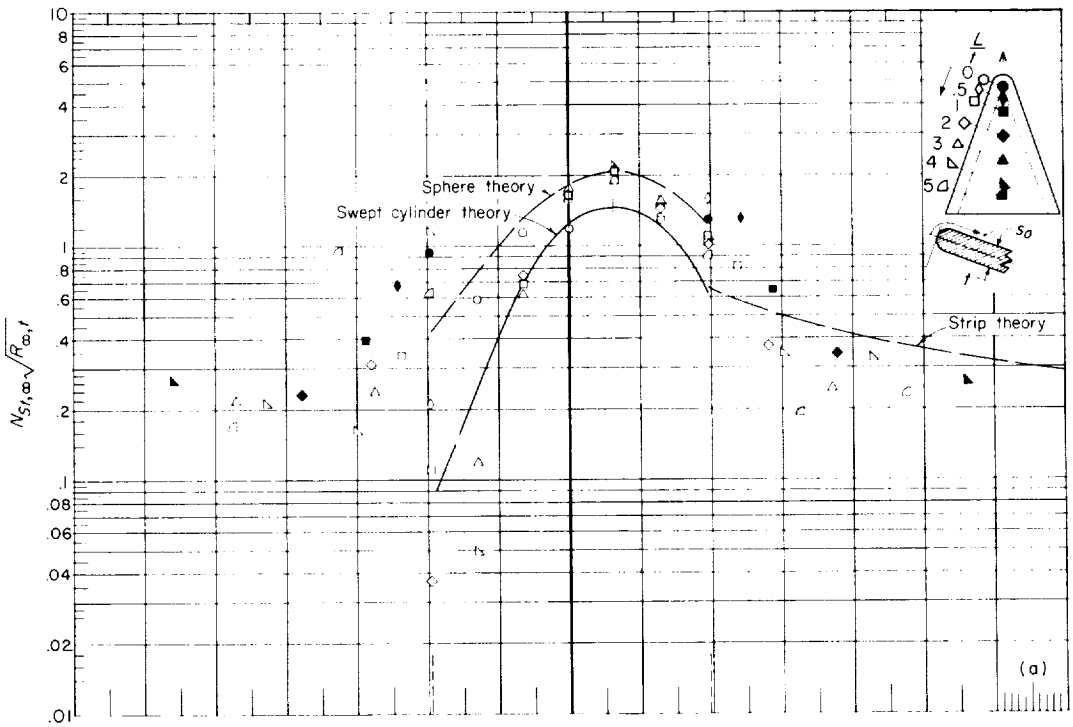

(a) $\alpha = 10.4^\circ$.

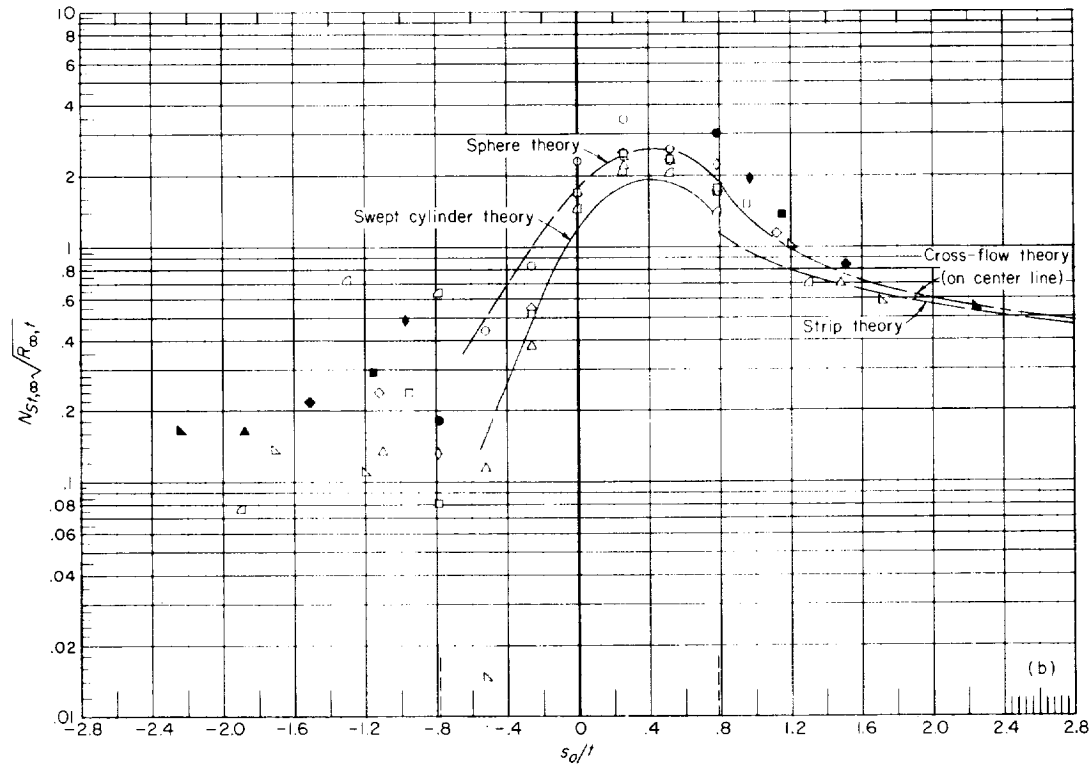

(b) $\alpha = 20.6^\circ$.

Figure 29.- Stanton number distribution normal to the leading edge on blunt-prow delta wing at various stations along the leading edge at angle of attack. $M_\infty = 6.8$; $R_{\infty,t} = 2.4 \times 10^5$; air.

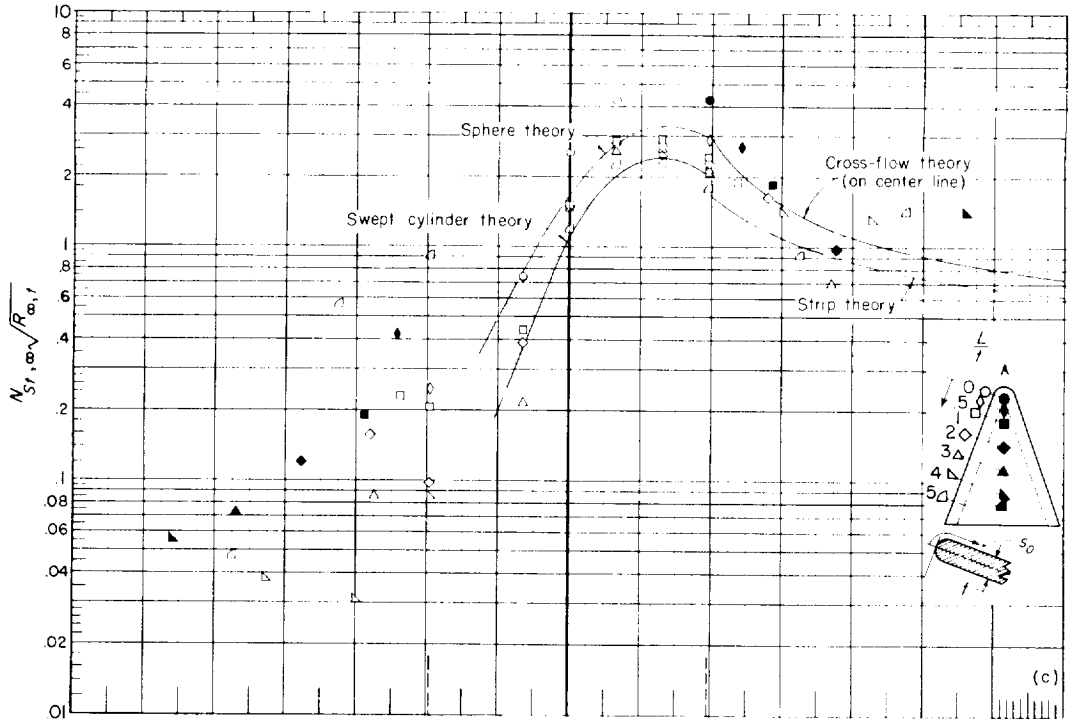

(c) $\alpha = 30^{\circ}$.

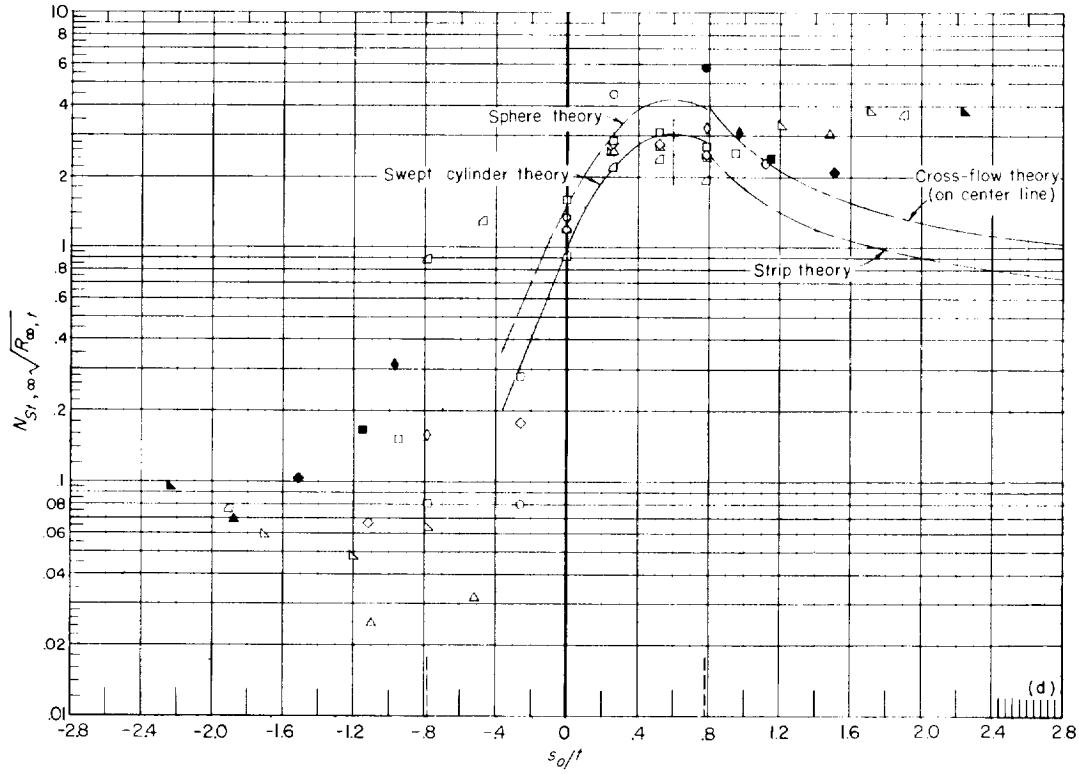

(d) $\alpha = 41.1^{\circ}$.

Figure 29.- Continued.

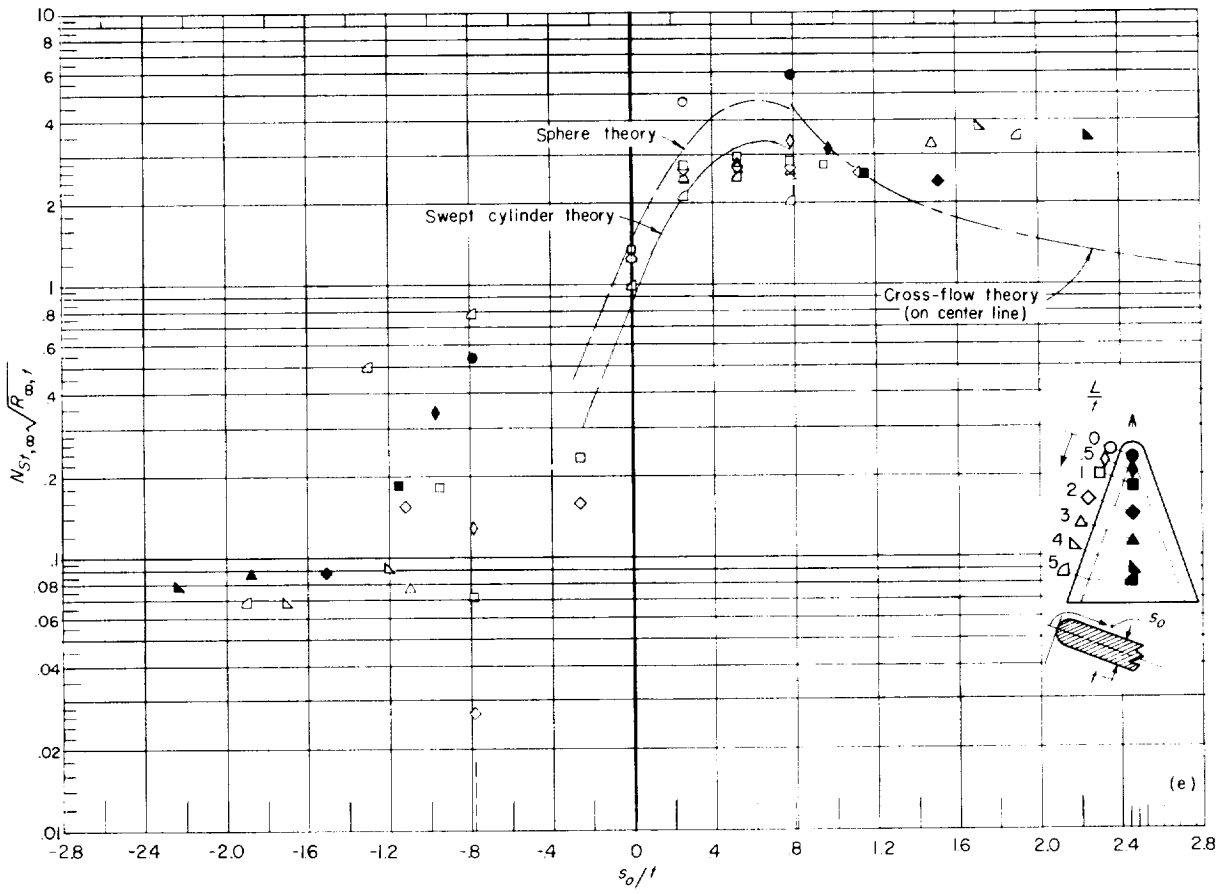

(e) $\alpha = 46.3^{\circ}$.

Figure 29.- Concluded.

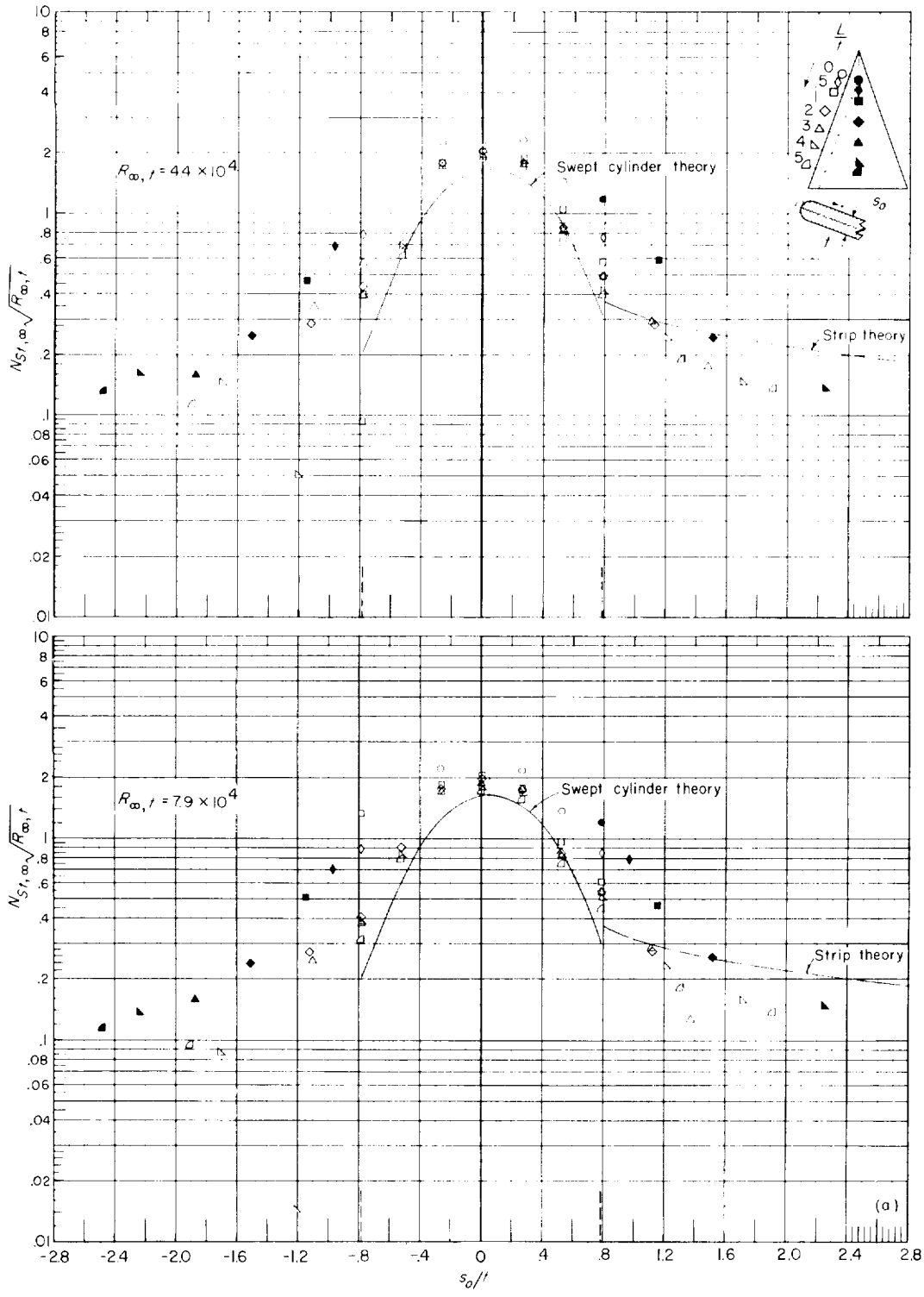

(a) $\alpha = 2^\circ$.

Figure 30.- Stanton number distribution normal to the leading edge on sharp-prow delta wing at various stations along the leading edge at angle of attack. $M_\infty = 9.6$; air.

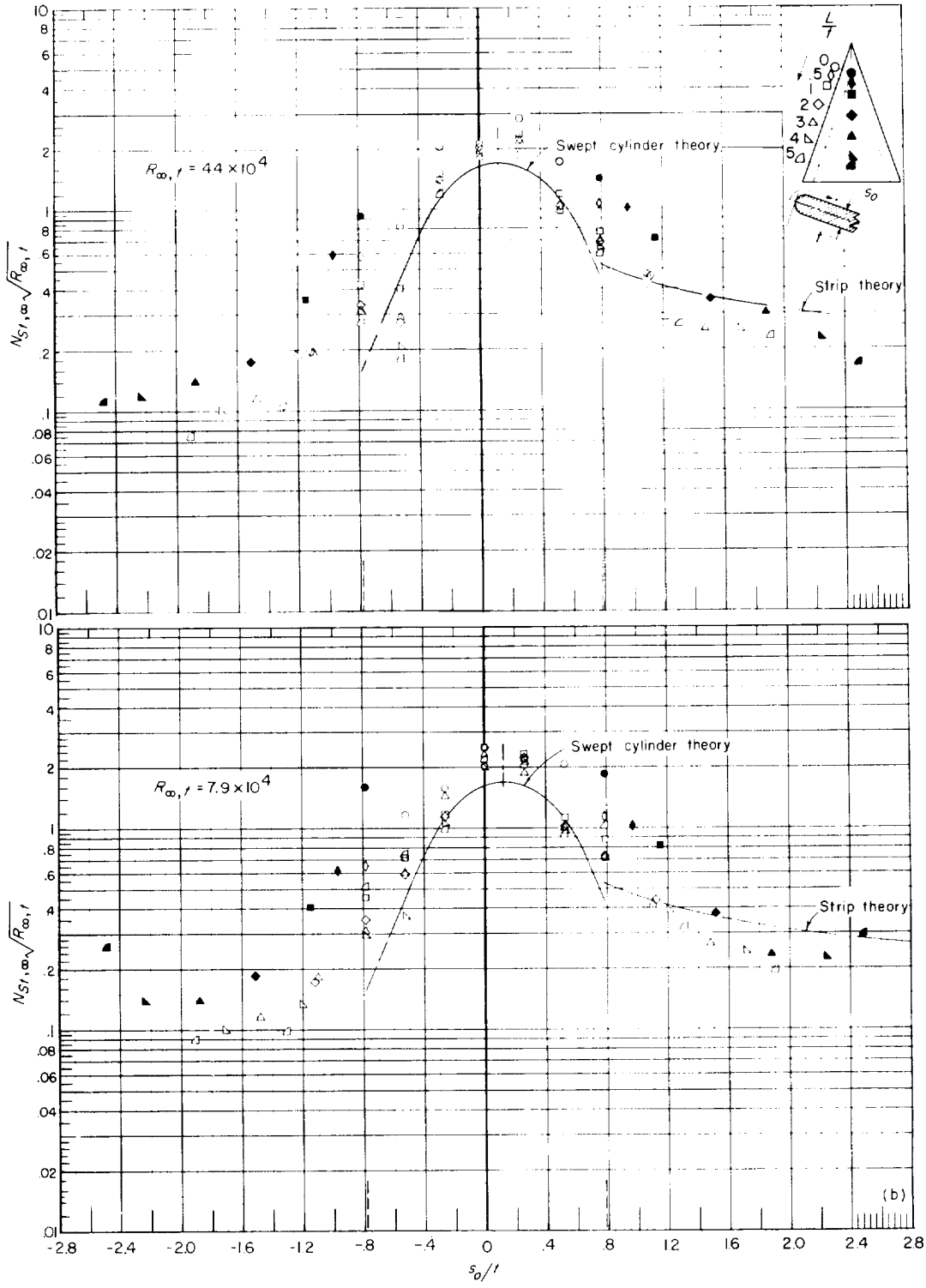

(b) $\alpha = 5^\circ$.

Figure 30.- Continued.

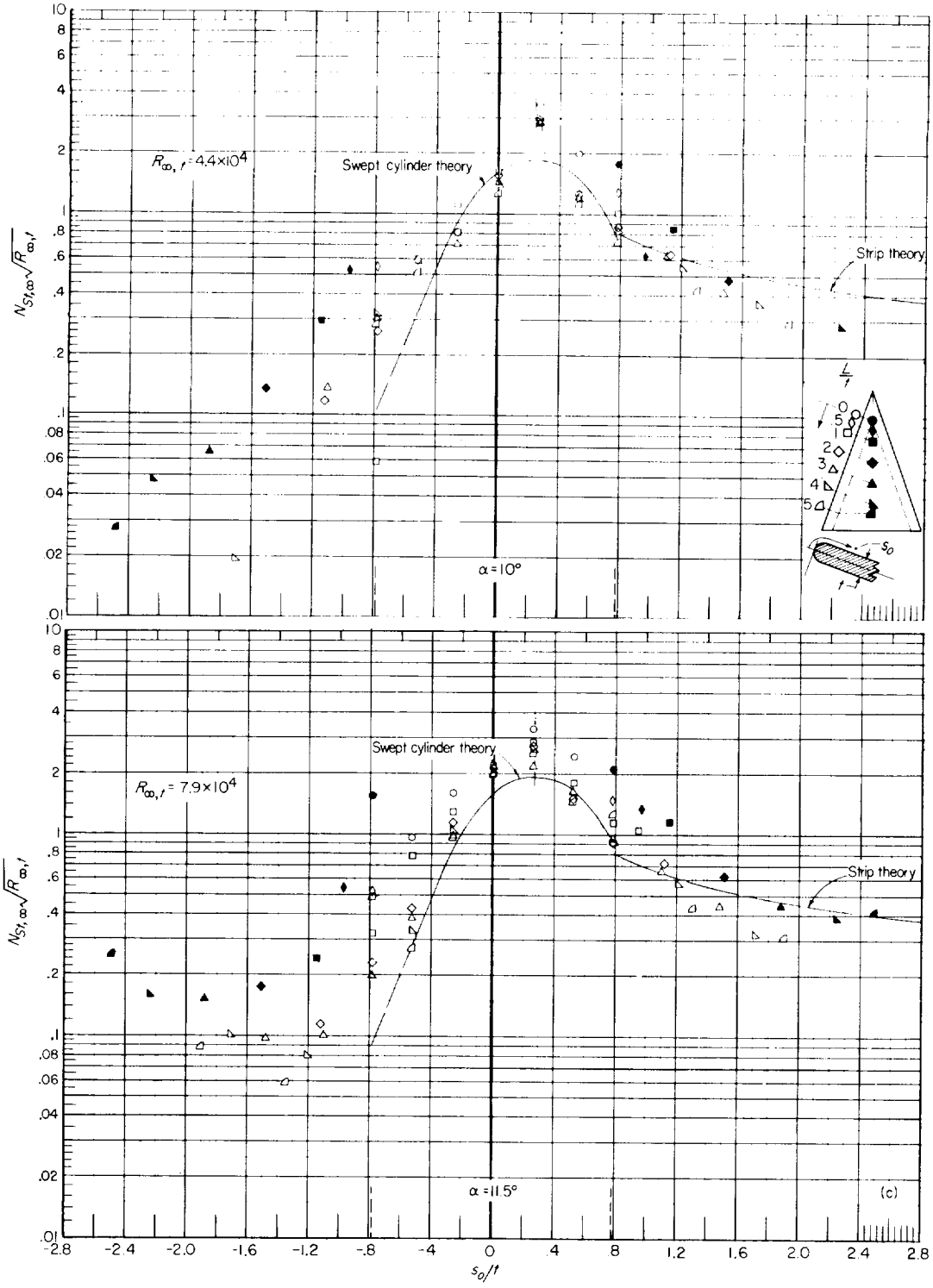

(c) $\alpha \approx 10^{\circ}$.

Figure 30.- Continued.

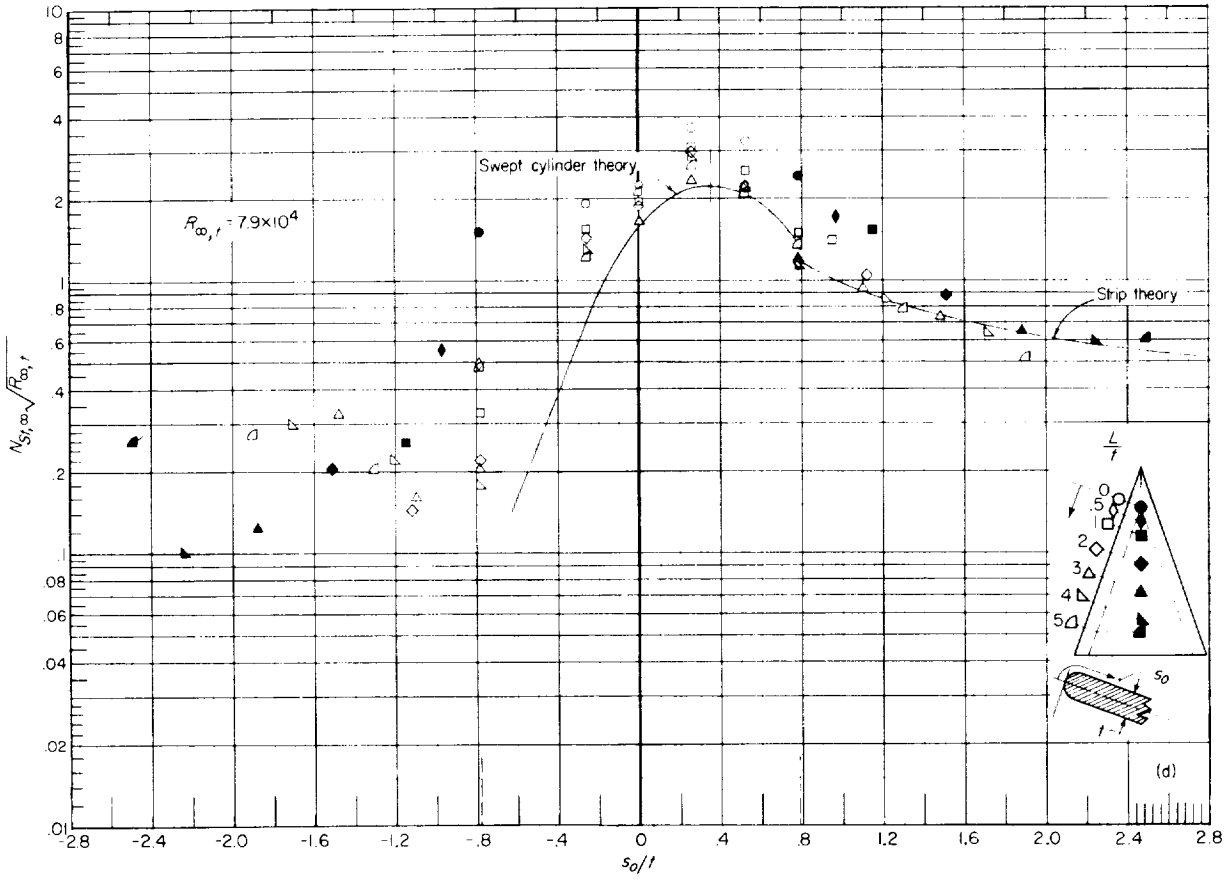

(d) $\alpha = 16.5°$.

Figure 30.- Continued.

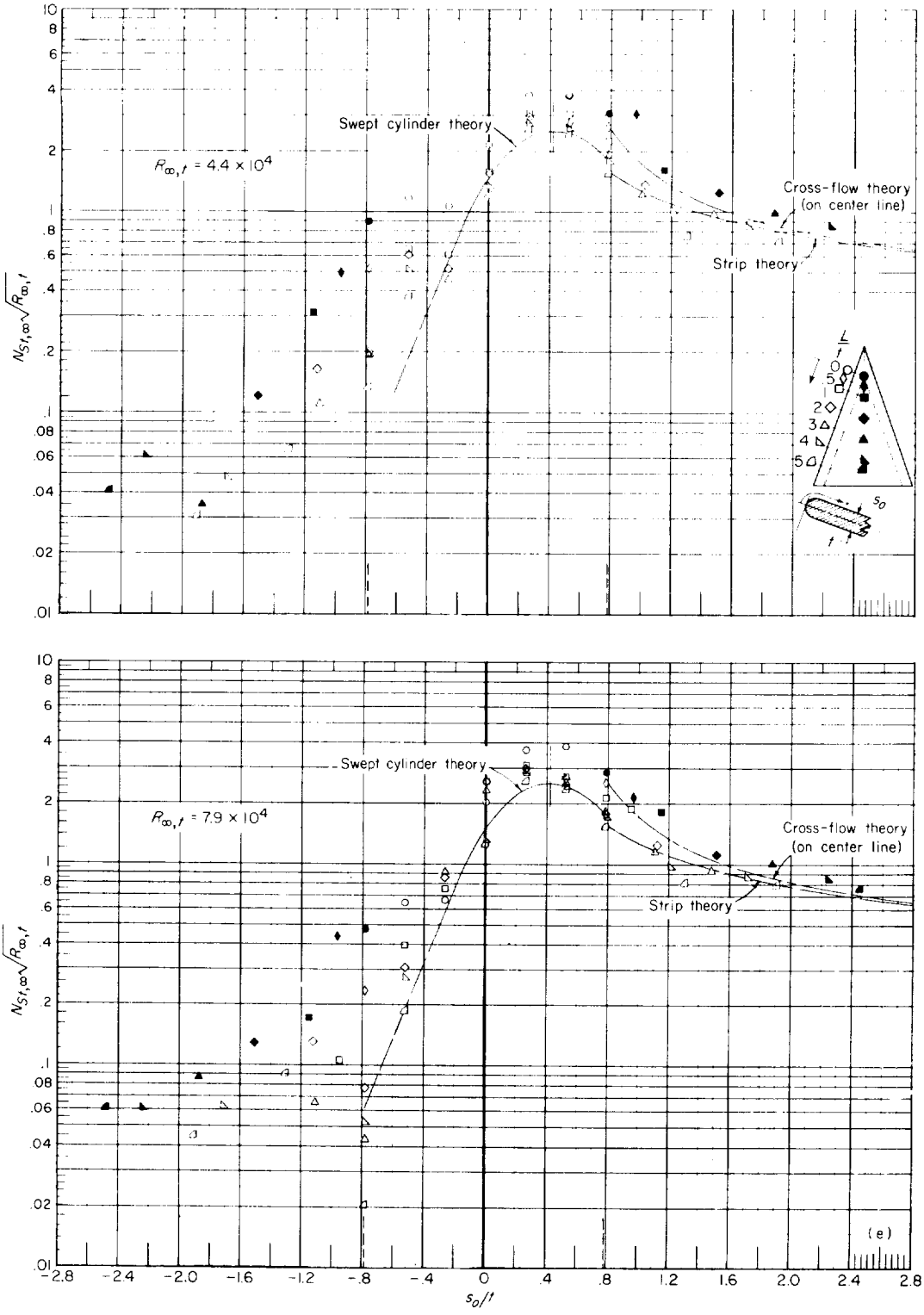

(e) $\alpha = 21^\circ$.

Figure 30.- Continued.

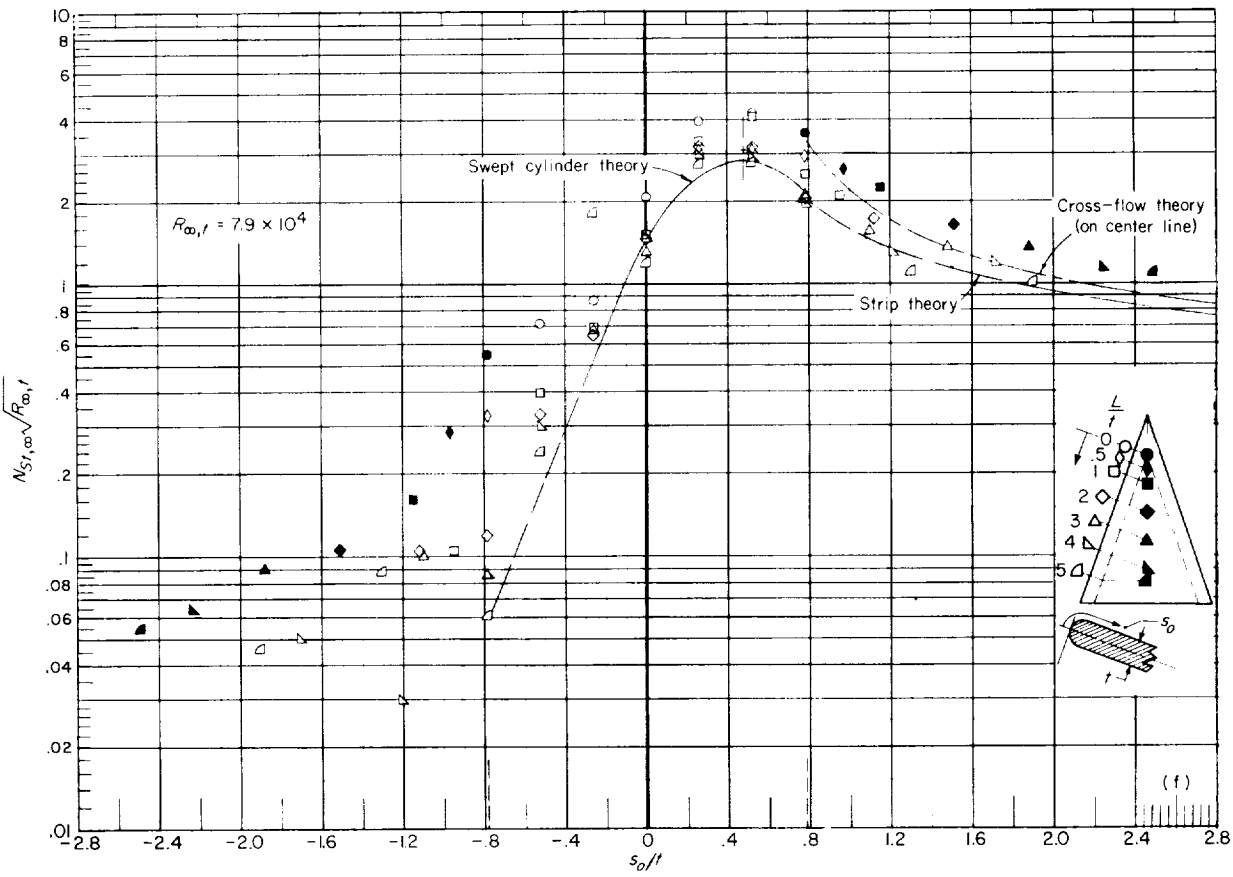

(f) $\alpha = 26^\circ$.

Figure 30.- Continued.

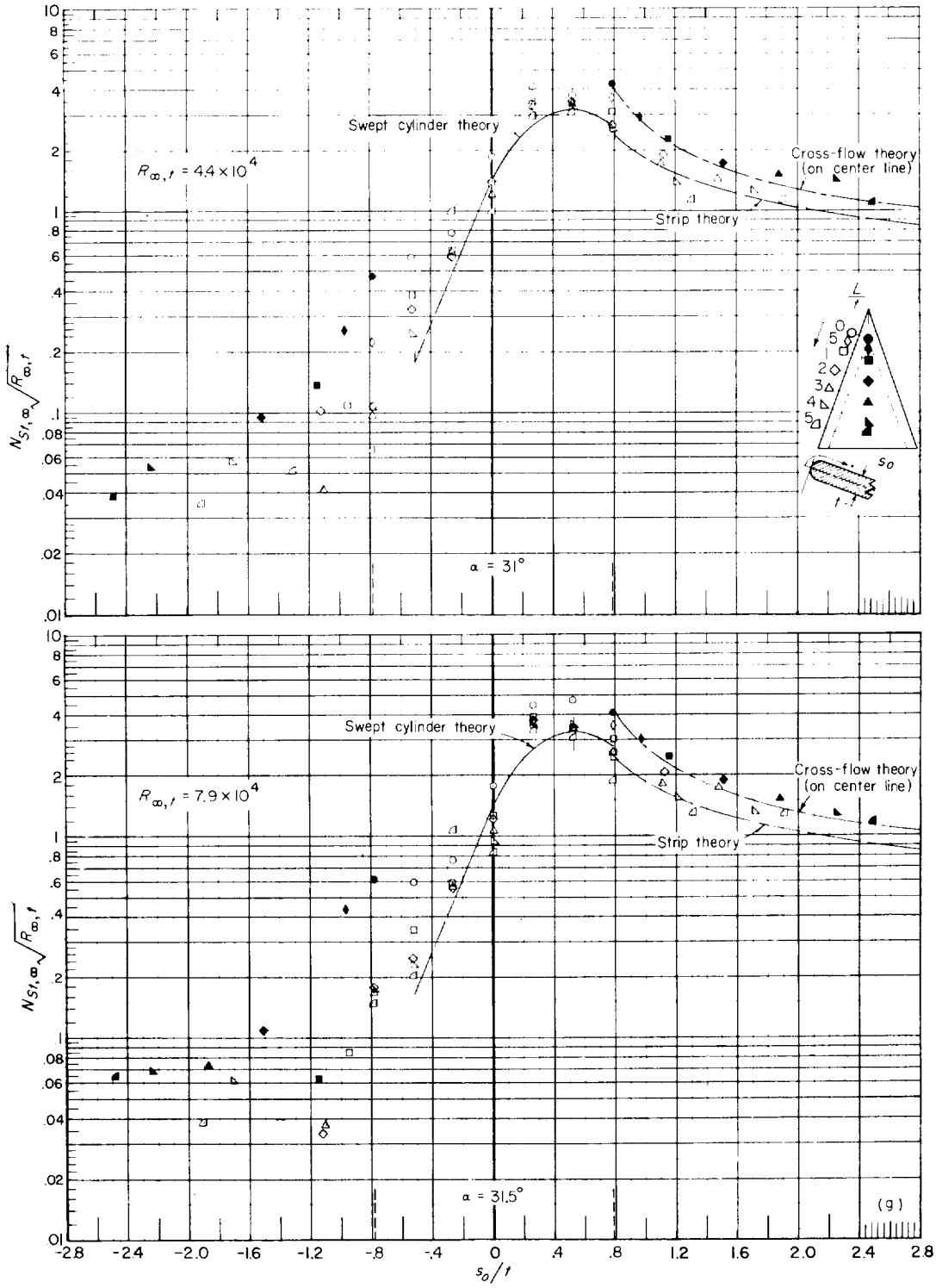

(g) $\alpha \approx 31°$.

Figure 30.- Continued.

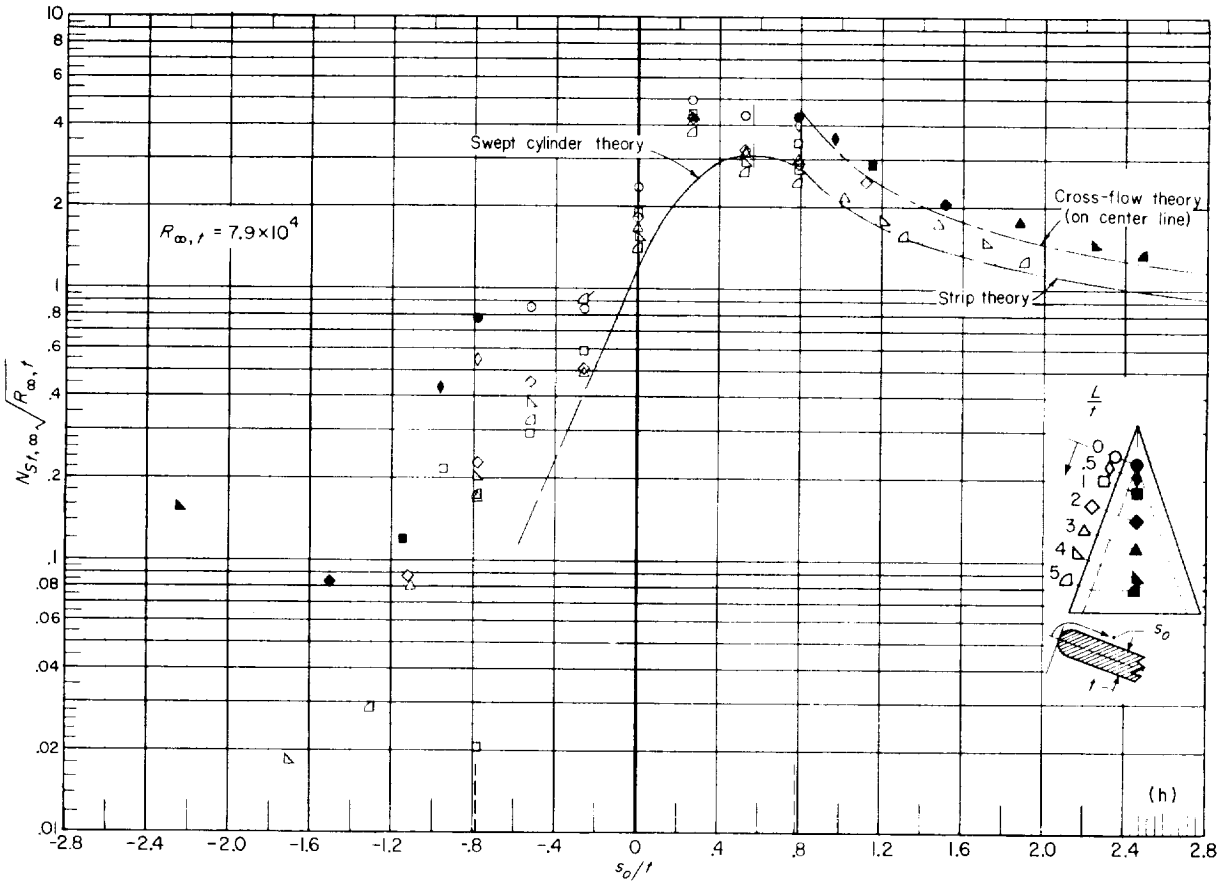

(h) $\alpha = 35^\circ$.

Figure 30.- Concluded.

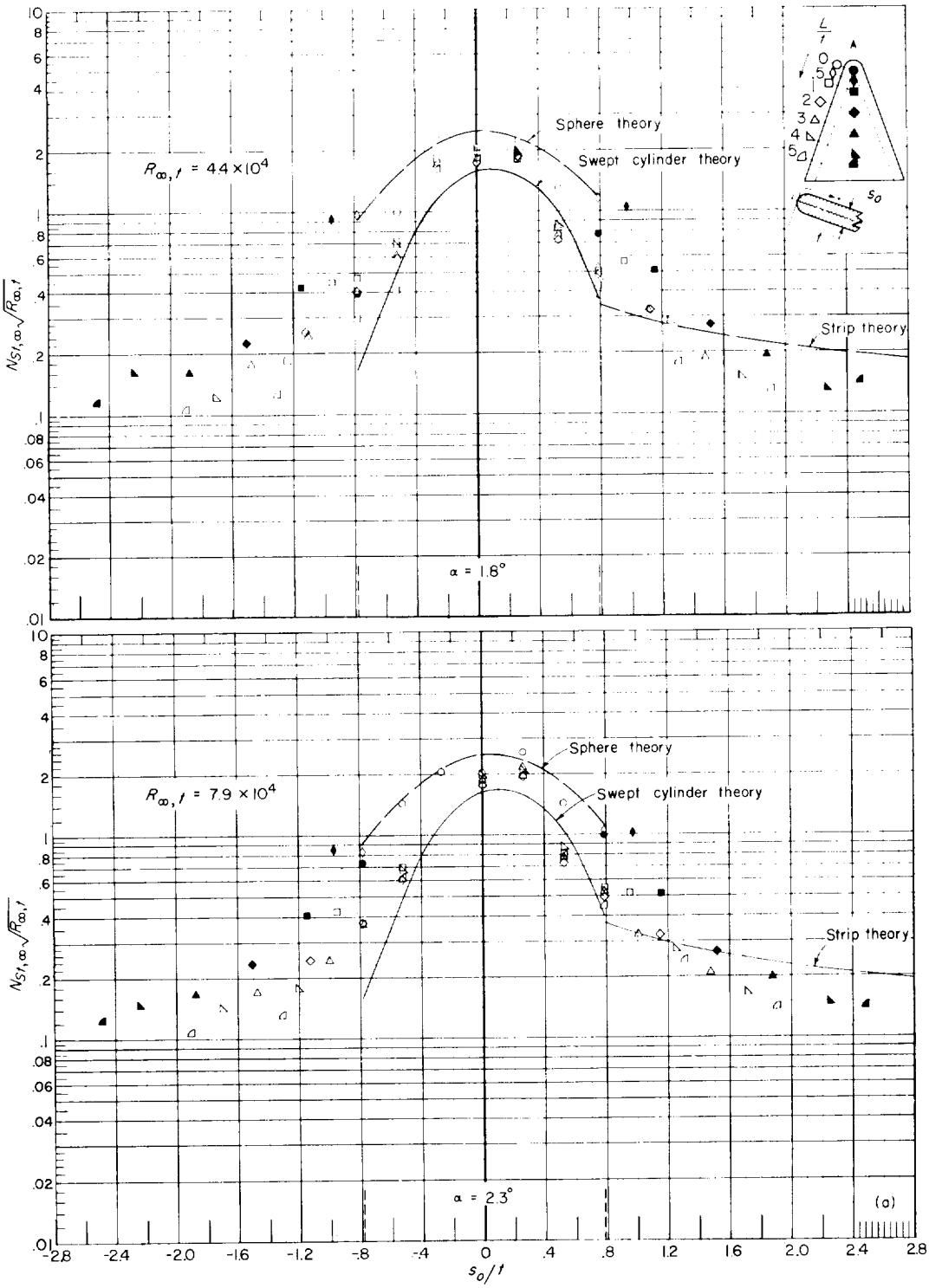

(a) $\alpha \approx 2°$.

Figure 31.- Stanton number distribution normal to the leading edge on blunt-prow delta wing at various stations along the leading edge at angle of attack. $M_\infty = 9.6$; air.

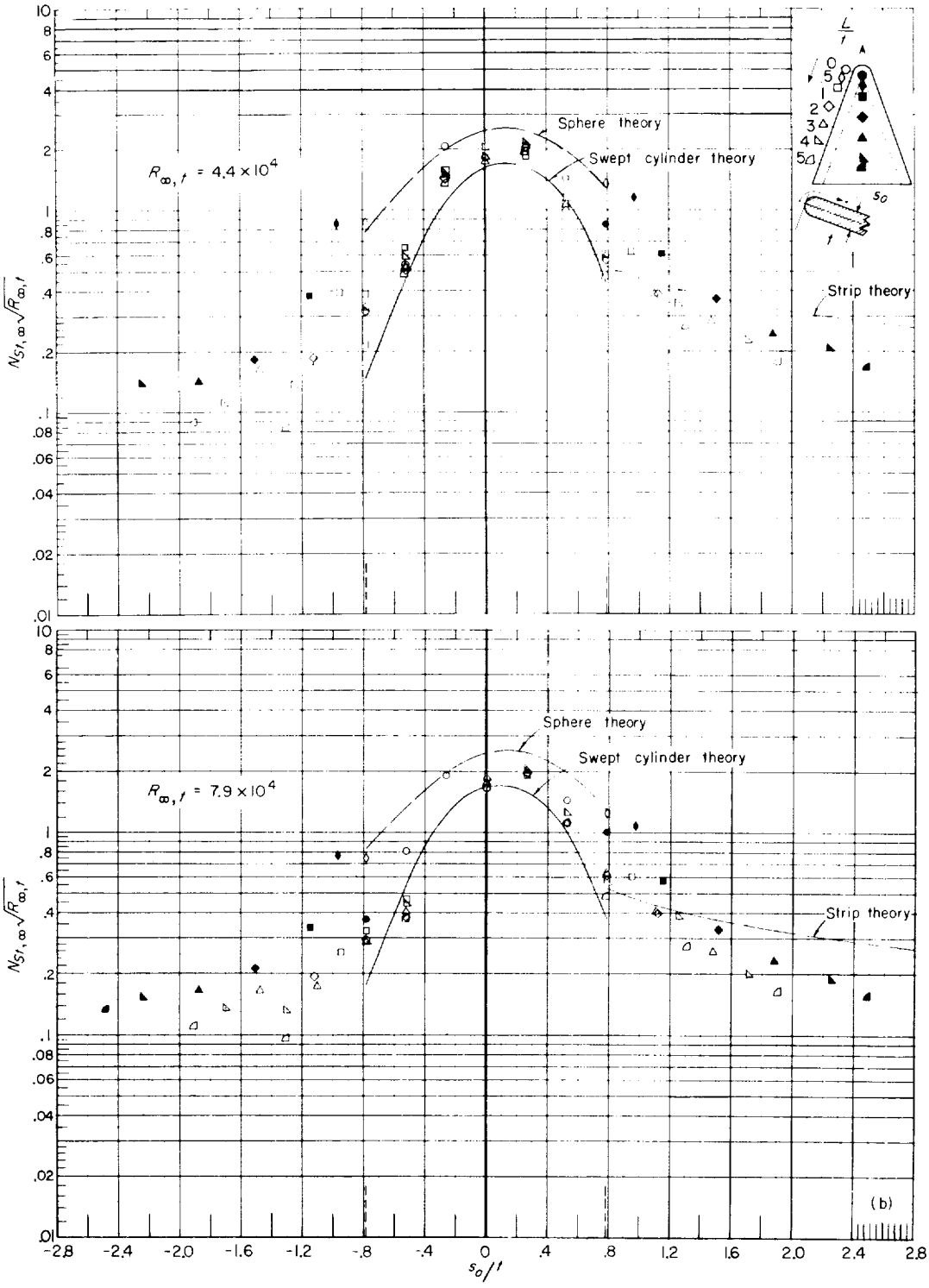

(b) $\alpha = 5.2^{\circ}$.

Figure 31.- Continued.

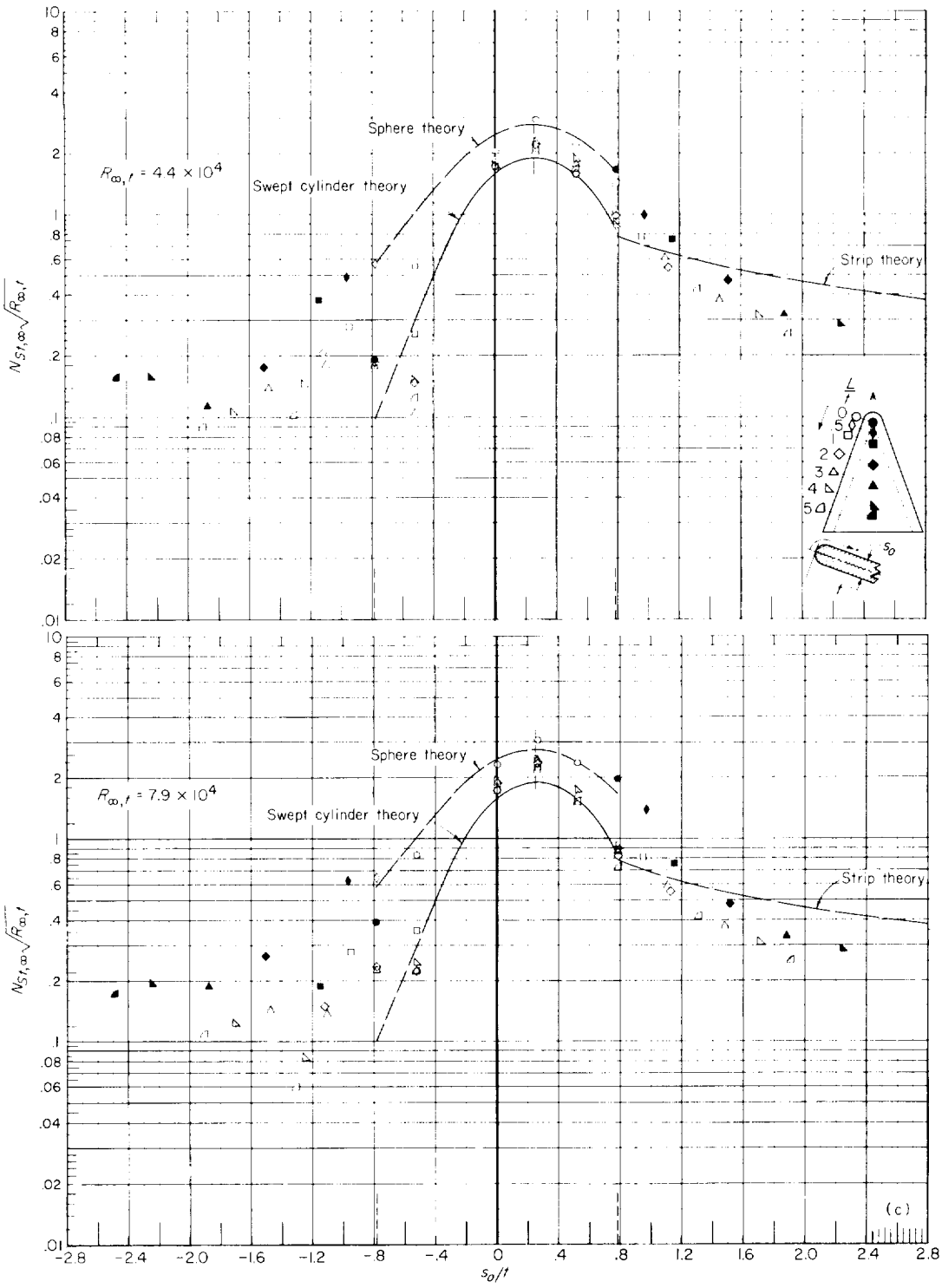

(c) $\alpha = 10.5^\circ$.

Figure 31.- Continued.

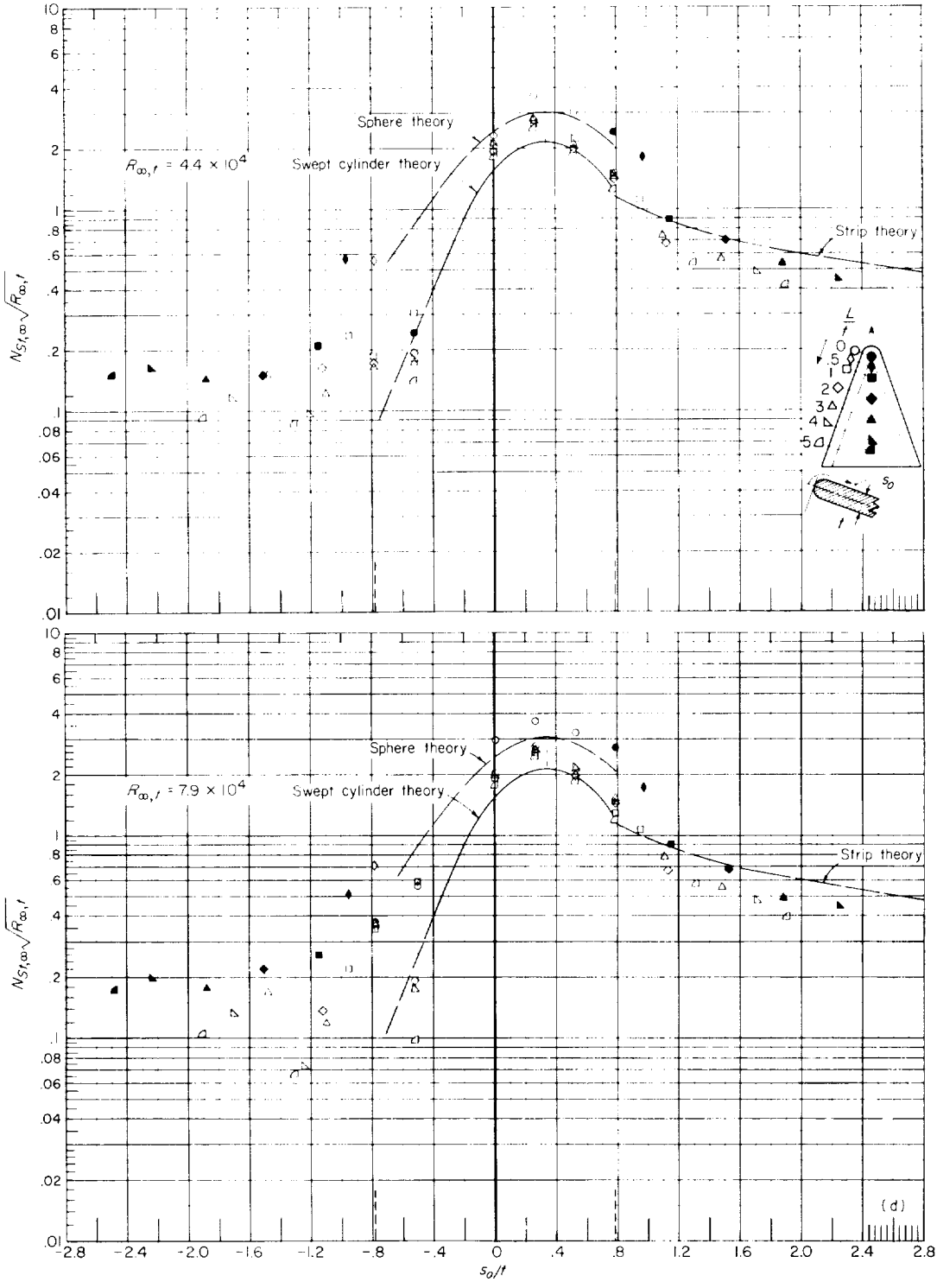

(d) $\alpha = 15.5^\circ$.

Figure 31.- Continued.

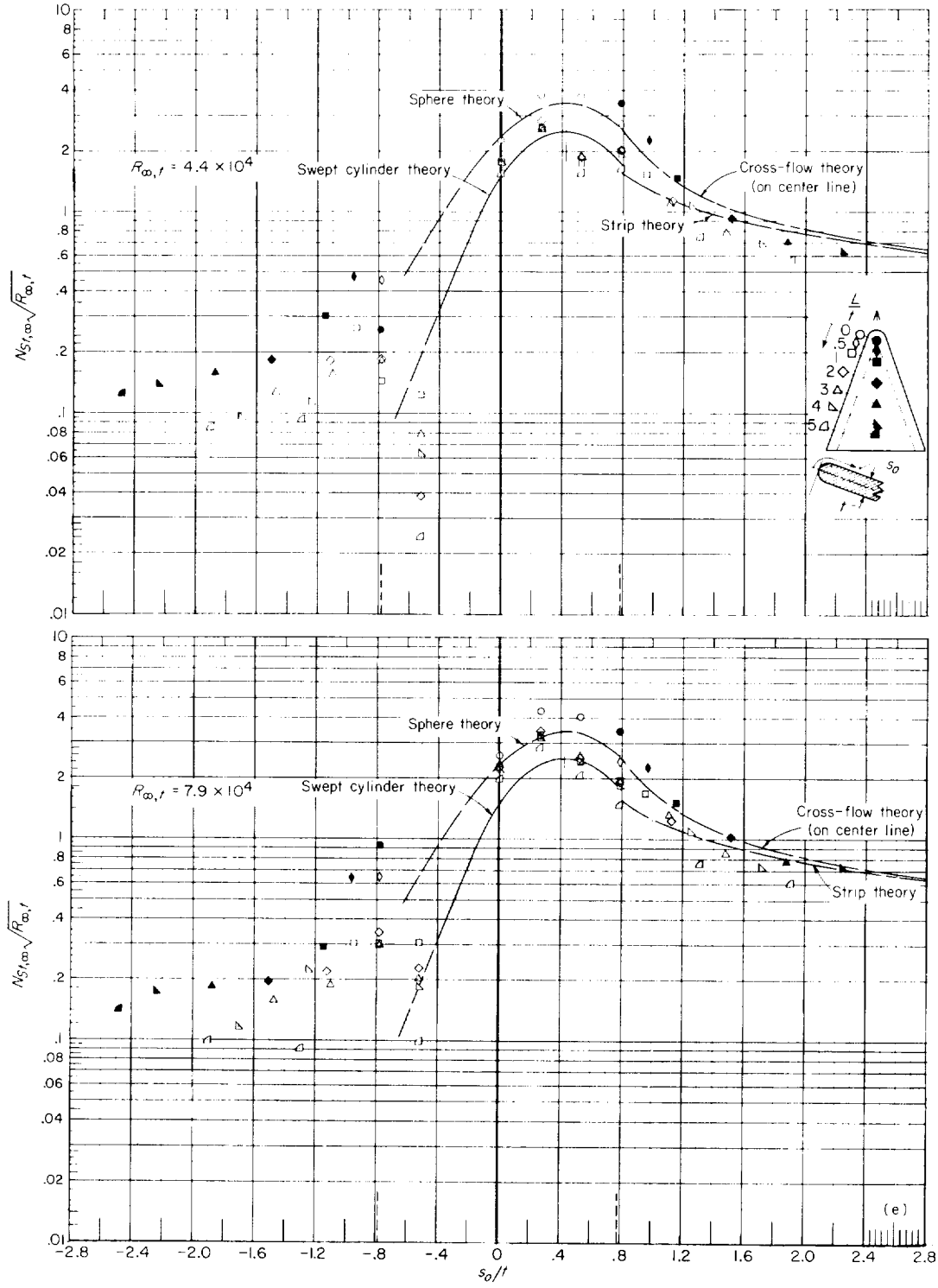

(e) $\alpha = 21^\circ$.

Figure 31.- Continued.

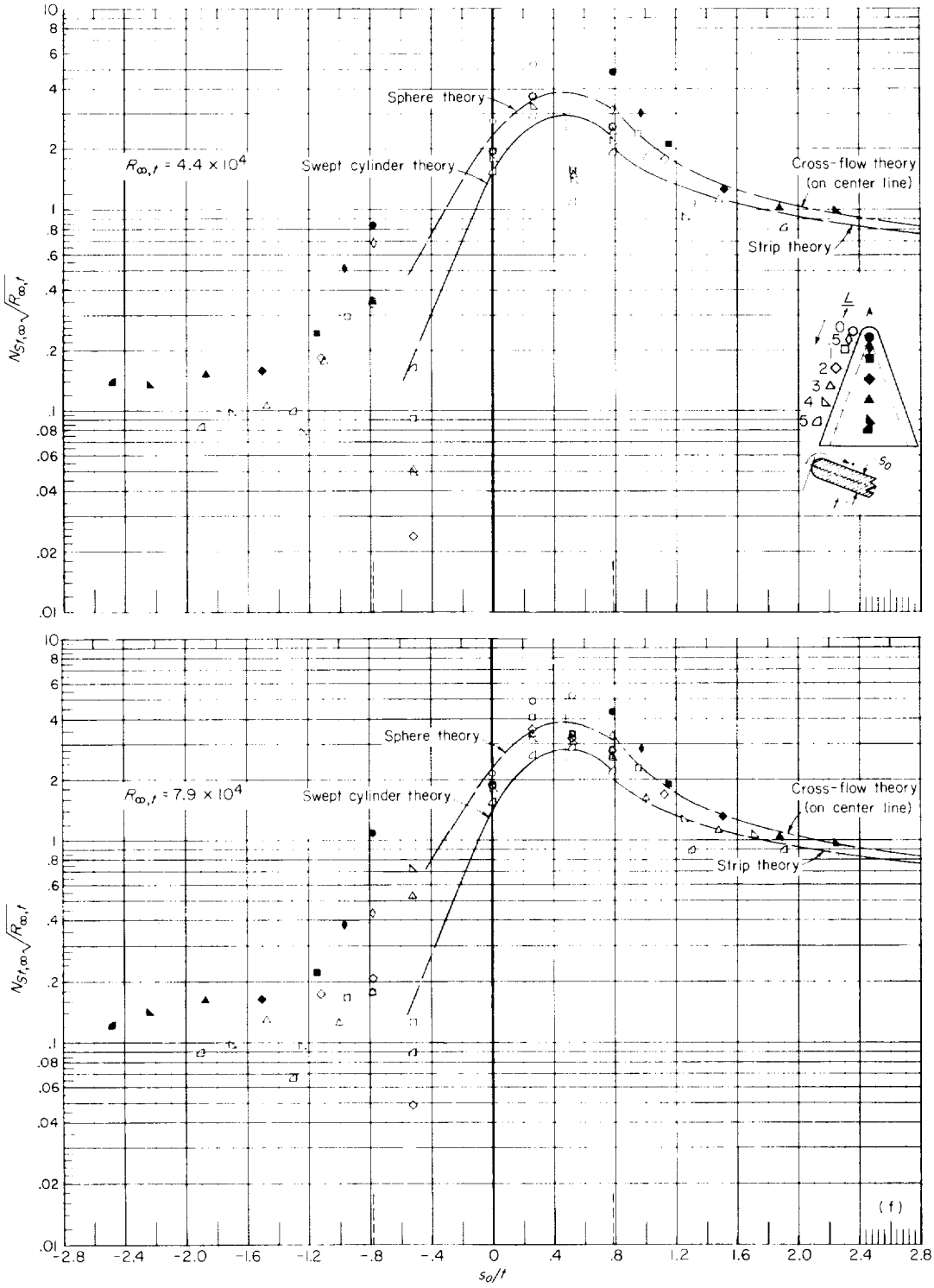

(f) $\alpha = 26^\circ$.

Figure 31.- Continued.

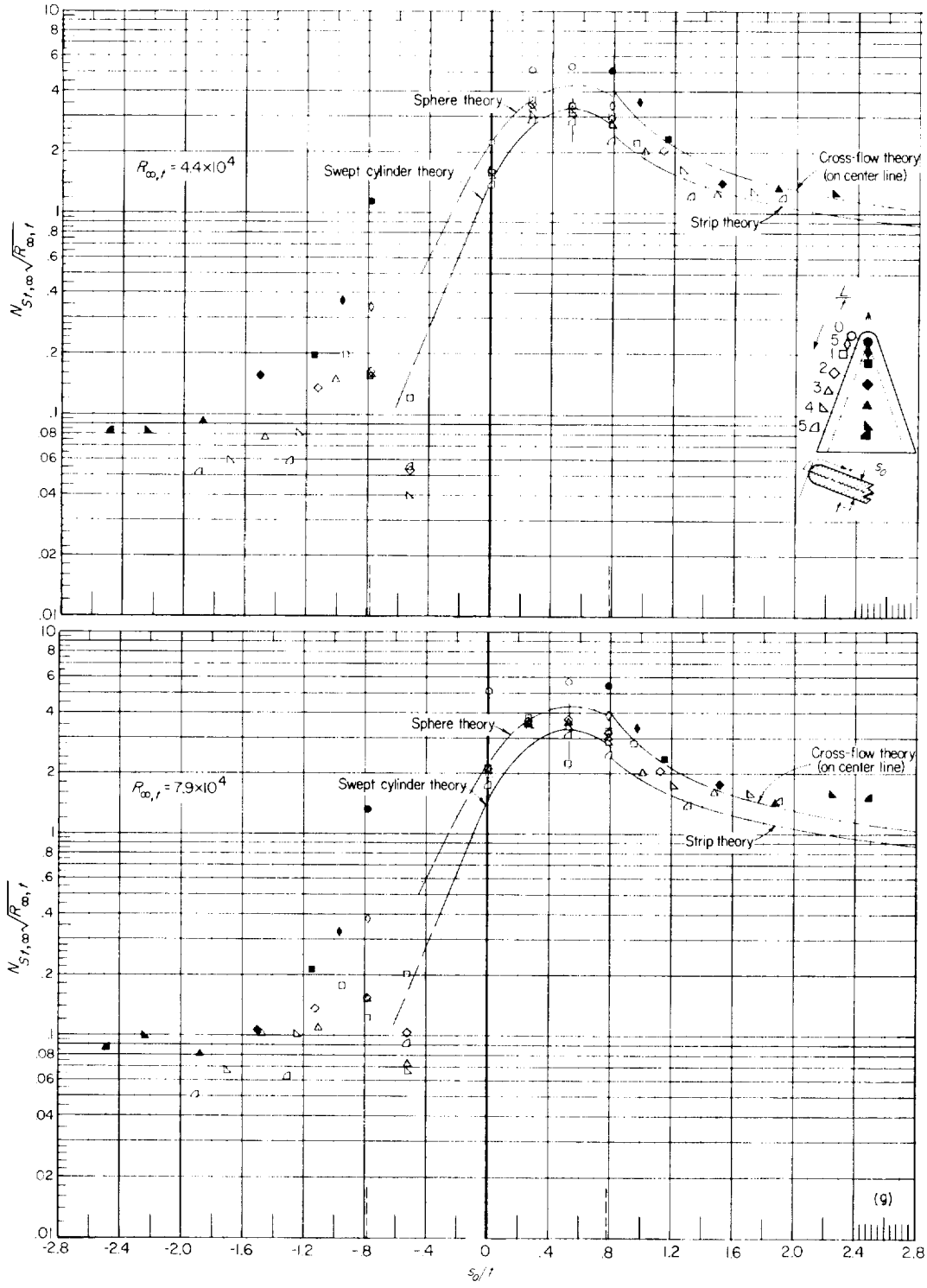

(g) $\alpha = 31.5^\circ$.

Figure 31.- Continued.

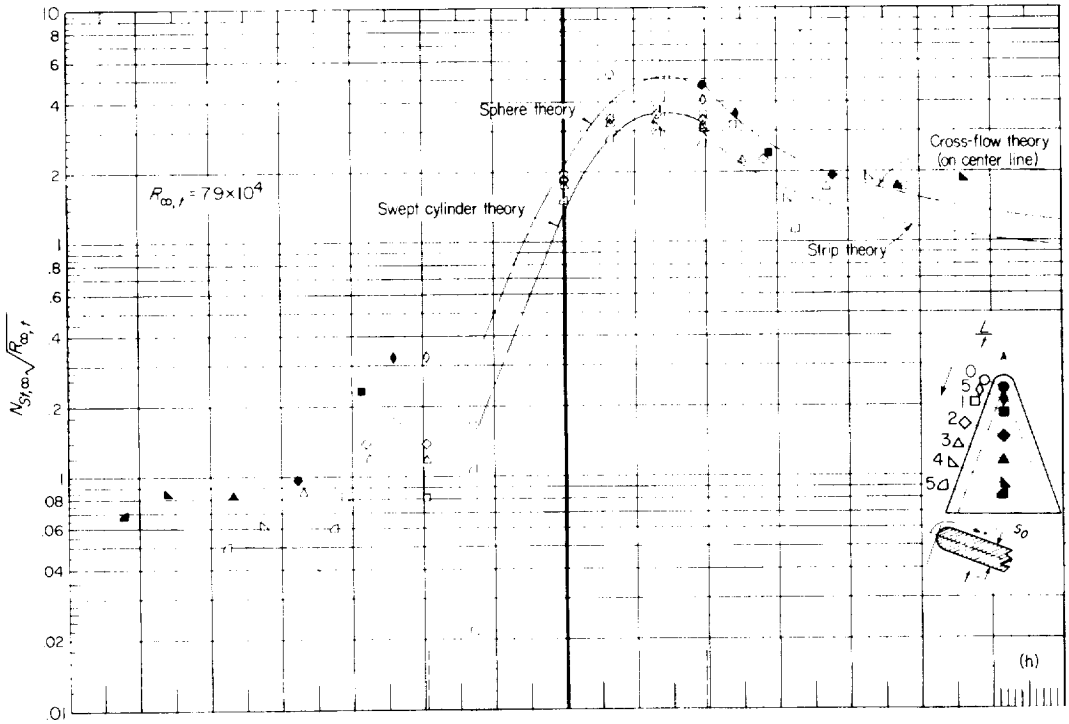

(h) $\alpha = 36.5^\circ$.

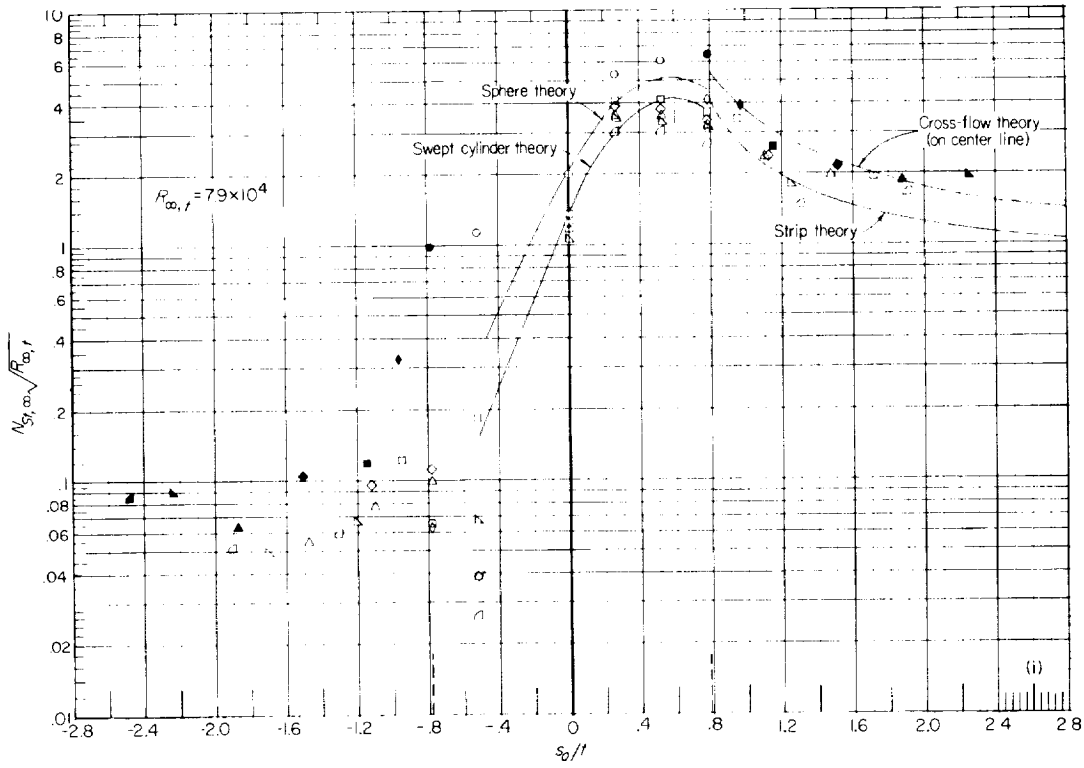

(i) $\alpha = 41.5^\circ$.

Figure 31.- Concluded.

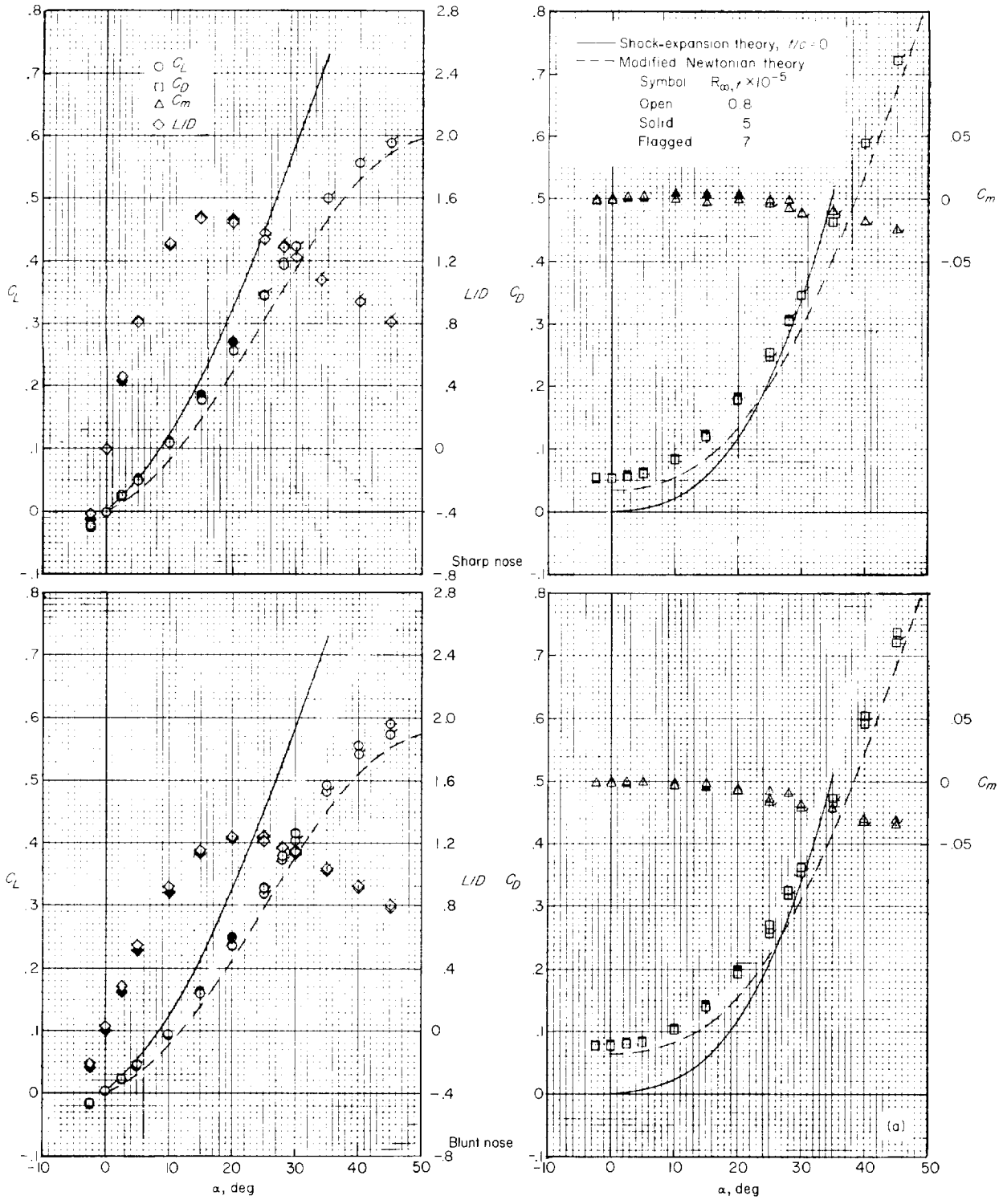

(a) $t/c_r = 0.143$.

Figure 32.- Aerodynamic characteristics of slab delta wing at angle of attack. $M_\infty = 6.8$; air.

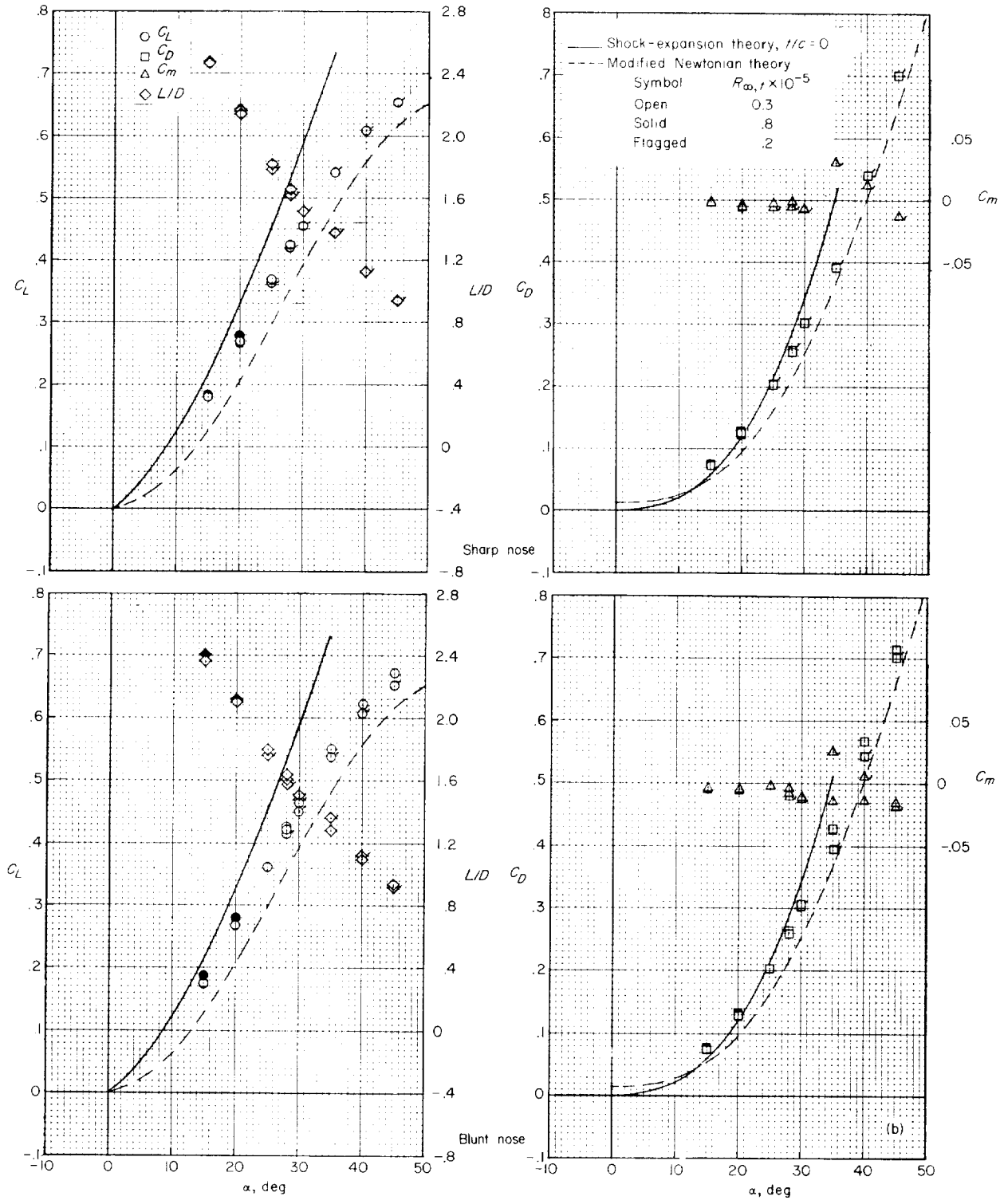

(b) $t/c_r = 0.048$.

Figure 32.- Concluded.

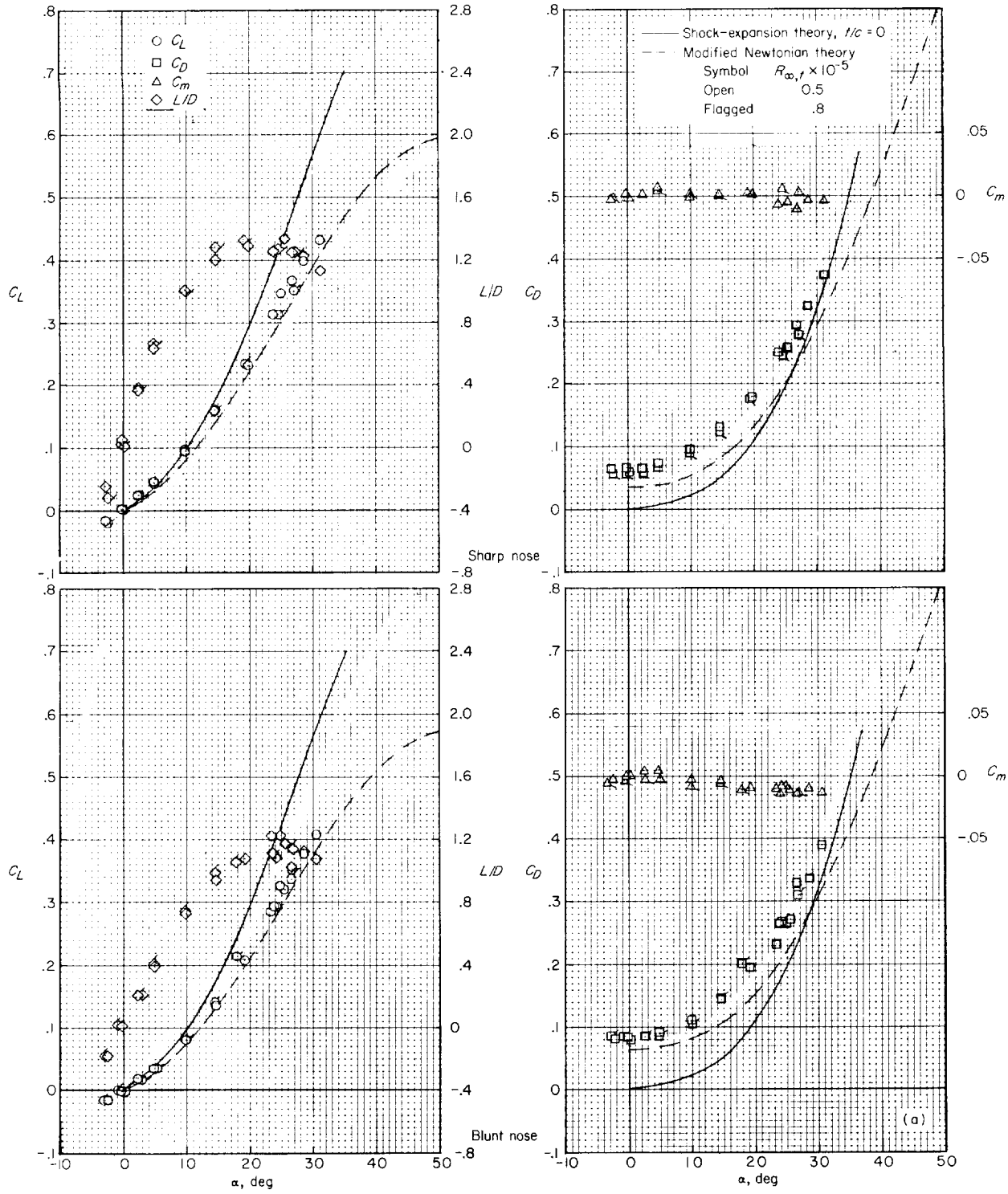

(a) $t/c_r = 0.143$.

Figure 33.- Aerodynamic characteristics of slab delta wing at angle of attack. $M_\infty = 9.6$; air.

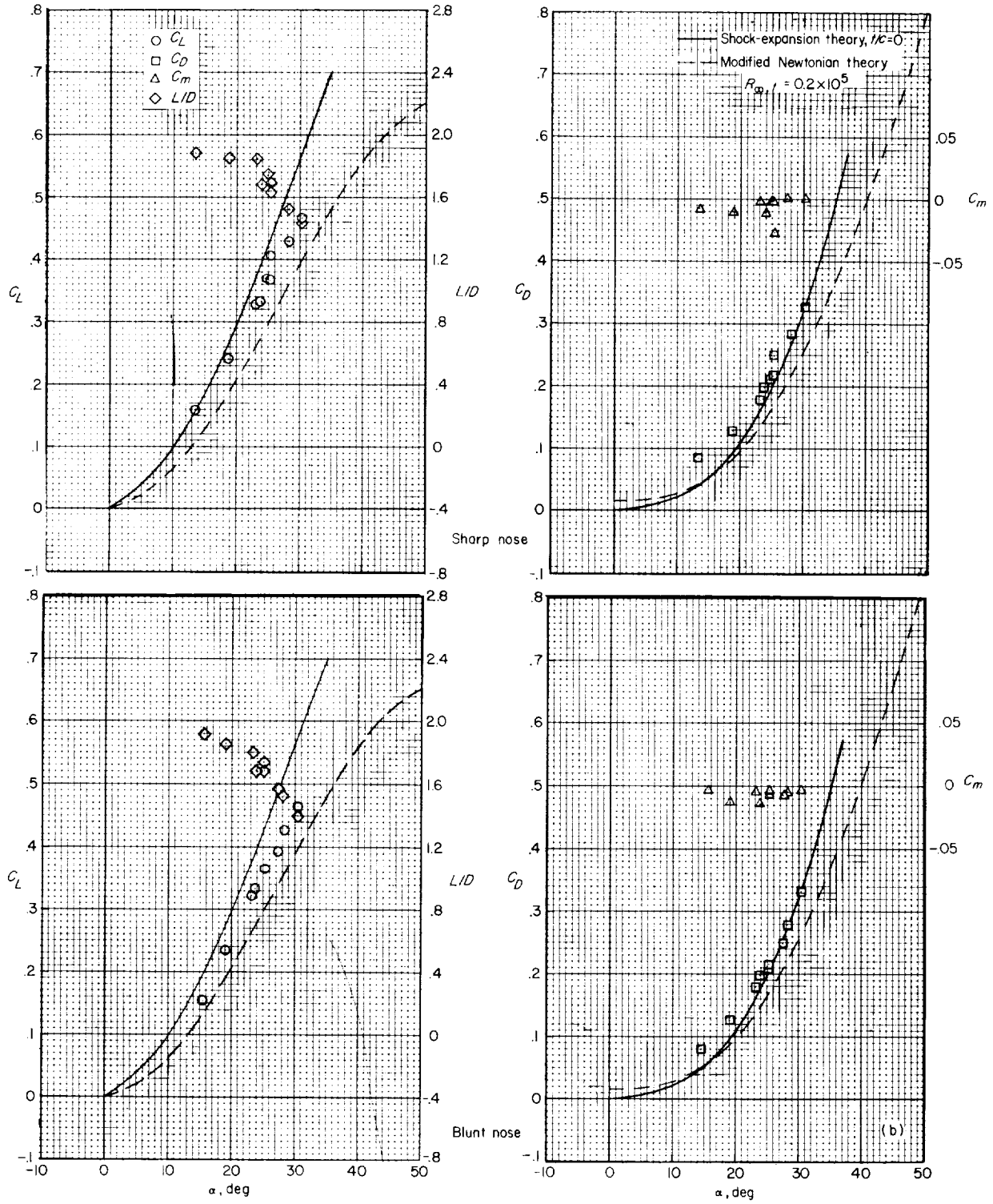

(b) $t/c_r = 0.048$.

Figure 33.- Concluded.

NASA TR R-153
National Aeronautics and Space Administration.
AN EXPERIMENTAL STUDY OF THE PRESSURE AND HEAT-TRANSFER DISTRIBUTION ON A 70° SWEEP SLAB DELTA WING IN HYPERSONIC FLOW.
Mitchel H. Bertram and Philip E. Everhart.
December 1963. i, 122p. OTS price, $2.75.
(NASA TECHNICAL REPORT R-153)

Results are presented for a study of the pressure and heat-transfer distributions and force characteristics of slab delta wings of 70° sweep at Mach numbers of 6.8 and 9.6 in air and 18 in helium. The wings had cylindrical leading edges and were tested with two different noses. One was sharp in plan view and the other was a tangent sphere with the same diameter as the cylindrical leading edge. Simple approaches to predicting the heat transfer are shown to be successful if the flow pattern peculiar to the angle-of-attack range under consideration is taken into account.

I. Bertram, Mitchel H.
II. Everhart, Philip E.
III. NASA TR R-153

NASA

NASA TR R-153
National Aeronautics and Space Administration.
AN EXPERIMENTAL STUDY OF THE PRESSURE AND HEAT-TRANSFER DISTRIBUTION ON A 70° SWEEP SLAB DELTA WING IN HYPERSONIC FLOW.
Mitchel H. Bertram and Philip E. Everhart.
December 1963. i, 122p. OTS price, $2.75.
(NASA TECHNICAL REPORT R-153)

Results are presented for a study of the pressure and heat-transfer distributions and force characteristics of slab delta wings of 70° sweep at Mach numbers of 6.8 and 9.6 in air and 18 in helium. The wings had cylindrical leading edges and were tested with two different noses. One was sharp in plan view and the other was a tangent sphere with the same diameter as the cylindrical leading edge. Simple approaches to predicting the heat transfer are shown to be successful if the flow pattern peculiar to the angle-of-attack range under consideration is taken into account.

I. Bertram, Mitchel H.
II. Everhart, Philip E.
III. NASA TR R-153

NASA

NASA TR R-153
National Aeronautics and Space Administration.
AN EXPERIMENTAL STUDY OF THE PRESSURE AND HEAT-TRANSFER DISTRIBUTION ON A 70° SWEEP SLAB DELTA WING IN HYPERSONIC FLOW.
Mitchel H. Bertram and Philip E. Everhart.
December 1963. i, 122p. OTS price, $2.75.
(NASA TECHNICAL REPORT R-153)

Results are presented for a study of the pressure and heat-transfer distributions and force characteristics of slab delta wings of 70° sweep at Mach numbers of 6.8 and 9.6 in air and 18 in helium. The wings had cylindrical leading edges and were tested with two different noses. One was sharp in plan view and the other was a tangent sphere with the same diameter as the cylindrical leading edge. Simple approaches to predicting the heat transfer are shown to be successful if the flow pattern peculiar to the angle-of-attack range under consideration is taken into account.

I. Bertram, Mitchel H.
II. Everhart, Philip E.
III. NASA TR R-153

NASA

NASA TR R-153
National Aeronautics and Space Administration.
AN EXPERIMENTAL STUDY OF THE PRESSURE AND HEAT-TRANSFER DISTRIBUTION ON A 70° SWEEP SLAB DELTA WING IN HYPERSONIC FLOW.
Mitchel H. Bertram and Philip E. Everhart.
December 1963. i, 122p. OTS price, $2.75.
(NASA TECHNICAL REPORT R-153)

Results are presented for a study of the pressure and heat-transfer distributions and force characteristics of slab delta wings of 70° sweep at Mach numbers of 6.8 and 9.6 in air and 18 in helium. The wings had cylindrical leading edges and were tested with two different noses. One was sharp in plan view and the other was a tangent sphere with the same diameter as the cylindrical leading edge. Simple approaches to predicting the heat transfer are shown to be successful if the flow pattern peculiar to the angle-of-attack range under consideration is taken into account.

I. Bertram, Mitchel H.
II. Everhart, Philip E.
III. NASA TR R-153

NASA

"The National Aeronautics and Space Administration . . . shall . . . provide for the widest practical appropriate dissemination of information concerning its activities and the results thereof . . . objectives being the expansion of human knowledge of phenomena in the atmosphere and space."

—NATIONAL AERONAUTICS AND SPACE ACT OF 1958

NASA SCIENTIFIC AND TECHNICAL PUBLICATIONS

TECHNICAL REPORTS: Scientific and technical information considered important, complete, and a lasting contribution to existing knowledge.

TECHNICAL NOTES: Information less broad in scope but nevertheless of importance as a contribution to existing knowledge.

TECHNICAL MEMORANDUMS: Information receiving limited distribution because of preliminary data, security classification, or other reasons.

CONTRACTOR REPORTS: Technical information generated in connection with a NASA contract or grant and released under NASA auspices.

TECHNICAL TRANSLATIONS: Information published in a foreign language considered to merit NASA distribution in English.

TECHNICAL REPRINTS: Information derived from NASA activities and initially published in the form of journal articles or meeting papers.

SPECIAL PUBLICATIONS: Information derived from or of value to NASA activities but not necessarily reporting the results of individual NASA-programmed scientific efforts. Publications include conference proceedings, monographs, data compilations, handbooks, sourcebooks, and special bibliographies.

Details on the availability of these publications may be obtained from:

SCIENTIFIC AND TECHNICAL INFORMATION DIVISION

NATIONAL AERONAUTICS AND SPACE ADMINISTRATION

Washington, D.C. 20546